Phosphorus Magnetic Resonance Spectroscopy in Breast Cancer

Wybe van der Kemp

Cover design: Wybe van der Kemp.
Cover background painting: ‘Sunrise in October’ by Ken Bushe.
Print: Ipskamp Drukkers, Enschede, The Netherlands.

PhD thesis, Utrecht University.
ISBN: 978-90-393-6175-7.

The publication of this thesis was financially supported by Philips Healthcare, Best, The Netherlands.

Phosphorus Magnetic Resonance Spectroscopy in Breast Cancer

Fosfor Magnetische Resonantie Spectroscopie bij Borstkanker

(met een samenvatting in het Nederlands)

PROEFSCHRIFT

TER VERKRIJGING VAN DE GRAAD VAN DOCTOR AAN DE UNIVERSITEIT UTRECHT OP GEZAG VAN DE RECTOR MAGNIFICUS, PROF. DR. G. J. VAN DER ZWAAN, INGEVOLGE HET BESLUIT VAN HET COLLEGE VOOR PROMOTIES IN HET OPENBAAR TE VERDEDIGEN OP VRIJDAG 12 SEPTEMBER 2014 DES MIDDAGS TE 2.30 UUR

DOOR

WYBE JOHANNES MARIA VAN DER KEMP

GEBOREN OP 28 NOVEMBER 1964 TE EDE

Promotor: Prof. dr. P.R. Luijten

Copromotor: Dr. D.W.J. Klomp

Table of Contents

CHAPTER 1

Introduction

1.1 Rationale

Breast cancer is the most prevalent type of cancer in women worldwide (1). In the western world the risk for a woman of developing invasive breast cancer during her lifetime is 1 in 8, and the risk of dying from invasive breast cancer is 1 in 36 (2). Conventional triple diagnosis consists of palpation, mammography and fine-needle cytology, which is nowadays often supplemented with ultrasonography (3). Lesion staging requires precise knowledge of the size, as well as of the presence or absence of lesions in other quadrants of the breast. Unfortunately, conventional triple diagnosis is insufficient in this respect. For instance, 9% to 30% of malignant lesions are not identified with mammography (4-8), while 11% to 15% of malignant lesions are not identified with ultrasonography (6,7). Furthermore, when a lesion is detected on mammography or ultrasonography, the size is often underestimated and multicentric or multifocal disease may be overlooked (6,7). Moreover, lesion detection on mammography is less sensitive in women with dense breast tissue (8,9).

In recent years there has been an increasing interest in Magnetic Resonance Imaging (MRI) as a non-invasive diagnostic modality for the work-up of suspicious breast lesions. The sensitivity of MRI for diagnosing breast cancer is over 90%, the specificity around 70% (10). The additional value of MRI in the staging of breast lesions lies in its capability to depict multicentric and multifocal disease, to assess the tumor in a three-dimensional way and to detect cancer in dense breast tissue (10).

Recently, ultra-high field 7.0 Tesla MRI has become clinically available, which offers new diagnostic possibilities. At ultra-high magnetic field strength images can be acquired at a higher spatial resolution, allowing smaller structural details to be depicted. For breast cancer this means not only detection of smaller lesions, but also increased morphologic detail of lesions that may aid classification and better delineation of lesion extent.

In addition, the higher spectral resolution and sensitivity of 7T MRI makes this ultra-high field strength ideal for Magnetic Resonance Spectroscopy (MRS), in which various

metabolite levels can be measured *in vivo*. Phosphorus may be one of the most promising nuclei in studying oncology with MRS. However, because of the very low metabolic concentrations in fibroglandular tissue, this requires highly efficient and sensitive breast coils and optimized pulse sequences to obtain the highest signal-to-noise ratio (SNR) possible.

With these prerequisites in place, MRS imaging can possibly increase breast cancer detection specificity and also could be a tool for treatment efficacy monitoring.

Development of optimized pulse sequences for ^{31}P MRS in breast cancer research is the main theme of this thesis, ultimately leading to a feasibility study of monitoring neo-adjuvant chemotherapy using ^{31}P MRS.

Surgical treatment of breast cancer is sometimes preceded by chemo-, hormonal- and/or trastuzamab therapy (neo-adjuvant) to reduce tumor volume. Although most tumors decrease in volume in response to neoadjuvant therapy, volume reduction as assessed by MRI is not a reliable measure of therapy efficacy in terms of survival rate. The most accurate and relatively early predictor of survival rate is the absence of any tumor cells in the excised specimen. However, this complete pathological response is only seen in less than 20% of the patients (11). Moreover, this response is measured after completion of the entire neo-adjuvant therapy. To enable early switching to a more favourable neoadjuvant regime there is a need for monitoring neoadjuvant therapy efficacy. Rather than observing morphologic alterations of the tumor by MRI, monitoring of tumor metabolism by means of phosphorus magnetic resonance spectroscopy may offer a better window to assess neo-adjuvant therapy efficacy.

1.2 ^{31}P in the living cell

Phosphorus plays an important role in the energy and phospholipid metabolism of the living cell. The metabolites involved in energy metabolism are the mono-, di- and tri-phosphates of adenoside (AMP), (ADP), (ATP) respectively, phosphocreatine (PCr) and inorganic phosphate (Pi), for which the molecular structure is shown in Figure 1.1. Phospholipids are the major constituents of all membranes in the cell. The most abundant class of phospholipids are the glycerophospholipids that can be subdivided into glycero-phosphatidylcholines, -ethanolamines, -serines, and -inositols, as shown in Figure 1.2. Of these subclasses the glycerophosphatidylcholines and -ethanolamines have the highest abundance. The most important small aqueous phosphorus intermediates in the biosynthe-

sis of phospholipids are phosphocholine (PC) and phosphoethanolamine (PE), which are called phosphomonoesters (PME). Their glycerol derivatives glycerophosphocholine (GPC) and glycerophosphoethanolamine (GPE) are products of phospholipid breakdown and are called phosphodiesters (PDE), see Figure 1.3.

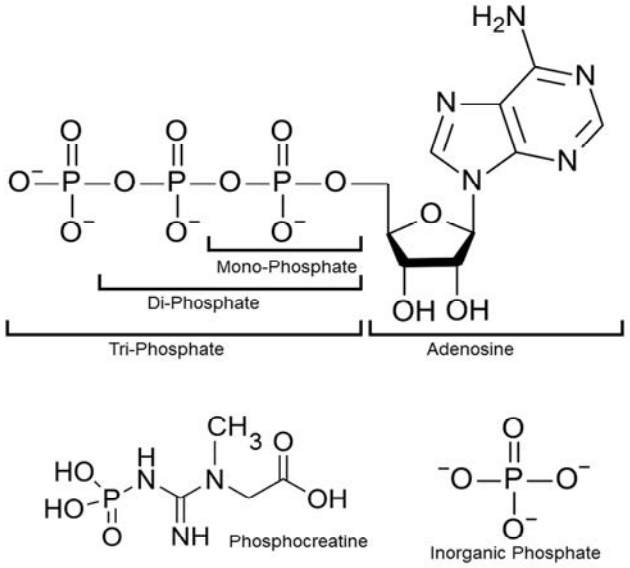

Figure 1.1. Some phosphorus metabolites involved in energy metabolism of the cell.

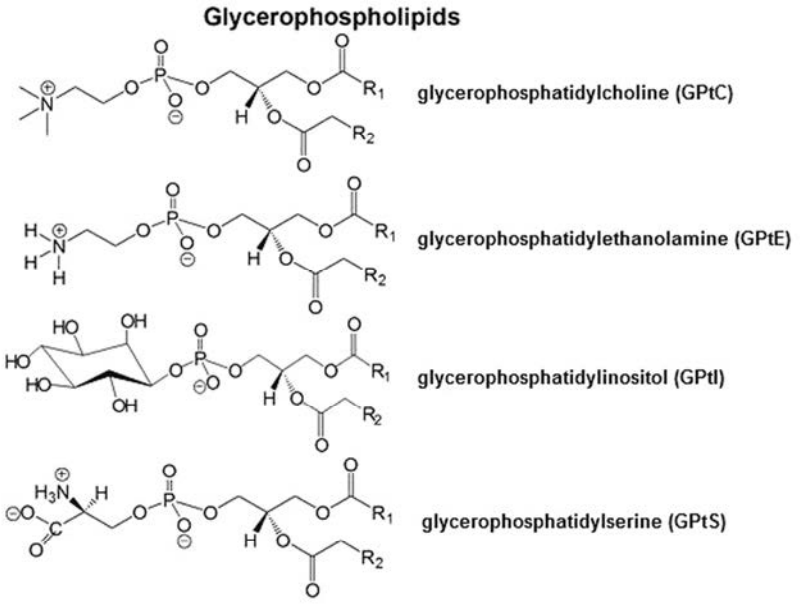

Figure 1.2. The glycerophospholipids.

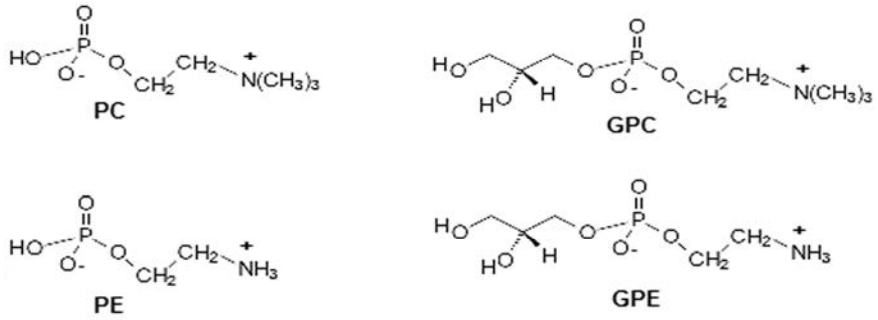

Figure 1.3. Intermediates in phospholipid biosynthesis and breakdown.

1.3 ^{31}P in cancer

From preclinical and clinical studies it is known that phospholipid metabolism is significantly altered in cancers (12,13). Almost all cancers display elevated PC and increased total choline-containing metabolites (13). In the breast for instance, a switch from high GPC / low PC to low GPC / high PC can be detected following malignant transformation (14). By measuring phospholipid metabolites MRS can be used as a tool for diagnosis of breast cancer, but more importantly for the monitoring of chemotherapy response, as has been shown in preclinical studies (15,16). As a rule of thumb, the ratio of PME to PDE goes up in cancer, with unrestrained cell multiplication, while in successful chemo-, radio-, or ablation therapy this ratio goes down. Measuring the concentration ratios of these metabolites *in vivo* with MRS can possibly enhance cancer detection and improve therapy efficacy monitoring. However, so far preclinical research has only been translated into clinical research of very large tumors (> 3 cm) due to limited detection sensitivity of phosphorylated compounds in the human breast at 1.5 T MR systems (17).

1.4 Sensitivity of ^{31}P MRS

Although ^{31}P MRS is, due to the lower gyromagnetic ratio, far less sensitive than proton MRS, there are a number of benefits that make ^{31}P MRS more suitable to measure the PMEs and PDEs *in vivo*. With ^{31}P MRS, PMEs can be easily distinguished from PDEs due to the larger chemical shift dispersion for phosphorus. At high magnetic field it even

becomes possible to distinguish PC from PE as well as GPC from GPE (Figure 1.4a). The spectral resolution of *in vivo* proton spectroscopy is not sufficient to distinguish monoesters from diesters and only a 'total choline' signal, which also contains the (G)PEs can be measured (Figure 1.4b). Moreover, proton spectroscopy suffers from disturbing signals from lipids and water, that are many orders of magnitude larger than the metabolite signals of interest, while ^{31}P MRS is thought to be free from these disturbing signals.

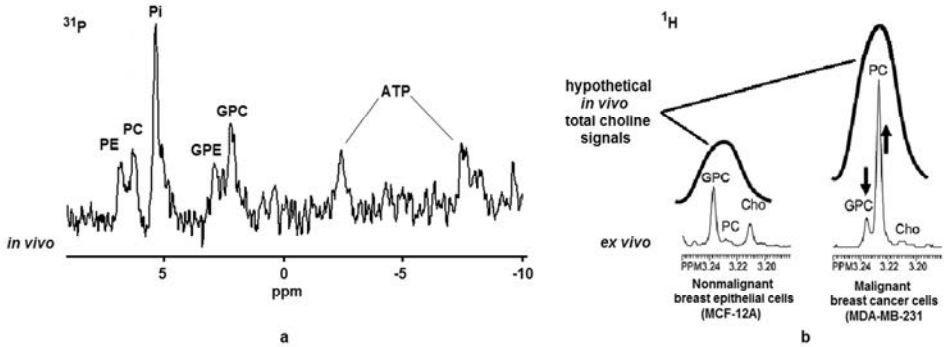

Figure 1.4. (**a**) *In vivo* ^{31}P MR spectroscopy of a voxel containing a malignant breast tumor (18). (**b**) *Ex vivo* ^{1}H NMR spectra of non-malignant breast epithelial cells and malignant breast cancer cells, with added hypothetical (lower resolution) *in vivo* signals, modified from (19).

1.5 Challenges of ultra-high field ^{31}P MRS

Signal-to-noise ratio as well as spectral resolution of ^{31}P MRS can be improved by going to higher field, as SNR and spectral resolution increase with the magnetic field strength. A drawback of going to higher field is the impediment to effectively apply proton decoupling and utilize signal enhancement by the Nuclear Overhauser Effect (NOE), which has been applied at lower field strengths (20,21). Decoupling and NOE add to RF energy deposition, which is already troublesome in ultra-high field *in vivo* MRS. Moreover, proton decoupling and NOE are less effective at ultra-high field, due to increased spectral linewidth and increased relaxation by chemical shift anisotropy over dipolar relaxation, respectively.

In addition, high magnetic field strength comes with its own specific challenges such as complicated B_0-shimming, less penetration depth of the corresponding high radio frequency (RF) pulses, more RF energy deposition of these pulses, shorter transverse

relaxation times, T_2 as well as T_2*, caused by magnetic field inhomogeneities of the main magnetic field or due to susceptibility differences between different tissues.

As the breast generally contains many glandular to lipid transitions that cannot be shimmed away, and metabolite concentrations in glandular tissue are low, ^{31}P MRS of the breast is very challenging. Moreover, ^{31}P MRS signals from the underlying pectoralis muscles may contaminate the signal from the glandular tissue, thus necessitating a form of localization. Localization of the ^{31}P MRS signal is also required to distinguish healthy glandular tissue from cancerous glandular tissue. Throughout this thesis magnetic resonance spectroscopic imaging (MRSI), also called chemical shift imaging (CSI), attained by phase encoding, is used for localization.

1.6 Thesis outline

The main theme of this thesis is developing pulse sequences for improving the SNR of ^{31}P MRS, and in particular improving SNR for the PMEs and PDEs, to enhance breast cancer detection specificity, and enable monitoring of neoadjuvant chemotherapy. This thesis is an example of progressive scientific insight. During the course of the investigation, the methods improve and are combined leading to higher SNR and the spectroscopic interpretation of the data gets more refined when more data become available.

Chapter 2 deals with a method to enhance SNR of PMEs and PDEs by combination of proton to phosphorus polarization transfer and direct detection within the same repetition time.

In chapter 3 another possibility of enhancing SNR of ^{31}P MRS, tailored for high magnetic field, is explored by combining a pulse acquire sequence with multi-echo acquisition. At high magnetic field, T_2* values are usually up to an order of magnitude smaller than T_2 values of small molecules and the rapid signal loss can be regained by a multi-echo sequence. The SNR can be increased even a factor $\sqrt{2}$ more by acquiring symmetric echoes. This method is applied in chapter 4 to measure metabolite ratios in breast glandular tissue of healthy volunteers.

Chapter 5 zooms in on the PDE signals in the breast that show odd behaviour. It appears that chemical shift values are approximately -0.5 ppm off from GPE and GPC, and T_1 and T_2 values of the PDE signals are much shorter than expected.

The methods of chapters 2 and 3 are combined in chapter 6, leading to a sequence where multi-echo direct detection is integrated with multi-echo polarization transfer (DIMEPT) to obtain the highest SNR possible.

The feasibility of monitoring neoadjuvant chemotherapy with *in vivo* ^{31}P MRS is investigated in chapter 7. This patient study is based on the method described in chapter 3. Future patient studies might benefit from the method described in chapter 6, which increases SNR even more.

References

1. Jemal A, Bray F, Center MM, Ferlay J, Ward E, Forman D. Global cancer statistics. CA Cancer J. Clin. 2011; 61: 69-90.
2. American Cancer Society. Breast Cancer Facts & Figures 2013-2014. Atlanta: American Cancer Society, Inc. 2013.
3. Houssami N, Irwig L, Simpson JM, McKessar M, Blome S, Noakes J. Sydney Breast Imaging Accuracy Study: Comparative sensitivity and specificity of mammography and sonography in young women with symptoms. Am. J. Roentgenol. 2003; 180: 935-940.
4. Majid AS, de Paredes ES, Doherty RD, Sharma NR, Salvador X. Missed breast carcinoma: pitfalls and pearls. Radiographics 2003; 23: 881-895.
5. Bluemke DA, Gatsonis CA, Chen MH, DeAngelis GA, DeBruhl N, Harms S, Heywang-Köbrunner SH, Hylton N, Kuhl CK, Lehman C, Pisano ED, Causer P, Schnitt SJ, Smazal SF, Stelling CB, Weatherall PT, Schnall MD. Magnetic resonance imaging of the breast prior to biopsy. JAMA 2004; 292: 2735-2742.
6. Boetes C, Mus RD, Holland R, Barentsz JO, Strijk SP, Wobbes T, Hendriks JH, Ruys SH. Breast tumors: comparative accuracy of MR imaging relative to mammography and US for demonstrating extent. Radiology 1995; 197: 743-747.
7. Malur S, Wurdinger S, Moritz A, Michels W, Schneider A. Comparison of written reports of mammography, sonography and magnetic resonance mammography for preoperative evaluation of breast lesions, with special emphasis on magnetic resonance mammography. Breast Cancer Res. 2001; 3: 55-60.
8. Kolb TM, Lichy J, Newhouse JH. Comparison of the performance of screening mammography, physical examination, and breast US and evaluation of factors that influence them: an analysis of 27,825 patient evaluations. Radiology 2002; 225: 165-175.
9. Bird RE, Wallace TW, Yankaskas BC. Analysis of cancers missed at screening mammography. Radiology 1992; 184: 613-617.

10. Peters NH, Borel Rinkes IH, Zuithoff NP, Mali WP, Moons KG, Peeters PH. Meta-analysis of MR imaging in the diagnosis of breast lesions. Radiology 2008; 246: 116-124.

11. Kong X, Moran MS, Zhang N, Haffty B, Yang Q. Meta-analysis confirms achieving pathological complete response after neoadjuvant chemotherapy predicts favourable prognosis for breast cancer patients. Eur. J. Cancer 2011; 47: 2084-2090.

12. Podo F, Tumor phospholipid metabolism. NMR Biomed. 1999; 12: 413-439.

13. Glunde K, Ackerstaff E, Mori N, Jacobs M A, Bhujwalla ZM, Choline Phospholipid Metabolism in Cancer: Consequences for Molecular Pharmaceutical Interventions. Mol. Pharm. 2006; 3: 496–506.

14. Aboagye EO and Bhujwalla ZM, Malignant transformation alters membrane choline phospholipid metabolism of human mammary epithelial cells. Cancer Res. 1999; 59: 80-84.

15. Katz-Brull R, Seger D, Rivenson-Segal D, Rushkin E, Degani H. Metabolic markers of breast cancer: enhanced choline metabolism and reduced choline-ether-phospholipid synthesis. Cancer Res. 2002; 62: 1966-1970.

16. Morse DL, Raghunand N, Sadarangani P, Murthi S, Job C, Day S, Howison C, Gillies RJ. Response of choline metabolites to docetaxel therapy is quantified *in vivo* by localized ^{31}P MRS of human breast cancer xenografts and *in vitro* by high-resolution ^{31}P NMR spectroscopy of cell extracts. Magn. Reson. Med. 2007; 58: 270-280.

17. Leach MO, Verrill M, Glaholm J, Smith TA, Collins DJ, Payne GS, Sharp JC, Ronen SM, McCready VR, Powles TJ, Smith IE. Measurements of human breast cancer using magnetic resonance spectroscopy: a review of clinical measurements and a report of localized ^{31}P measurements of response to treatment. NMR Biomed. 1998; 11: 314-340.

18. Klomp DWJ, Bank BL van de, Raaijmakers A, Korteweg MA, Possanzini C, Boer VO, Berg CAT van de, Bosch MAAJ van de, Luijten PR. ^{31}P MRSI and ^{1}H MRS at 7 T: initial results in human breast cancer. NMR Biomed. 2011; 24: 1337–1342.

19. Glunde K, Jie C, Bhujwalla ZM. Molecular causes of the aberrant choline phospholipid metabolism in breast cancer. Cancer Res. 2004; 64: 4270-4276.

20. Luyten PR, Bruntink G, Sloff FM, Vermeulen JW, van der Heijden JI, den Hollander JA, Heerschap A. Broadband proton decoupling in human ^{31}P NMR spectroscopy. NMR Biomed. 1989; 1: 177-183.

21. Bachert-Baumann P, Ermark F, Zabel HJ, Sauter R, Semmler W, Lorenz WJ. *In vivo* nuclear Overhauser effect in ^{31}P–(^{1}H) double-resonance experiments in a 1.5-T whole-body MR system. Magn. Reson. Med. 1990; 15: 165–172.

CHAPTER 2

Increase in SNR for ^{31}P MR spectroscopy by combining polarization transfer with a direct detection sequence

WJM van der Kemp, VO Boer, PR Luijten, Wijnen JP, DWJ Klomp.
Magnetic Resonance in Medicine. 2012; 68: 353-357.

2.1 Introduction

Phosphomonoesters (PME) and phosphodiesters (PDE) are involved in phospholipid metabolism and have shown clinical potential to be used as biomarkers in oncology and neurological disorders (1-10). The concentration of these metabolites can be obtained using ^{31}P MRS. However, direct ^{31}P measurement *in vivo* is hampered by an intrinsic low sensitivity. Enhancement of signal-to-noise ratio (SNR) can be obtained by increasing the magnetic field (B_0) and by ^{1}H to ^{31}P polarization transfer (PT) techniques. For instance a RINEPT (11) (refocused insensitive nuclei enhanced polarization transfer), a sRINEPT (selective RINEPT) (12,13) or its adiabatic variant the BINEPT (14,15) have been shown to effectively transfer the stronger polarization of proton spins to the phosphorus spins.

Due to interfering inter-proton coupling, the intrinsic signal intensity for a (B/R)INEPT and direct ^{31}P detection are approximately equal (16). With a sRINEPT, the inter-proton coupling is refocused, but its increased sensitivity is almost lost by additional T_2 relaxation. However, as these polarization transfer techniques are based on polarization of a complete different pool of spins (^{1}H) compared to direct detection (^{31}P), the SNR per unit of time will be more favorable since $T_1(^{1}\text{H}) << T_1(^{31}\text{P})$ (12,16).

The signal intensity obtained with a ^{1}H to ^{31}P polarization-transfer sequence is related to the population difference of the ^{1}H spins. Apart from B_0 magnetic field strength, this difference is related to perturbation and T_1 relaxation of proton spins prior to excitation. This implies that this signal intensity is independent of any perturbation or relaxation of ^{31}P spins prior to excitation. Polarization transfer leads to ^{31}P spin population differences (polarization), and subsequent ^{31}P excitation, irrespective whether there is Boltzmann

equilibrium (full relaxation) of the ^{31}P spins or not. When using a polarization-transfer technique that contains a segmented BIR-4 zero degree pulse on the ^{31}P channel (Figure 2.1, BINEPT), there is no direct excitation of ^{31}P spins by the BINEPT, only the transferred polarization is excited. Therefore, direct detection can be combined with polarization-transferred detection within the same scan time without compromising SNR of the polarization-transferred signal. In fact, combining these signals will result in enhanced SNR for coupled spins, but also provides information of spins that are not detected by polarization transfer sequences.

Using phantom measurements we first demonstrate that direct ^{31}P detection can be merged into a polarization-transfer sequence without affecting the polarization-transfer SNR.

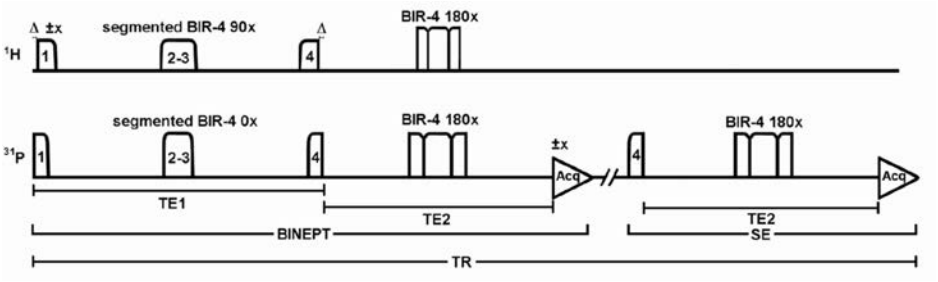

Figure 2.1. Combined BINEPT-SE sequence used for ^{31}P MR spectroscopy. Pulse parameters for the ^{1}H channel. Segmented BIR-4 90°: frequency sweep 8.0 kHz, γB_{1max} = 962 Hz, duration per segment 2.5 ms; BIR-4 180°: frequency sweep 13.3 kHz, γB_{1max} = 1435 Hz, duration 6.0 ms. Pulse parameters for the ^{31}P channel: segmented BIR-4 0°: frequency sweep 10.0 kHz, γB_{1max} = 1400 Hz, duration per segment 2.0 ms; BIR-4 180°: frequency sweep 10.0 kHz, γB_{1max} = 1700 Hz, duration 8.0 ms.

With the aim of being able to detect very small concentrations of phospholipid metabolites, we implemented the adiabatic version of a polarization transfer (BINEPT) technique for 7 T, and combined this with an adiabatic direct ^{31}P detection sequence. *In vivo* validation of the combination of the polarization-transfer sequence with the additional adiabatic direct ^{31}P detection was performed in the human calf muscle where ATP and PDE are highly abundant. Using a sensitivity optimized quadrature transmit and receive breast coil double tuned to ^{1}H and ^{31}P, we demonstrate the optimal detection of very-low concentrations of PMEs and PDEs in the healthy human breast with the BINEPT, whilst enabling the detection of the non ^{1}H-coupled signals of inorganic phosphate and ATP at the same time.

2.2 Experimental

2.2.1 Implementation of combined polarization transfer with direct detection

An adiabatic version of the polarization-transfer sequence (BINEPT) was used to minimize sensitivity to the non-uniformities in B_1 fields that are observed at 7 T. The modulation functions for the segmented adiabatic BIR-4 0° and the BIR-4 180° pulses were adopted from Garwood and Ke (17). In this approach the B_1 field f_b and the frequency sweep ω_1 of the four segments of the BIR-4 are given by

$$f_b = f_{b\max}\tanh\left[\zeta\cdot(1-\tau)\right] \quad \text{and} \quad \omega_1(\tau) = \frac{sw_{\max}\cdot\tan(\kappa\tau)}{\tan(\kappa)} \qquad \text{for } 0 \le t \le \tfrac{1}{4}T_{\mathrm{p}} \qquad [2.1]$$

$$f_b = f_{b\max}\tanh\left[\zeta\cdot(\tau-1)\right] \quad \text{and} \quad \omega_1(\tau) = \frac{sw_{\max}\cdot\tan(\kappa\tau-2)}{\tan(\kappa)} \qquad \text{for } \tfrac{1}{4}T_{\mathrm{p}} < t \le \tfrac{1}{2}T_{\mathrm{p}} \qquad [2.2]$$

$$f_b = f_{b\max}\tanh\left[\zeta\cdot(3-\tau)\right] \quad \text{and} \quad \omega_1(\tau) = \frac{sw_{\max}\cdot\tan(\kappa\tau-2)}{\tan(\kappa)} \qquad \text{for } \tfrac{1}{2}T_P < t \le \tfrac{3}{4}T_{\mathrm{p}} \qquad [2.3]$$

$$f_b = f_{b\max}\tanh\left[\zeta\cdot(\tau-3)\right] \quad \text{and} \quad \omega_1(\tau) = \frac{sw_{\max}\cdot\tan(\kappa\tau-4)}{\tan(\kappa)} \qquad \text{for } \tfrac{3}{4}T_P < t \le T_{\mathrm{p}} \qquad [2.4]$$

where $\zeta = 10$, $\tan(\kappa) = 20$ and $\tau = 4t/T_{\mathrm{p}}$ with t, time, T_{p} the total pulse duration, $f_{b\max}$ the maximum B_1 field expressed as γB_1 and $sw_{\max}$ the maximum frequency sweep. A limitation of our MR system is that pulses on different channels cannot have the same starting time. For this reason the combined sequence was implemented as depicted in Figure 2.1, in which the reference points of segment 1 and segment 4 of the segmented BIR-4 pulses on the two channels are shifted by $\Delta = 0.5$ ms, similar to that reported by Klomp *et al.* (12). Details about the applied adiabatic pulses are summarized in the figure legend.

Adiabaticity of the pulses was verified by assessing SNR variations in phantom experiments when lowering the used B_1 values of the pulses at both the ^{1}H and the ^{31}P channel. The optimal echo times, $TE1$ = 41 ms and $TE2$ of 34 ms, were obtained at 7 T through quantum mechanical simulations (TOPSPIN, Bruker Biospin, Billerica, MA, USA) and in a phantom measurement containing phosphoethanolamine (PE) and phosphocholine (PC). Since the spectral line widths observed *in vivo* are substantially larger than the J-coupling values between the ^{31}P and ^{1}H spins, no ^{1}H decoupling has been applied. Likewise Nuclear Overhauser enhancement techniques have been omitted for their effects may be marginal due to dominance of chemicals shift anisotropic relaxation for most ^{31}P nuclei at higher fields (18).

For accurate comparison to the polarization-transfer sequence, the direct detection method is performed with the same RF pulses and echo time (*TE*2) as used in the ^{31}P spin-echo part of the BINEPT sequence (Figure 2.1). Therefore, RF pulse profiles and T_2 effects have minimal effect on SNR differences. Although it is expected that the SE sequence would not affect the signals obtained with the BINEPT, the BINEPT will affect the signals obtained with the SE, which is due to the BIR-4 180° pulse of the BINEPT on the phosphorus channel that leads to partial inversion of longitudinal ^{31}P magnetization. The steady-state longitudinal magnetization $M_{z,ss}$ of such an inversion-recovery sequence (*i.e.* ^{31}P part of the BINEPT sequence) with spin-echo detection can be written as

$$M_{z,ss} = M_0(1 - 2e^{-T_I/T_1} + 2e^{-(T_R - TE/2)/T_1} - e^{-T_R/T_1}), \quad [2.5]$$

where T_I is the inversion time, the delay between BINEPT and SE. Since, in the case of our implementation of the combined BINEPT-SE, the inversion time T_I = ½T_R (there are two inversion pulses approximately equidistant in one T_R) and $TE << T_R$, equation [2.5] can be simplified to

$$M_{z,ss} = M_0(1 - e^{-T_R/2T_1}). \quad [2.6]$$

The other pulses on the ^{31}P channel do not affect the SE signal since the segmented BIR-4 0° pulse on the ^{31}P channel causes an identity transformation and no direct excitation.

2.2.2 Measurements

As a proof of principle, ^{31}P MRS measurements were obtained with a BINEPT sequence and a direct detection sequence (adiabatic SE, with the same *TE*(^{31}P) of 34 ms as used in the BINEPT) at various T_R for each sequence separately, and combined within the same T_R. A spherical phantom of 4 cm in diameter, filled with 12 mM PE and 15 mM PC solution buffered to pH = 7.0, was used and submersed in a larger semi-sphere filled with NaCl solution for RF loading of the coil, similar as the loading of the human breast. Measurements were performed with a whole body 7 T MR system (Philips, Cleveland, USA) using a sensitivity-optimized unilateral dual-tuned quadrature coil (19). Since ^{1}H decoupling and NOE techniques are excluded from the measurements, RF power deposition remained well within SAR guidelines (20).

The sequence was tested on the calf muscle of a male volunteer using a T_R of 5 s and 60 averages and, for comparison to a BINEPT, with T_R of 5 s and 64 averages. To explore the feasibility in detecting low concentrations of phosphorylated metabolites, the combined BINEPT-SE sequence was applied *in vivo* to the breast of a healthy female volunteer. The volunteer was positioned in prone position, with her left breast in the quadrature coil setup. The combined sequence was applied to the subject using a T_R of 5 s with 128 averages. Written informed consent was obtained from the volunteers and the study was approved by the local medical ethics review board.

2.3 Results

B_1 measurements obtained from the loaded phantom were used to assess the performance of the adiabatic RF pulses. Simulated frequency profiles of the pulses show accurate flip angles (>95%), over the chemical shift range of interest of 3.8 ppm, that comprises the PMEs and PDEs, even in the regime of 60% of the applied B_1 (Figure 2.2).

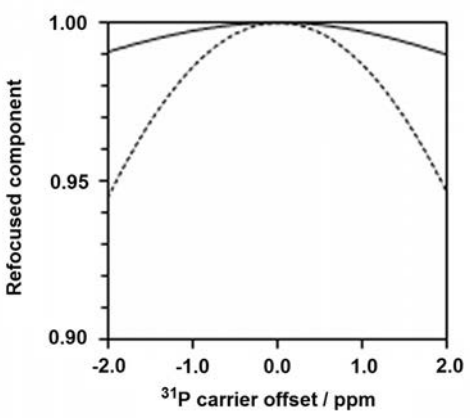

Figure 2.2. Simulated frequency profile of the refocused component of the BIR-4 180° refocusing pulse at a γB_{1max} of 1700 Hz (solid line) and 1000 Hz (dashed line), *i.e.* at 100% and 60 % of the nominal max. B_1.

Phantom measurements have demonstrated that more than 95% of the original SNR is obtained when applying the RF pulses at 60% of the nominal B_1 (data not shown). Phantom measurements obtained with the BINEPT and SE sequence demonstrate substantial different signal attenuation with respect to T_R (Figure 2.3a-d). However, when combining the SE sequence with the BINEPT, the SNR levels of the BINEPT (Figure 2.3a) remain similar to the single BINEPT (Figure 2.3c). The decrease in SNR with increasing T_R is caused by less sample averages at higher T_R, as the total scan duration per spectrum is kept constant. The signal attenuation observed in the SE part of the combined sequence is caused by the inversion recovery, as described by equation [2.6]. A fit to the data results in T_1 values of 6.2 ± 0.1 s and 5.5 ± 0.1 s for PC and PE respectively,

see Figure 2.3e. These values correspond well to the T_1-values obtained using the SE sequence exclusively, 5.9 ± 0.1 s and 5.6 ± 0.1 s (data not shown).

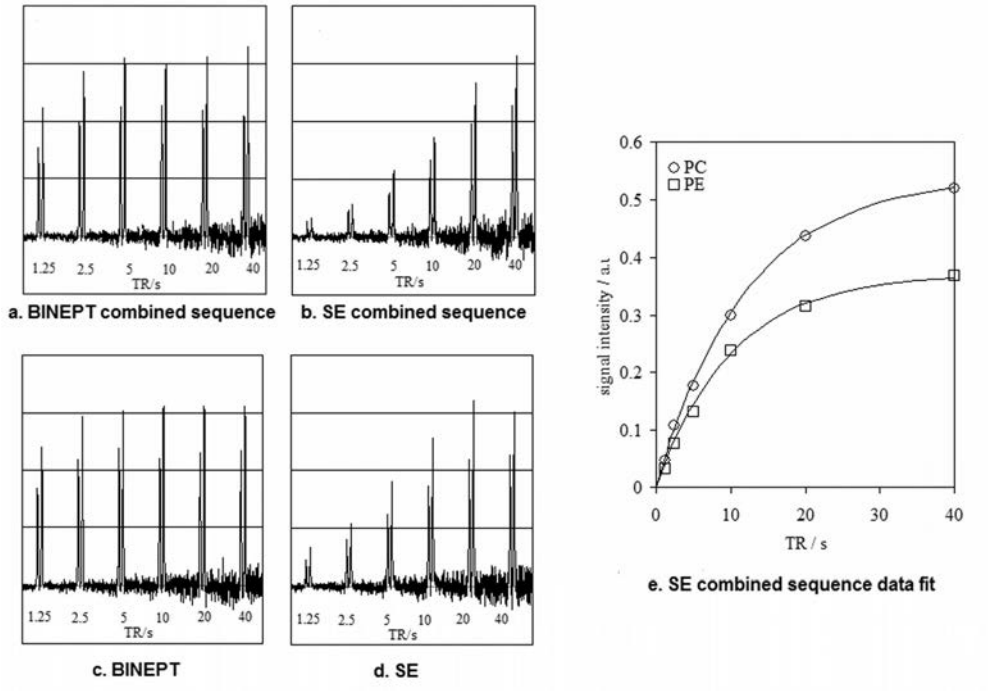

Figure 2.3. Measured ^{31}P MRS data on a PC and PE containing phantom. ^{31}P MR spectra for a combined BINEPT – SE sequence (**a,b**) and for separate BINEPT (**c**) and SE (**d**) sequences at various T_R, with fixed scan times of 80 s. Note that the BINEPT is hardly affected by an additional ^{31}P MR SE experiment in one T_R. (**e**) Measured SE(combined sequence) signal intensities of PC and PE in the phantom, fitted to equation [2.6]. The T_1-values obtained from the fit were 6.2 s for PC and 5.5 s for PE.

The combined sequence can be applied to obtain a BINEPT at the same SNR in the same time that one would need to obtain a normal BINEPT MR spectrum, but now with all the additional information that direct detection provides. This is shown in Figure 2.4 for ^{31}P MR spectra of the calf muscle of a healthy male volunteer. Note that in the direct detected ^{31}P MR spectra, the resonances of the PMEs overlap with levels of phosphate sugars.

The ^{31}P breast MR spectra of a healthy female volunteer are shown in Figure 2.5. Here the combined $[\text{BINEPT} + \text{SE}]_{NSA=128}$ MR spectra show well-separated and artefact-free resonances of PME and PDE in the BINEPT data (Figure 2.5a), while in addition, Pi and ATP resonances are observed in the SE data (Figure 2.5b).

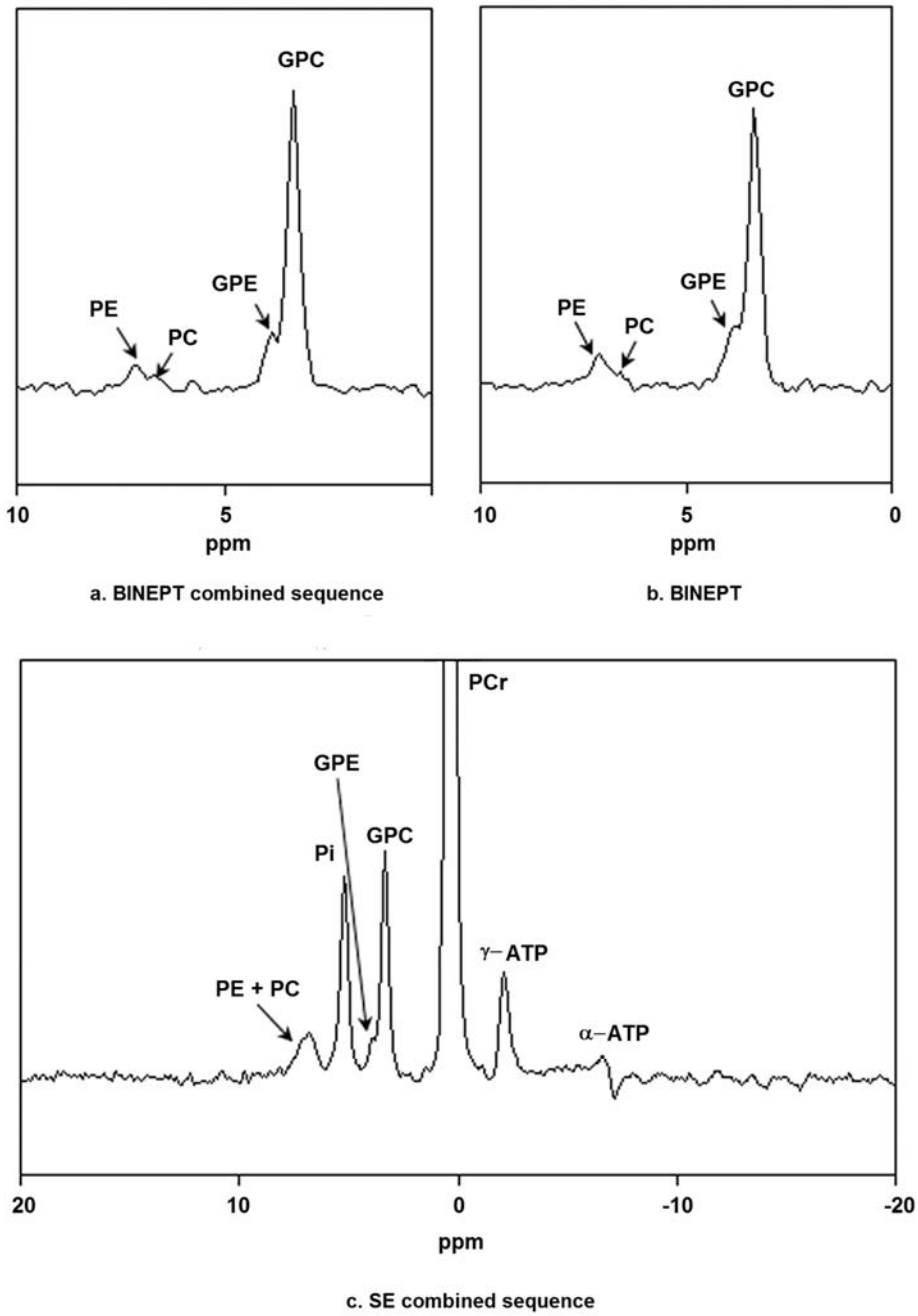

Figure 2.4. ^{31}P MR spectra of the calf muscle of a healthy male volunteer. Combined $[\text{BINEPT + SE}]_{NSA=60}$ (**a,c**) sequence; and separate $[\text{BINEPT}]_{NSA=64}$ (**b**) sequence. Repetition time $T_R = 5$ s. All MR spectra are scaled to the same noise.

Without sacrificing SNR, nor scan-time, the combined BINEPT and SE MR spectra provide more metabolite information than MR spectra obtained with a BINEPT alone. Also note that both the BINEPT as well as the SE MR spectra have signals from PME and PDE while their noise is uncorrelated, which will improve SNR of these signals when applying weighted averaging. Since localization techniques have not been implemented in this sequence, large contaminating signals from PCr in the chest muscle are observed in the direct detected MR spectra.

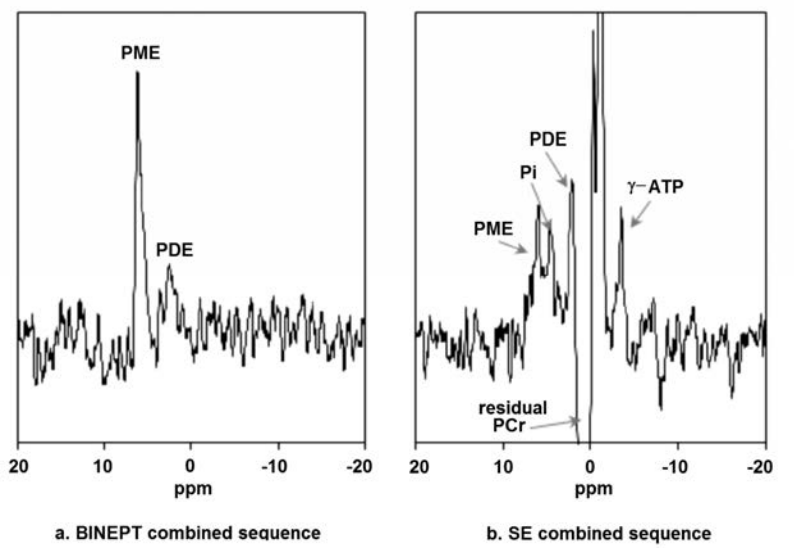

Figure 2.5. ^{31}P breast MR spectra of a healthy female volunteer with the combined [BINEPT(a) + SE(b)]$_{NSA=128}$ sequence, with an effective T_R of 5 s. Note that these spectra are obtained from very low concentrated phospholipid metabolites in the healthy human breast.

As the chest muscle is outside the coil volume, signals from the muscle, such as PCr, are out of phase because the adiabatic condition has not been reached due to the low B_1 field in the muscle. Based on the signal of Pi in the SE spectrum, the linewidth can be determined as approximately 65 Hz.

2.4 Discussion

This study shows that polarization transfer, *e.g.* using BINEPT, and an adiabatic direct detection method can be combined in one repetition time without compromising the

intensity of the polarization-transferred signal. However, the signal from direct detection is impeded because the BIR-4 180° pulse from the BINEPT on the ^{31}P channel acts as an inversion pulse for the longitudinal ^{31}P magnetization, giving rise to an inversion-recovery sequence for direct detection. In the present implementation of the combined sequence, the BINEPT and the SE sequence each comprise half T_R, giving rise to a SE signal proportional to Eq. [2.6]. However, this latter signal can be maximized by making the inversion time, *i.e.* the time between the BIR-4 180° and the adiabatic half passage of the direct excitation sequence on the ^{31}P channel, as short as possible, without compromising the acquisition time of the BINEPT.

Chemical shift dispersion is increased at higher field strength, making spectral resolution of PC and PE and their glycerol derivatives possible under favorable conditions. However, in the human breast spectral resolution is hampered by susceptibility differences between fat and glandular tissue as well as by fluctuating magnetic fields from breathing and heart beat, so that at present only the sum signals of PC, PE (*i.e.* PME) and GPC, GPE (*i.e.* PDE) can be observed in Figure 2.5. Respiratory and cardiac gating, or dynamic shimming, can mitigate the disturbing dynamic influences on the acquired signal, such that the peaks of the individual metabolites may be observed. In order to be more useful for breast cancer evaluation, MR spectra may need to be spatially resolved, which can be realized by integrating CSI in the combined sequence.

In calf muscle, shimming conditions are more favorable than in the breast and PC, PE and GPC, GPE can be resolved as shown in Figure 2.4. The α-ATP signal in Figure 2.4c is out of phase and the β-ATP signal is absent because the bandwidth of the adiabatic refocusing pulse (BIR-4 180°, Figure 2.2) is limited. Although a SE was chosen as a direct detection method, a conventional pulse acquire sequence can be used as well, which may include an excitation pulse with a higher bandwidth. Because of the short T_2* at 7 T and consequently broad line widths that already at 3 T can go up to 62 Hz (21) in the breast, proton decoupling for spins that have J-coupling values of only 6 Hz may not improve spectral resolution or SNR. In fact, by avoiding proton decoupling, shorter T_R-values can be used without violating SAR guidelines, hence maximizing SNR per unit of time.

^{31}P MRS is less sensitive than ^{1}H MRS, however, as shown in this study, polarization can be transferred from ^{1}H to ^{31}P in human subjects even at the field strength of 7 T for increased SNR. In addition, using both ^{1}H and ^{31}P pools, the sensitivity of ^{31}P MRS is increased even further. In fact, in contrast to ^{31}P MRS studies reported at 1.5T (16,22), even in healthy human breasts, low levels of PMEs and PDEs can now be obtained within

clinically acceptable acquisition times. Rather than studying the total choline pool with ^{1}H MRS, multiple metabolites in choline metabolism can be assessed with ^{31}P MRS, which may improve specificity in grading tumors and monitoring of anti-cancer treatment response (22).

2.5 Conclusions

Polarization transfer, *e.g.* using BINEPT, and direct detection techniques can be combined in one repetition time without compromising the intensity of the polarization transferred signal. The SNR per time unit of the ^{31}P MRS signals of PMEs and PDEs can therefore be increased by using an combined BINEPT - SE sequence. Or alternatively, the combined BINEPT - SE sequence can be used to obtain a BINEPT at the same SNR, but at the same time with the additional information on metabolite content (Pi, PCr, ATP) that direct detection offers.

References

1. Negendank W. Studies of human tumors by MRS: a review. NMR Biomed. 1992; 5: 303-324.
2. Leach MO, Verrill M, Glaholm J, Smith TA, Collins DJ, Payne GS, Sharp JC, Ronen SM, McCready VR, Powles TJ, Smith IE. Measurements of human breast cancer using magnetic resonance spectroscopy: a review of clinical measurements and a report of localized ^{31}P measurements of response to treatment. NMR Biomed. 1998; 11: 314-340.
3. Aboagye EO and Bhujwalla ZM. Malignant transformation alters membrane choline phospholipid metabolism of human mammary epithelial cells. Cancer Res. 1999; 59: 80-84.
4. Podo F. Tumour phospholipid metabolism. NMR Biomed. 1999; 12: 413–439.
5. Podo F, Canevari S, Canese R, Pisanu ME, Ricci A, Iorio E. MR evaluation of response to targeted treatment in cancer cells. NMR Biomed. 2011; 24: 648-672.
6. Kato T, Inubushi T, Kato N. Magnetic resonance spectroscopy in affective disorders. J. Neuro-psychiatry Clin. Neurosci. 1998; 10: 133-47.
7. Valenzuela MJ, Sachdev P. Magnetic resonance spectroscopy in Alzheimer disease. Neurology 2001; 56: 592-598.
8. Yildiz A, Sachs GS, Dorer DJ, Renshaw PF. ^{31}P Nuclear magnetic resonance spectroscopy findings in bipolar illness: a meta-analysis. Psychiatry Res. 2001;106:181-191.

9. Reddy R and Keshavan MS. Phosphorus magnetic resonance spectroscopy: its utility in examining the membrane hypothesis of schizophrenia. Prostaglandins, Leukotrienes and Essential Fatty Acids 2003; 69: 401–405.

10. Stanley JA, Kipp H, Greisenegger E, MacMaster FP, Panchalingam K, Pettegrew JW, Keshavan MS, Bukstein OG. Regionally specific alterations in membrane phospholipids in children with ADHD: an *in vivo* ^{31}P spectroscopy study. Psychiatry Res. 2006; 148: 217–221.

11. Burum DP and Ernst RR. Net polarization transfer via a J-ordered state for signal enhancement of low-sensitivity nuclei. J. Magn. Res. 1980; 39: 163-168.

12. Klomp DWJ, Wijnen JP, Scheenen TWJ, Heerschap A. Efficient ^{1}H to ^{31}P polarization transfer on a clinical 3 T MR system. Magn. Reson. Med. 2008; 60: 1298-1305.

13. Kemp WJM van der, Boer VO, Luijten PR, Klomp DWJ. Full ^{1}H to ^{31}P polarization transfer on 7 tesla, Proceedings of the joint annual meeting ISMRM-ESMRMB, International Society of Magnetic Resonance in Medicine, Stockholm, 2010.

14. Merkle H, Wei H, Garwood M, Uğurbil K. B_1-Insensitive heteronuclear adiabatic polarization transfer for signal enhancement. J. Magn. Reson. 1992; 99: 480-494.

15. Payne GS and Leach MO. Surface-coil polarization transfer for monitoring tissue metabolism *in vivo*. Magn. Reson. Med. 2000; 43: 510–516.

16. Mancini L, Payne GS, Leach MO. Comparison of polarization transfer sequences for enhancement of signals in clinical ^{31}P MRS studies. Magn. Reson. Med. 2003; 50: 578-588.

17. Garwood M and Ke Y. Symmetric pulses to induce arbitrary flip angles with compensation for RF inhomogeneity and resonance offsets. J. Magn. Reson. 1991; 94: 511-525.

18. Mathur-deVré R, Maerschalk C, Delporte C. Spin lattice relaxation times and nuclear Overhauser effect for ^{31}P metabolites in model solutions at two frequencies: implications for *in vivo* spectroscopy. Magn. Reson. Imag. 1990; 8: 691-698.

19. Klomp DWJ, Bank BL van de, Raaijmakers A, Korteweg MA, Possanzini C, Boer VO, Berg CAT van de, Bosch MAAJ van de, Luijten PR. ^{31}P MRSI and ^{1}H MRS at 7 T: initial results in human breast cancer. NMR Biomed. 2011; 24: 1337-1342.

20. International Electrotechnical Commission (IEC). IEC 60601-2-33. Medical electrical equipment. Part 2-33: Particular requirements for the safety of magnetic resonance equipment for medical diagnosis. IEC 60601-2-33 Ed. 3:2010. Geneva: IEC; 2010.

21. Hu J, Feng W, Hua J, Jiang Q, Xuan Y, Li T, Haacke EM. A high spatial resolution *in vivo* ^{1}H magnetic resonance spectroscopic imaging technique for the human breast at 3 T. Med. Phys. 2009; 36: 4870-4877.

22. Glaholm J, Leach MO, Collins DJ, Mansi J, Sharp JC, Madden A, Smith IE, McCready VR. *In vivo* ^{31}P magnetic resonance spectroscopy for monitoring treatment response in breast cancer. Lancet 1989; 333: 1326–1327.

CHAPTER 3

Adiabatic Multi-Echo ^{31}P Spectroscopic ImagiNG (AMESING) at 7 tesla for measuring transverse relaxation times and regaining sensitivity in tissues with short T_2* values

WJM van der Kemp, VO Boer, PR Luijten, BL Stehouwer, WB Veldhuis, and DWJ Klomp.
NMR in Biomedicine 2013; 26: 1299-1307.

3.1 Introduction

Metabolites containing phosphorus play an important role in energy metabolism and phospholipid metabolism. Phospholipid metabolism, involving the phosphomonoesters (PME): phosphocholine (PC) and phosphoethanolamine (PE), and the phosphodiesters (PDE): glycerophosphocholine (GPC) and glycerophosphoethanolamine (GPE), is altered in many cancers (1-5). In contrast to proton Magnetic Resonance Spectroscopy (^{1}H MRS), the signals of these metabolites can be measured by ^{31}P MRS without the necessity of water or fat suppression. Additionally, while clinical *in vivo* proton MRS only leads to a 'total-choline' signal (including all PME and PDE metabolites), ^{31}P MRS can spectrally resolve PME and PDE metabolites. However, ^{31}P MRS is hampered by an intrinsic low sensitivity that can be as low as 6.7% of the sensitivity achieved with proton spectroscopy. This is due to the fact that the gyromagnetic ratio of phosphorus spins is 2.5 times lower than that for proton spins and the intrinsic sensitivity is proportional to γ^3 (6). Signal-to-noise ratio (SNR) in ^{31}P MRS is further impeded by long longitudinal relaxation times.

Apart from increased SNR at higher magnetic fields, T_1 relaxation times of ^{31}P spins are reduced, while due to tissue loss dominance of the receiver coils, the intrinsic sensitivity approaches a quadratic rather than third power dependence on the gyromagnetic ratio.

Moreover, the SNR in ^{31}P MRS can be enhanced even further by using polarization transfer techniques (7-9) or by using the Nuclear Overhauser Effect (NOE) (10-12).

However, in MRSI of tissues with strong susceptibility transitions, one often has to deal with a bad B_0 shimming leading to a large loss in SNR because of short T_2* values and the accompanying line broadening. Of course, in organs and locations where susceptibility differences are small, or extend significantly beyond the boundaries of the sample studied, T_2* can be long, particularly with good B_0 shimming. Therefore, MRS is very successful in many areas in the brain (13), prostate (14) or even inside relatively large tumors (15,16). But in the human breast B_0 shimming is more problematic. The human breast contains many small glandular-to-lipid transitions that cannot be shimmed away due to their differences in susceptibility. Even after third order shim field corrections, the high number of glandular-to-lipid transitions generally present in the breast will cause a non-uniform B_0 field. A good B_0 shim can only be obtained for voxels that solely contain glandular tissue, or in case of large tumors that remain well within its boundaries avoiding the transitions to lipids. But in small breast tumors, or even large breast tumors that have necrotic areas or lipid layers within the tumor (for instance caused by neoadjuvant chemotherapy), conventional B_0 shimming is usually poor. Dynamic shimming, however, may be of benefit for improving B_0 fluctuations in time (17), and as a consequence SNR and spectral resolution, not only for the FID but also for multi-echo acquisitions. In cases where shimming is good, the multi-echo approach would require fewer echoes, and less SAR deposition to obtain good quality spectra.

The loss of SNR, due to susceptibility effects can be regained by using multi-echo (18-21) sequences. The multi-echo approach for regaining SNR is especially suitable for higher magnetic field strengths, where susceptibility effects are strong. These effects lead to reduced T_2* values, while the T_2 of many ^{31}P metabolites is an order of magnitude larger than T_2*. In addition, the increased chemical shift dispersion at higher magnetic field strengths provides less constraints to the spectral resolution, thereby permitting the reduction of the acquisition duration and hence increasing the number of echoes per unit of T_2.

Here we implemented an Adiabatic Multi-Echo Spectroscopic ImagiNG (AMESING) sequence with spherical k-space sampling (Figure 3.1) on a whole body 7 tesla MR system (Philips, Cleveland, USA). Spatial encoding is done using compensated phase encoding gradients, *i.e.* the echoes are not used for speeding up k-space sampling but for averaging and even enabling T_2 measurements of ^{31}P metabolites, while excluding T_2-dependent spatial blurring.

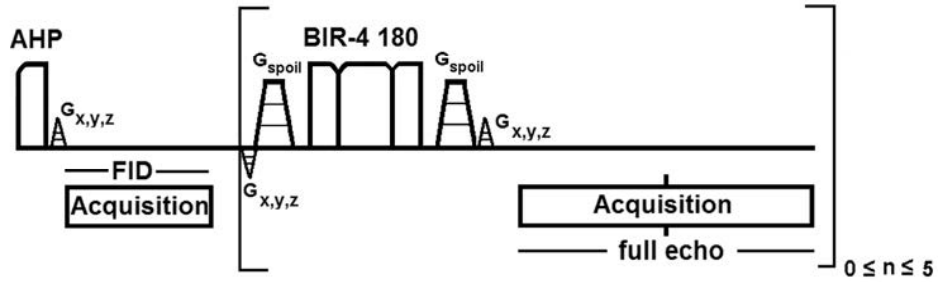

Figure 3.1. Adiabatic Multi-Echo Spectroscopic ImagING (AMESING) sequence used for ^{31}P MRS, acquiring a total of 1 FID and n symmetric echoes in one T_R. An adiabatic half passage pulse was used for excitation and BIR-4 180° pulses for refocusing.

The signals of the FID and the full echoes are combined in order to maximize SNR per unit of time. T_2-weighted averaging can be applied for each metabolite separately, resulting in optimized SNR enhancement compared to a pulse-acquire sequence, even when applied at the Ernst angle (21). Note that Ernst-angle excitation leads to an SNR improvement of only 11% as compared to a 90 degree excitation with a longer T_R of $1.26T_1$. For metabolite quantification the signal from the AMESING sequence extrapolated from the T_2 fit to $t = 0$ ms can be used including correcting for coil sensitivity as described by Wijnen *et al.* (22).

Here we demonstrate the validation of the AMESING sequence on the calf muscle and the regaining of SNR in the detection of low-concentrated ^{31}P metabolites in the breast, obtained in a healthy female volunteer and in a breast cancer patient. The study was approved by the local medical ethics review board and written informed consent was obtained from the volunteers and the patient.

3.2 Theory

With the AMESING sequence, the FID signal and multiple echoes can be acquired. These are combined to maximize the SNR. In the following it is assumed that $T_2^* << T_2$ and $T_{acq} \geq 1.26T_2^*$, making a multi-echo approach useful. A T_{acq} of $1.26T_2^*$ for a FID and $2.52T_2^*$ for a full echo leads to an optimal SNR when no filtering is applied (21). As maximizing SNR is a main objective, it is evident to sample the full echoes, that contain $\sqrt{2}$ more SNR, instead of half echoes. For illustrative purposes we consider two methods for combining the FID and the echoes: averaging and weighted averaging. The n symmetric echoes of the AMESING sequence can be considered equivalent to $2n$ half echoes (*i.e.* equivalent to $2n$

times the FID signal). The summed signal of the two echo parts of a symmetric echo can be written as

$$S_i = 2S_0 e^{-i\Delta TE / T_2}\,, \qquad [3.1]$$

The average S_a of the FID signal, S_0, with n symmetric echoes (i)
can be written as

$$S_a = \frac{S_0}{2n+1}\left(1 + 2\sum_{i=1}^{n} e^{-i\Delta TE / T_2}\right), \qquad [3.2]$$

where S_0 denotes the FID, S_i with i = 1 to n the echoes, ΔTE the echo time step and T_2 the transverse relaxation time of a specific metabolite. The noise σ_a of the average signal is given by:

$$\sigma_a^2 = \frac{\sigma_0^2}{2n+1}, \qquad [3.3]$$

leading to a SNR for the average signal of

$$SNR_a = SNR_0 \cdot \frac{1 + 2\sum_{i=1}^{n} e^{-i\Delta TE / T_2}}{\sqrt{2n+1}}, \qquad [3.4]$$

where $SNR_0 = S_0/\sigma_0$.

The enhancement in SNR of signal averaging E_a, as compared to a single FID acquisition is

$$E_a = \frac{1 + 2\sum_{i=1}^{n} e^{-i\Delta TE / T_2}}{\sqrt{2n+1}}. \qquad [3.5]$$

In case of weighted averaging of signals, the signals will be multiplied by a weighting factor w_i and divided by the sum of the weighting factors. Therefore, the weighted average signal can be written as

$$S_{wa} = \frac{w_0 S_0 + \sum_{i=1}^{n}\left[S_i \cdot w_i\right]}{w_0 + 2\sum_{i=1}^{n} w_i}, \qquad [3.6]$$

with S_i given by equation [3.1]. The weighted average noise can be written

$$\sigma_{\mathrm{wa}}^2 = \sigma_0^2 \cdot \frac{w_0^2 + 2\sum_{i=1}^{n} w_i^2}{\left[w_0 + 2\sum_{i=1}^{n} w_i \right]^2}, \qquad [3.7]$$

where it is used that the noise for every signal, FID or (half) echo, is σ_0^2. We now substitute

$$w_0 = 1 \text{ and } w_i = e^{-i\Delta TE / T_2}, \qquad [3.8]$$

for the weights, and equation [3.1] for the signals, in equations [3.6] and [3.7]. The weighted average signal can then be written as

$$S_{\mathrm{wa}} = S_0 \cdot \frac{1 + 2\sum_{i=1}^{n} e^{-2i\Delta TE / T_2}}{1 + 2\sum_{i=1}^{n} e^{-i\Delta TE / T_2}}, \qquad [3.9]$$

and the weighted average noise as

$$\sigma_{\mathrm{wa}}^2 = \sigma_0^2 \cdot \frac{1 + 2\sum_{i=1}^{n} \left[e^{-2i\Delta TE / T_2} \right]}{\left[1 + 2\sum_{i=1}^{n} e^{-i\Delta TE / T_2} \right]^2}. \qquad [3.10]$$

Combining [3.9] with the square root of [3.10] leads to the weighted average SNR_{wa}

$$SNR_{\mathrm{wa}} = SNR_0 \cdot \sqrt{1 + 2\sum_{i=1}^{n} e^{-2i\Delta TE / T_2}} \qquad [3.11]$$

and the SNR enhancement of the weighted average signal is given by

$$E_{\mathrm{wa}} = \sqrt{1 + 2\sum_{i=1}^{n} e^{-2i\Delta TE / T_2}}. \qquad [3.12]$$

Figure 3.2a and 3.2b show enhancement in SNR for signal averaging and weighted averaging, equations [3.5] and [3.12] respectively, as a function of $T_2/\Delta TE$ and number of signals $2n$+1: 1 FID and n symmetric echoes. The weighted average model shows a higher enhancement for all T_2 values. Both models predict that for $T_2 \rightarrow \infty$, the enhancement approaches $\sqrt{2n+1}$. For very short T_2, the averaging model even leads to a SNR decrease with $1/\sqrt{2n+1}$, while the weighted average model enhancement remains $\geq$1.

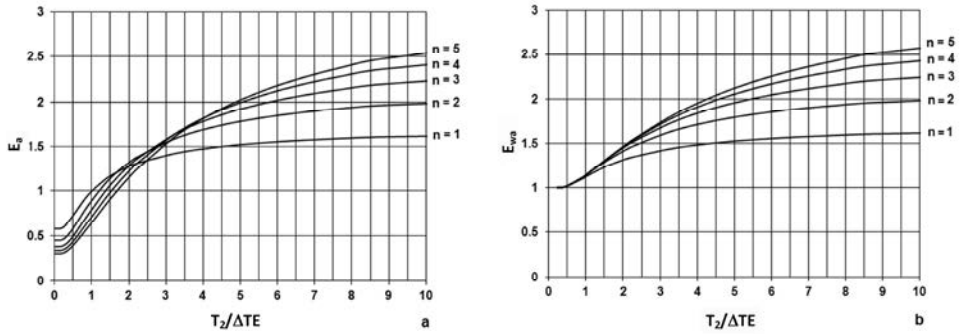

Figure 3.2. Expected SNR enhancement of a metabolic resonance by acquiring 1 FID and $n \geq 1$ symmetric echoes as a function of $T_2/\Delta TE$. (**a**) Signal averaging, Eq. [3.5]; (**b**) Weighted averaging, Eq. [3.12].

It should be noted that the enhancement models Eq. [3.5] and [3.12] assume that $T_2 >> T_2^*$. In fact, with the constraint that optimal acquisition times for the FID and the full echoes are $T_{acq}(\text{FID}) = 1.26T_2^*$ and $T_{acq}(\text{full echo}) = 2.52T_2^*$, respectively (21), one can write for $\Delta TE = 2.52T_2^*$, neglecting pulse durations and gradient durations. Or when taking into account these durations $\Delta TE = 2.52T_2^* + T_{pulse} + T_{gradient}$.

Thus far T_1 effects have been neglected. Assuming steady-state conditions, T_1 effects can be taken into account and the SNR per unit of time can be calculated for various pulse sequences. In Figure 3.3 a comparison is made of the SNR per unit of time for Ernst-angle excitation pulse acquire, 90° excitation pulse acquire, 90° excitation spin-echo acquisition (half echo), and the AMESING sequence with one FID and five full echo acquisitions for three different values of $T_2/\Delta TE$. The SNR per unit of time is given in arbitrary units and is normalised to 1.0 for Ernst-angle excitation. From the figure it appears that even for values of $T_2/\Delta TE = 1$ and $0.9 \leq T_R/T_1 \leq 1.8$ the AMESING sequence already leads to higher SNR per unit of time than low-flip Ernst-angle excitation. In situations where $T_2/\Delta TE > 1$ this range of T_R/T_1, where the SNR per unit of time for the AMESING sequence is higher than for low flip Ernst-angle excitation, becomes broader.

Published T_2 values for ^{31}P metabolites at 7 tesla by Bogner *et al.* (23) in calf muscle range from 29 ms for γ-ATP to 314 ms for phosphodiesters. Using these T_2 values and $\Delta TE = 45$ ms, $0.64 \leq T_2/\Delta TE \leq 6.98$, we expect SNR enhancements ranging between 1.0 and 2.3 for ATP and phosphodiesters, respectively, when acquiring one FID and five symmetric echoes as compared to the acquired FID of the sequence.

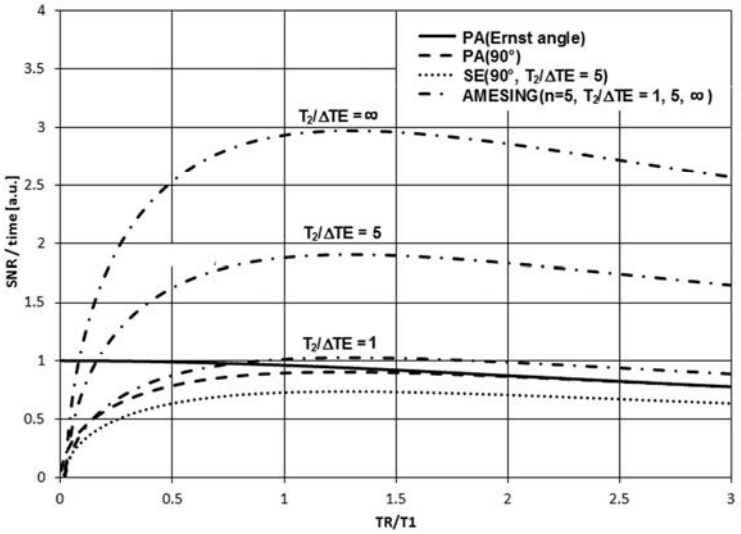

Figure 3.3. Comparison of SNR per unit of time for different pulse sequences: pulse acquire at 90 degree excitation PA(90°), at Ernst-angle excitation PA(Ernst angle), spin echo SE(90° $T_2/\Delta TE = 5$), AMESING at different ratios of T_2 over ΔTE AMESING (n = 5, $T_2/\Delta TE = 1, 5, \infty$).

Signal quantification of weighted average spectra can be done using equation [3.12]. For each individual metabolite the weighted average spectrum can be multiplied by the reciprocal value of equation [3.12], with the known fitted T_2, leading to the signal at $t = 0$ for that metabolite. Alternatively, one can directly scale the weighted average spectrum with the intensity at $t = 0$ obtained from the T_2-fit per metabolite. Quantification, or calculating intensity ratios is then identical to quantification of a FID acquisition. This still gives the advantage of the SNR increase, but it applies a scaling factor as a function of T_2 that differs per metabolite.

3.3 Experimental

The AMESING sequence was implemented on a whole body 7 tesla MR system (Philips, Cleveland, USA). Both AHP excitation and BIR-4 refocusing pulses had a frequency sweep of 10.0 kHz and tangent frequency modulation and hyperbolic tangent amplitude modulation as described in Garwood and Ke (24). The AHP excitation pulse was driven with γB_{1max} = 1400 Hz power and had a duration of 2.0 ms and a > 95% excitation band–

width of 800 Hz. The BIR-4 180° was driven with a power of γB_{1max} = 1700 Hz and had a duration 8.0 ms and a > 95% refocused component bandwidth of 1100 Hz.

The relatively long T_2 and T_1 of the ^{31}P metabolites of interest are not expected to influence the performance of the adiabatic refocusing pulses (*i.e.* pulse-duration << T_2, T_1). During the adiabatic RF pulses, the spins are locked, therefore unaffected by T_2*, and the bandwidth is an order of magnitude larger than the line broadening of the resonances.

The RF power deposition stayed within SAR guideline as determined by experimentally validated numerical simulations (16,25,26) while applying one AHP and five BIR-4 180° pulses in a T_R of 6 s. Since a surface coil was used at 7T, the SAR is determined by the local (hot spot) SAR. The effective B_1 in the center of the breast before the local SAR value exceeds 20 W/kg (excluding a safety margin) is 8 μT, which is less than the square root integral of the B_1 during the AMESING sequence. When using AHP excitation, the optimal T_R, with respect to SNR per unit of time, is 1.26T_1 of the metabolites under investigation. The *in vivo* T_1 for the PMEs and PDEs in calf muscle at 7 tesla range from 3 to 6 seconds (23), while for the PMEs in the breast at 7 tesla values of 4.7 to 5.6 s have been reported (22).

Individual resonances of PC and PE and GPC and GPE can be spectrally resolved (0.5 ppm) under favourable B_0 shimming conditions at 7 tesla. Considering the enhanced chemical shift dispersion at the higher field strength, an acquisition time of 16 ms (for a FID) provides sufficient spectral resolution (1/16 ms / 120MHz = 0.5 ppm) to enable distinction between (G)PC and (G)PE resonances. Combined with the restraints of refocusing pulse durations, spoiler gradients and phase encoding gradients, the optimum echo interval (ΔTE) that can be used in the AMESING sequence can go down to 45 ms for application in the human breast and calf muscle.

The sequence was validated in the calf muscle of a healthy male volunteer and the breast of a healthy female volunteer, using 3D MRSI spherical k-space sampling with an 8x8x8 matrix, voxels of 20x20x20 mm^3, T_R = 6 s, ΔTE = 45 ms, acquiring 1 FID and 5 echoes per T_R with a total scan time of 25 minutes per volunteer. The calf muscle spectra were acquired with a dedicated 7.0 T double tuned ^{1}H Quad / ^{31}P Quad partial volume coil (Philips, Cleveland, USA). The breast spectra were acquired using a homebuilt, unilateral sensitivity optimised, dual tuned coil setup (16).

After validation, the AMESING sequence was applied in a 50 year old female patient with breast cancer (histopathology: ductulolobular carcinoma of less than 2 ml). Here also,

1 FID and 5 echoes were acquired with T_R = 6 s, ΔTE = 45 ms in a scan time of 25 minutes, using a 8x8x8 matrix with voxels of 20x20x20 mm^3. Both FID and symmetric echoes were acquired with 256 data points, while the spectral bandwidth for the acquisition of the FID was 16.4 kHz and for the echoes 8.2 kHz to maintain equal acquisition durations for the FID and each half echo. In the case of the calf muscle, that can be B_0-shimmed adequately, the spectral resolution can be higher, however we use these settings for validation and illustration of the sequence in bad shim situations, comparable to the breast.

The acquired data was spatially Hamming filtered (effective voxel size 39 ml) and apodized in time domain using a Gaussian filter (calf muscle 12 Hz, volunteer glandular tissue 10 Hz, pectoralis muscle 8 Hz, breast cancer patient 3 Hz). The FID was zerofilled to 1024 data points and the echoes to 512 data points in the time domain to assure equal spectral resolution. The echo spectra were zeroth-order phased by matching the maximum signal of its real spectrum to its absolute spectrum. The zeroth-order phase of the FID is set to the phase of the even echoes. Therefore all spectra were zeroth-order phased before the weighted addition. The FID was also first-order corrected for the acquisition delay, and the baseline of the FID was corrected by means of fitting a second-order spline. SNR-weighted averaged spectra for the different ^{31}P metabolites of the calf muscle were calculated. The weighted average was calculated according to equation [3.6] where the weights were estimated as the SNR of the peak of interest. The noise for FID, echoes, and weighted averaged spectra was calculated as the root mean squared standard deviation of the first and last 112 data points of the zerofilled spectra, way beyond metabolite resonances. SNR was calculated as the ratio of peak height and the standard deviation of the noise. The transmitter offset for ^{31}P was at 2.8 ppm compared to PCr in the measurements of the volunteers and at 4.9 ppm in the case of the breast cancer patient, *i.e.* in between the PDE and PME resonances. Additionally, the signal intensity for all detected ^{31}P metabolites was calculated from the echoes and from the FID signal, for a voxel in the calf muscle and a voxel with breast glandular tissue. The intensity data were mono-exponentially fitted as a function of *TE*, using Poisson weighting, to calculate T_2 values for the various ^{31}P metabolites. In case of γ-ATP, J-modulation that possibly leads to too short T_2 values (27), was not taken into account, therefore reported as apparent T_2. For the breast cancer example T_2-weighted spectra for PE, PC, GPE and GPC were analyzed with the JMRUI software package (28), using AMARES (29) for spectral fitting. The calculated peak integrals for the different metabolites were normalized with the enhancement factor Eq.

[3.12], based on the measured T_2 values of the metabolites and PE/GPE, PC/GPC and PME/PDE ratios were calculated. This quantification method was first tested on a high-SNR phantom. Calculated metabolite ratios obtained from the SNR-enhanced spectra of the phantom, corrected for T_2 values, where within 4% of the metabolite ratios obtained from the high-SNR FID signal.

3.4 Results

Figure 3.4a-e show the FID and the SNR-weighted averaged ^{31}P MR spectra acquired from a voxel of calf muscle. Although the calf muscle can be shimmed adequately, in this case a bad shim was simulated using the 16 ms acquisition time for the FID and appropriate time domain apodization to smooth the truncated FID. Figure 3.4a and 3.4c both depict the FID spectrum, only the scale is different. The increase in SNR for phosphocreatine (PCr) is a factor 2.2 by using PCr weighting (Figure 3.4b). For PDE with the longest T_2, a factor 2.6 is gained in SNR (Figure 3.4d). The SNR enhancement for inorganic phosphate (Pi), using Pi-weighting, is 1.5 (Figure 3.4e). The γ-ATP SNR-weighted average spectrum depicted in Figure 3.4f has an SNR that is similar to the SNR of the γ-ATP FID spectrum, that was acquired as the first shot of the sequence, because of the very short T_2 of γ-ATP. All the weighted average spectra are scaled to the same noise level as the corresponding FID spectra.

Signal decay as a function of the number of echo times are shown in Figure 3.5a-d for γ-ATP, PCr, PDE, and Pi respectively, in a voxel of calf muscle. The T_2 values for γ-ATP, PCr, PDE, and Pi, for the calf muscle data depicted in Figure 3.5a-d are 25 ± 6 ms, 193 ± 5 ms, 375 ± 44 ms, and 96 ± 10 ms, respectively.

Breast data of a healthy volunteer and a breast cancer patient are shown in Figure 3.6 and 3.7, respectively. Figure 3.6 shows the data acquired for a Hamming filtered voxel with the pectoral muscle and a Hamming filtered voxel with glandular tissue. The SNR gain with the SNR-weighted sequence for PCr in the pectoral muscle is a factor 1.5, and for Pi in the glandular tissue voxel a factor 1.7. Despite the low intensity of the metabolic signals in glandular tissue, we were still able to fit a T_2 (136 ± 15 ms) for Pi as depicted in Figure 3.6b3. Even PDE, PME and γ-ATP can be clearly distinguished in the Pi-SNR-weighted sum spectrum of Figure 3.6b2.

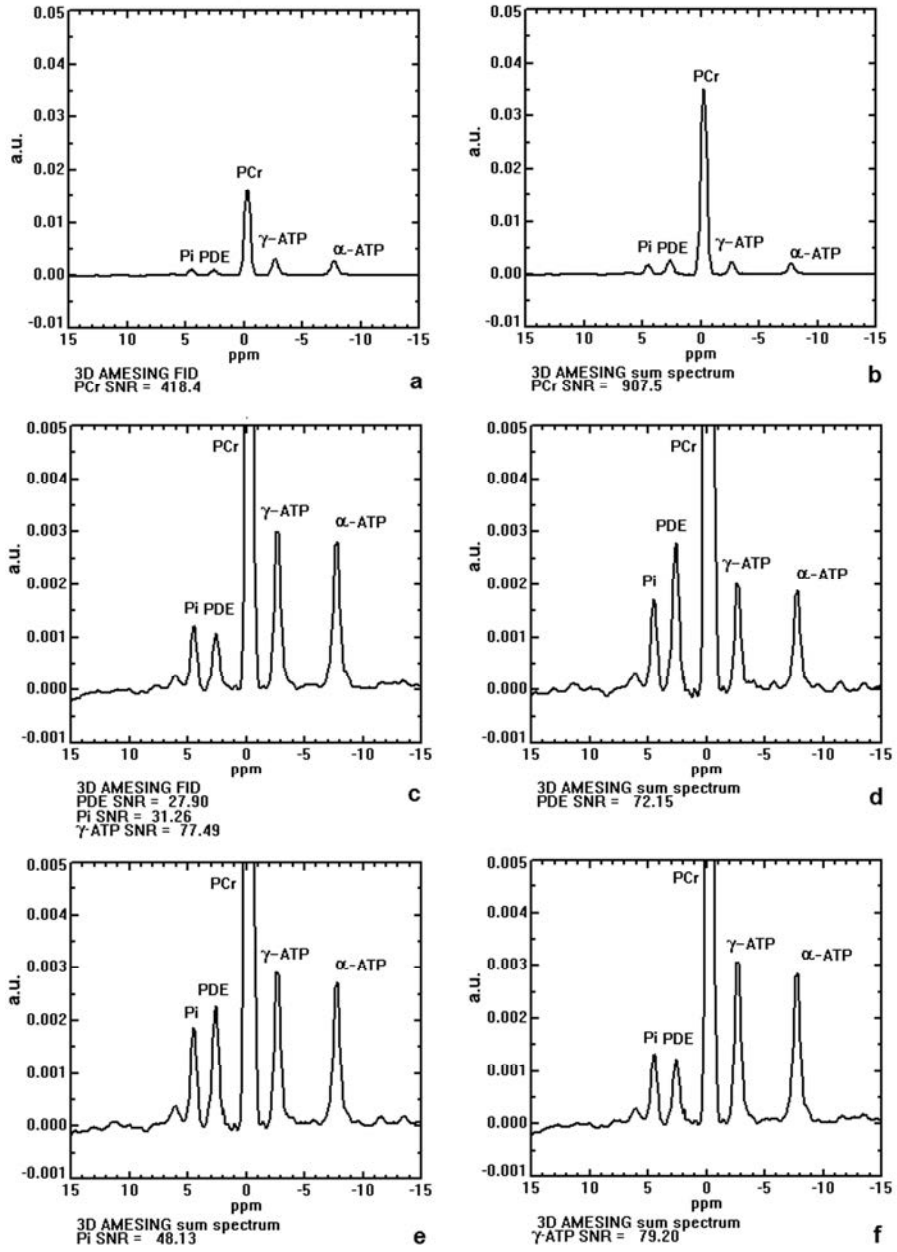

Figure 3.4a-e. FID ^{31}P MR spectra (**a**, **c**) and corresponding SNR-weighted average spectra (**b**) PCr-SNR-weighted; (**d**) PDE-SNR-weighted; (**e**) Pi-SNR-weighted; (**f**) γ-ATP-SNR-weighted, for a voxel in calf muscle. Weighted average spectra are scaled to the same noise level as the corresponding FID spectra.

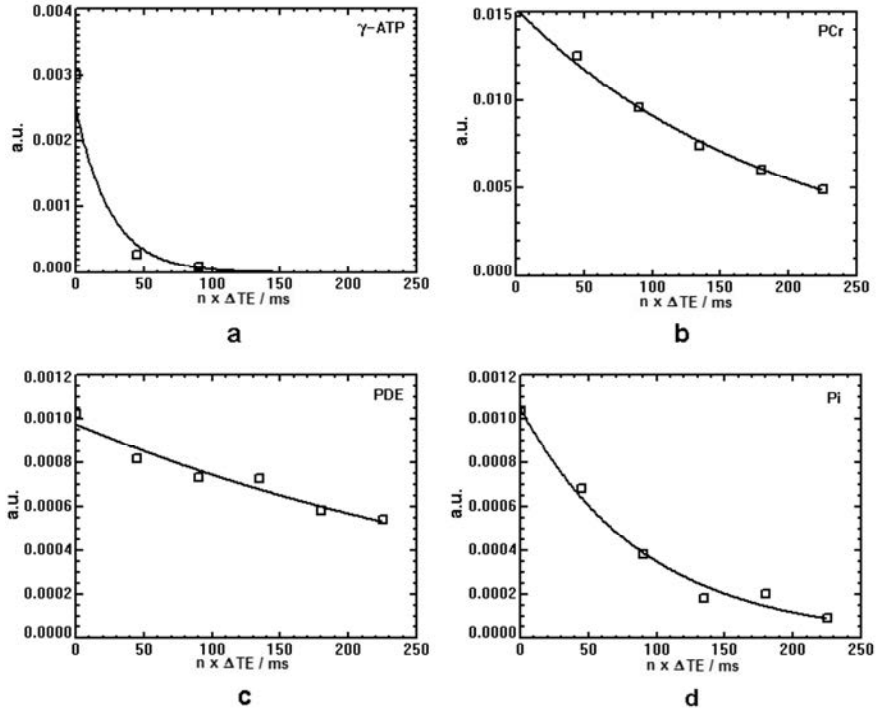

Figure 3.5. ^{31}P MR Signal intensity as a function of the number of echo times for (**a**) γ-ATP, T_2 = 25 ± 6 ms; (**b**) PCr, T_2 = 193 ± 5 ms; (**c**) PDE, T_2 = 375 ± 44 ms; (**d**) Pi, T_2 = 96 ± 10 ms, respectively, in a voxel of the calf muscle of a healthy male volunteer.

Figure 3.7a shows a Fat suppressed MR image of the left breast of a breast cancer patient. Encircled are a Hamming filtered voxel with the relatively small cancerous lesion (upper voxel) and a voxel of healthy breast tissue (lower voxel). Figure 3.7b and 3.7c show the ^{31}P FID and the PME-SNR-weighted spectra, respectively, of the cancerous lesion and d and e of the voxel with healthy tissue. The SNR gain for PE, when using the SNR-weighted echo sequence, is a factor of two as compared to the FID of the sequence. T_2 values of the phosphomonoesters and diesters fitted to the experimental data, range between 170 and 210 ms. As an example the T_2 fit for PE is shown in Figure 3.7f. The fitted PE/GPE, PC/GPC and PME/PDE ratios that are corrected for T_2 effects are 2.7, 1.8, and 2.3, respectively.

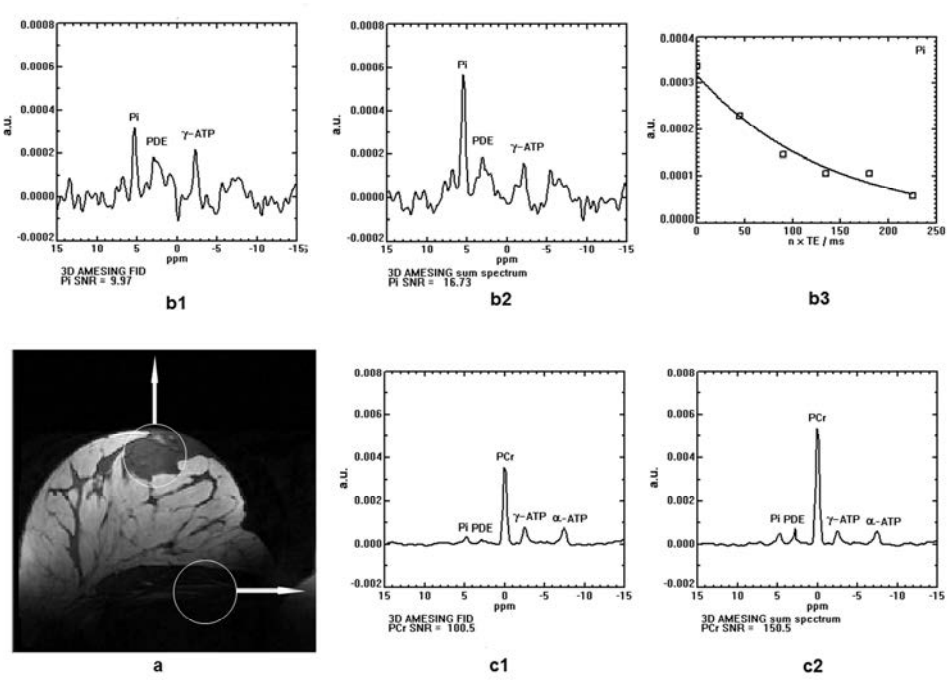

Figure 3.6. (**a**) Water suppressed breast MR image of a healthy volunteer, with encircled a voxel of pectoral muscle and a voxel of glandular tissue; (**b1**) FID ^{31}P MR spectrum of glandular tissue; (**b2**) Pi-SNR-weighted ^{31}P MR spectrum of glandular tissue; (**b3**) T_2 plot for Pi in glandular tissue, T_2 = 136 ± 15 ms; (**c1**) FID ^{31}P MR spectrum of pectoral muscle; (**c2**) PCr-SNR-weighted ^{31}P MR spectrum of pectoral muscle.

3.5 Discussion

Intrinsic sensitivity of ^{31}P MRS improves at higher magnetic fields, providing a tool to detect phosphor containing metabolites that cannot be distinguished with ^{1}H MRS. Even in areas where susceptibility differences are high, spectral resolution in ^{31}P MRS may be sufficient to detect the metabolites of interest, albeit at compromised sensitivity. Although in cases where T_2* << T_2, higher fields will not help to improve spectral resolution significantly, apart from J-coupling effects on the line width, here we demonstrate that sensitivity can be regained in these bad shim situations when using multi-echo acquisitions. Provided that T_R doesn't need to be prolonged to > 1.26T_1 due to SAR deposition, T_2 >> ΔTE, T_2* << T_2, and signals are T_2-weighted averaged, the use of more echoes will lead to more SNR as shown in Figure 3.2b. In fact, as the chemical shift dispersion increases and line widths become heavily weighted by magnetic field distortions or T_2* at higher fields, the use of

multi-echo approaches in MRS becomes more and more appealing. In order for MRS to be applied robustly in clinical studies, one needs to face this fact of short T_2*.

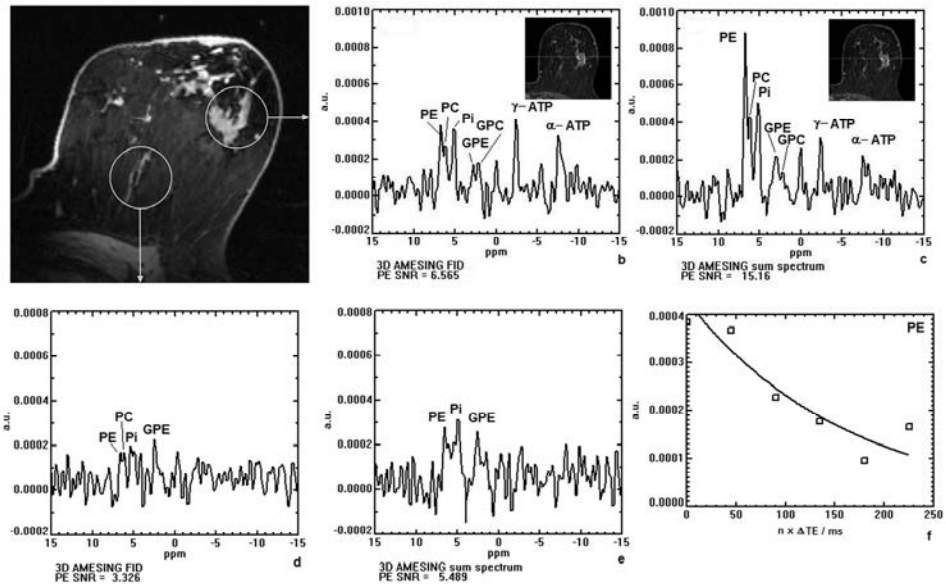

Figure 3.7. (**a**) Fat suppressed FFE MR image of the left breast of a breast cancer patient showing a voxel containing tumor tissue and a voxel containing healthy tissue; (**b**) FID ^{31}P MR spectrum and (**c**) weighted average ^{31}P MR spectrum of the voxel containing the tumor mass; (**d**) FID ^{31}P MR spectrum and (**e**) weighted average ^{31}P MR spectrum of the voxel containing healthy tissue; (**f**) T_2-fit from the voxel containing the tumor mass for PE. Fitted values of T_2 for monoesters and diesters ranged between 170 and 210 ms.

With the AMESING sequence, even in the presence of short T_2*, SNR can be optimized, or at least not degraded as would have been the case for pulse-acquire MRSI. Even with Ernst-angle excitation, pulse-acquire MRSI could only improve SNR by 11%. Consequently, ^{31}P MRSI can be a robust method for obtaining relevant metabolites with substantially less sensitivity to T_2* effects. While demonstrating its performance in the breast it may very well also be applied to other challenging but relevant targets like for instance lymph nodes.

A downside of the increased chemical shift dispersion at 7 T is that the bandwidth of RF pulses needs to increase to cover the entire spectral range. Limitations in peak power and SAR prevent the use of high bandwidth pulses, therefore the outer resonance of β-ATP at -16.3 ppm cannot be shown in the ^{31}P MR spectra. Nonetheless, the metabolites that benefit

most from the AMESING sequence, *i.e.* metabolites that have long T_2 values, have a range of chemical shifts that can easily be excited and refocused with the limited RF peak power available at 7 T.

The ^{31}P T_2 values of γ-ATP 25 ± 6 ms, PCr 193 ± 5 ms, PDE 375 ± 44 ms, Pi 96 ± 10 ms, that we determined in a 39 ml voxel in calf muscle (Figure 3.5 a-d) correspond well to published values of 29 ± 3 ms (ATP), 217 ± 14 ms (PCr), 314 ± 35 ms (PDE), and 109 ± 17 ms (Pi), acquired in larger volumes (112-169 ml) at 7 T by Bogner *et al.* (23). It should be noted that the calculated T_2 of γ-ATP is affected by J-modulation due to homonuclear ^{31}P coupling, leading to an apparent lower T_2. However, this effect is difficult to quantify because the coupled β-ATP spins are not well refocused, due to the limited bandwidth of the refocusing pulse.

The SNR-gain for PCr in the pectoral muscle of 1.5 (Figure 3.6c1-c2) is smaller than for calf muscle where the gain is 2.2 (Figure 3.4a1-a2). This may be due to the non-optimal geometry of the breast coil with respect to the chest wall, leading to low B_1 and only partial refocusing, presumably caused by non-adiabaticity of the RF pulses. In that case, calculated T_2 of ^{31}P metabolites based on these data would lead to underestimated values. The SNR gain for Pi in healthy glandular breast tissue, which is inside the optimal volume of the RF coil, is similar to that in calf muscle.

The essence of using the AMESING sequence at 7 tesla is demonstrated in a breast cancer patient. In a tumor (T2-staged breast cancer) with a size less than 2 ml, elevated resonances of PMEs could be observed. As the tumor is surrounded by lipid tissue, where PME signals are not detectable, the sensitivity of ^{31}P MRS with AMESING at 7 tesla seems to enable the detection of phospholipid metabolites from tumors of only 2 ml. Note that the encircled voxels in Figure 3.6 and 3.7 are spatially Hamming filtered voxels, that reduce voxel bleeding to a minimum while being 1.7 times as large as the nominal voxel size. Metabolite ratios for PMEs to PDEs obtained from the SNR-enhanced spectra corrected for T_2 effects are, as expected, larger than 1, in this case of ductulolobular carcinoma. It should be noted here, however, that quantifications based on this method are dependent on the reliability of the fitted T_2 values.

While this study demonstrated applicability of the AMESING sequence for 3D encoding, it may also apply to slice, bar or voxel selective 2D MRS, 1D MRS or unlocalized MRS. In addition, acquisition weighting can be applied which will increase SNR even more, although it is not compatible with T_2 measurement and will lead to

broadening of the spatial response function as different k-steps will have different intensities.

3.6 Conclusions

3D AMESING at 7 tesla is a promising tool for ^{31}P MR spectroscopy in regaining SNR in bad shim situations, in providing localised T_2 measurement of metabolites, and thereby retaining the possibility of quantification.

Here we validated its application in calf muscle and in glandular breast tissue of a healthy female volunteer, and applied the sequence in cancerous tissue in a breast cancer patient. We were able to fit T_2 values for several ^{31}P metabolites in voxel volumes as small as 39 ml. Our T_2 data for phosphorus metabolites in calf muscle agrees well with previously published data, which was acquired in 3 to 4 times larger sample volumes.

T_2-weighted averaging could be applied for each metabolite separately, resulting in different gains in SNR compared to the FID spectra acquired in the first shot of the sequence of up to 2.6-fold for PDEs measured in calf muscle and almost a factor 2 for PMEs in ductulolobular breast carcinoma. Therefore, using the AMESING sequence at 7 tesla, we were able to detect phospholipid metabolites *in vivo* and determined their ratios in a ductulolobular carcinoma of less than 2 ml.

References

1. Negendank W. Studies of human tumors by MRS: a review. NMR Biomed. 1992; 5: 303–324.
2. Podo F. Tumour phospholipid metabolism. NMR Biomed. 1999; 12: 413–439.
3. Aboagye EO, Bhujwalla ZM. Malignant transformation alters membrane choline phospholipid metabolism of human mammary epithelial cells. Cancer Res. 1999; 59: 80–84.
4. Glunde K, Jie C, Bhujwalla ZM. Molecular causes of the aberrant choline phospholipid metabolism in breast cancer. Cancer Res. 2004; 64: 4270–4276.
5. Glunde K, Bhujwalla ZM, Ronen SM. Choline metabolism in malignant transformation. Nat. Rev. Cancer 2011; 11: 835-48.
6. Graaf RA de. *In Vivo* NMR, principals and techniques. Chichester: Wiley; 2007.
7. Burum DP, Ernst RR. Net polarization transfer via a J-ordered state for signal enhancement of low-sensitivity nuclei. J. Magn. Reson. 1980; 39: 163–168.

8. Payne GS and Leach MO. Surface-coil polarization transfer for monitoring tissue metabolism *in vivo*. Magn. Reson. Med. 2000; 43: 510–516.

9. Kemp WJM van der, Boer VO, Luijten PR, Wijnen JP, Klomp DWJ. Increase in SNR for ^{31}P MR spectroscopy by combining polarization transfer with a direct detection sequence. Magn. Reson. Med. 2012; 68: 353-357.

10. Burt CT, Cohen SM, Barany M. Analysis of intact tissue with ^{31}P NMR. Ann. Rev. Biophys. Bioeng. 1979; 8: 1-25.

11. Bachert-Baumann P, Ermark F, Zabel HJ, Sauter R, Semmler W, Lorenz WJ. *In vivo* nuclear Overhauser effect in ^{31}P-(^{1}H) double-resonance experiments in a 1.5-T whole-body MR system. Magn. Reson. Med. 1990; 15: 165-172.

12. Sluis R van, Payne GS, Leach MO. Increased NOE enhancement in ^{1}H decoupled ^{31}P MRS. Magn. Reson. Med. 1995; 34: 893–897.

13. Emir UE, Auerbach EJ, Moortele PF van de, Marjańska M, Uğurbil K, Terpstra M, Tkáč I, Oz G. Regional neurochemical profiles in the human brain measured by ^{1}H MRS at 7 T using local B_1 shimming. NMR Biomed. 2012; 25: 152-160.

14. Kobus T, Bitz AK, Uden MJ van, Lagemaat MW, Rothgang E, Orzada S, Heerschap A, Scheenen TW. *In Vivo* ^{31}P MR spectroscopic imaging of the human prostate at 7 T: Safety and feasibility. Magn. Reson. Med. 2012; 68: 1683-1695.

15. Leach MO, Verrill M, Glaholm J, Smith TA, Collins DJ, Payne GS, Sharp JC, Ronen SM, McCready VR, Powles TJ, Smith IE. Measurements of human breast cancer using magnetic resonance spectroscopy: a review of clinical measurements and a report of localized ^{31}P measurements of response to treatment. NMR Biomed. 1998; 11: 314-340.

16. Klomp DWJ, Bank BL van de, Raaijmakers A, Korteweg MA, Possanzini C, Boer VO, Berg CAT van de, Bosch MAAJ van de, Luijten PR. ^{31}P MRSI and ^{1}H MRS at 7 T: initial results in human breast cancer. NMR Biomed. 2011; 24: 1337–1342.

17. Boer VO, Bank BL van de, Vliet G van, Luijten PR, Klomp DW. Direct B_0 field monitoring and real-time B_0 field updating in the human breast at 7 tesla. Magn. Reson. Med. 2012; 67: 586-591.

18. Mulkern RV, Meng J, Oshio K, Guttmann CRG, Jaramillo ND, Bone marrow characterization in the lumbar spine with inner-volume spectroscopic CPMG imaging studies. J. Magn. Reson. Imaging 1994; 4: 585-589.

19. Dreher W, and Leibfritz, D. Parametric multi-echo proton spectroscopic imaging: Application to the rat brain *in vivo*. Magn. Reson. Imaging 1995; 13: 753-761.

20. Mulkern RV, Meng J, Oshio K, Tzika AA. Line scan imaging of brain metabolites with CPMG sequences at 1.5 T. J. Magn. Reson. Imaging 1996; 6: 399-405.

21. Pohmann R, Kienlin M von, Haase A, Theoretical evaluation and comparison of fast chemical shift imaging methods. J. Magn. Reson. 1997; 129: 145–160.

22. Wijnen JP, Kemp WJM van der, Luttje MP, Korteweg MA, Luijten PR, Klomp DWJ. Quantitative ^{31}P magnetic resonance spectroscopy of the human breast at 7 T. Magn. Reson. Med. 2012; 68: 339-348.

23. Bogner W, Chmelik M, Schmid AI, Moser E, Trattnig S, Gruber S. Assessment of ^{31}P relaxation times in the human calf muscle: a comparison between 3 T and 7 T *in vivo.* Magn. Reson. Med. 2009; 62: 574-582.

24. Garwood M and Ke Y. Symmetric pulses to induce arbitrary flip angles with compensation for RF inhomogeneity and resonance offsets. J. Magn. Reson. 1991; 94: 511-525.

25. International Electrotechnical Commission (IEC). IEC 60601-2-33. Medical electrical equipment. Part 2-33: Particular requirements for the safety of magnetic resonance equipment for medical diagnosis. IEC 60601-2-33 Ed. 3: 2010. Geneva: IEC; 2010.

26. Klomp DWJ, Raaijmakers AJE, Korteweg MA, Bank BL van de, Possanzini C, Boer VO, Visser F, Berg CAT van de, Luijten PR. High-resolution MR imaging and spectroscopy of the human breast at 7T using a focused field RF coil setup. Proc. Intl. Soc. Mag. Reson. Med. 2010; 18: 2469.

27. Jung WI, Straubinger K, Bunse M, Widmaier S, Schick F, Küper K, Dietze G, Lutz O. A pitfall associated with determination of transverse relaxation times of the ^{31}P NMR signals of ATP using the Hahn spin-echo. Magn. Reson. Med. 1993; 30: 138-141.

28. Naressi A, Couturier C, Devos JM, Janssen M, Mangeat C, Beer R de, Graveron-Demilly D. 'Java-based graphical user interface for the MRUI quantitation package'. MAGMA, 2001; 12: 141-152.

29. Vanhamme L, Boogaart A van den, Huffel S van. Improved method for accurate and efficient quantification of MRS data with use of prior knowledge . J. Magn. Reson. 1997; 129: 35-43.

CHAPTER 4

Phosphorus Magnetic Resonance Spectroscopy of the breast and the influence of the menstrual cycle

BL Stehouwer, WJM van der Kemp, PR Luijten, MAAJ van den Bosch,
WB Veldhuis, JP Wijnen, DWJ Klomp.
Breast Cancer Research and Treatment 2014; 144: 583-589.

4.1 Introduction

Breast cancer is the most common malignancy in women worldwide (1). Radiological imaging is essential in the patients work-up to establish a diagnosis and to determine a treatment plan. Dynamic contrast-enhanced (DCE) MRI is regularly used in the evaluation of breast lesions as well as for the monitoring of patients who receive neoadjuvant chemotherapy (2,3). Although DCE breast MRI has a high sensitivity for the detection of breast lesions, the specificity is relatively low; approximately 70% (4). The same accounts for the effectiveness of DCE MRI in treatment monitoring, which has shown to be variable depending on receptor status of the tumor (5). Therefore, other techniques are investigated to improve specificity.

One of the techniques of interest is MR Spectroscopy (MRS) or MR Spectroscopic Imaging (MRSI). With MRS(I) metabolites can be measured non-invasively. To date, patient studies mainly focused on proton (^{1}H) MRS (6). With ^{1}H MRS levels of the total pool of choline and ethanolamine containing compounds resonating at 3.2 ppm (tCho) are measured to evaluate the presence of malignancy and its response to therapy (6-8). However, tCho contains multiple different metabolites that individually play a role in the tumor metabolism (9). With phosphorus (^{31}P) MRS the phosphomonoesters (PME): phosphocholine (PC) and phosphoethanolamine (PE), as well as the phosphodiesters (PDE): glycerophosphocholine (GPC) and glycerophosphoethanolamine (GPE), can be measured individually, which was shown for the first time in breast cancer patients in 1988 (10). Elevated PME to PDE levels have been associated with the presence of cancer, while a fall in PME to PDE levels is seen in case of effective therapy (11). Other *ex vivo* work

described a lower PC to GPC ratio to be indicative of more aggressive breast cancer subtypes, such as triple negative breast cancer (12). Since phosphorus is less abundant than protons in the human body, and the gyromagnetic constant of ^{31}P is a factor 2.5 lower than that of ^{1}H, the measurements are challenging due to a lack of signal-to-noise ratio (SNR). However, recent studies have shown that ^{31}P MRS(I) at 7.0 tesla (7 T) is feasible for *in vivo* detection and quantification of phosphorus metabolites (13,14) with acceptable acquisition times and sufficient spatial resolution, particularly when using multi-echo acquisitions (15).

It is well known that, due to hormonal fluctuations, breast tissue changes during the menstrual cycle (16,17). Research has been performed to evaluate in which phase of the menstrual cycle DCE MRI should preferably be performed to avoid false positive readings due to contrast-agent uptake in normal glandular tissue (18-21). However, there is only little data on normal values of phosphorus metabolites and their fluctuation during all phases of the menstrual cycle measured with ^{31}P MRS. Consequently, it is unclear whether it can be combined with DCE MRI in clinical practice at the optimal timing for both methods. Of the published data, one study, performed in four premenopausal women at a compromised SNR at 1.5 T, does suggest that the PME, PDE and total ^{31}P signals change during the menstrual cycle (22). A second study, including five premenopausal women who were not taking oral contraceptives, scanned at 1.5 T as well, found a significant lower PME relative peak area in second week of the menstrual cycle as well as a significant higher PDE/PME peak area ratio (23).

Knowledge of normal values, and their fluctuation during the menstrual cycle, offers a framework for the interpretation of breast cancer patient data. Therefore, in this study, we investigated the phospholipid metabolism in glandular breast tissue and the influence of the menstrual cycle on the metabolism with ^{31}P MRS at 7 T.

4.2 Methods

4.2.1 Subjects and data acquisition

Seven female volunteers, who had a regular menstrual cycle and did not use any hormonal contraceptives, were included. The mean age was 27 years (range 24-30 years). Each volunteer underwent four 7 T MRSI examinations, one in each phase of the menstrual

cycle: the early follicular phase (EF), late follicular phase (LF), early luteal phase (EL), and late luteal phase (LL), resulting in 28 examinations in total. Before each examination the menstrual cycle status was reported and informed consent was signed. All examinations were performed in compliance with the local institutional ethics committee.

The examinations were performed on a 7 T whole-body scanner (Philips Healthcare, Cleveland, USA) using a two-channel double-tuned unilateral RF breast coil (MR Coils BV, Drunen, the Netherlands), with the resonance frequencies of 298 and 121 MHz for ^{1}H and ^{31}P, respectively (13,24). All volunteers were scanned in prone position with the coil encompassing the right breast. The scan protocol consisted of a 3D T_{1w} sequence [T_R/*TE* 4.0/2.0 ms, binominal flip angle 5°, FOV 160x160x160 mm^3, acquired resolution 1x1x2 mm^3], and a 3D ^{31}P multi-echo MRSI sequence, using spherical k-space sampling and an excitation bandwidth of 800 Hz [T_R/*TE* 6000/45 ms, adiabatic flip angle 90°, FOV 320x160x320 mm^3, nominal spatial resolution 40x20x40 mm^3]. One free induction decay (FID) and 5 full echoes were acquired within one T_R, resulting in the five echoes at 45, 90, 135, 180 and 225 ms, respectively. Both the FID and echoes were acquired with 256 data points. The MRS sequence is described in more detail elsewhere (15). Total scanning time was approximately 30 minutes.

4.2.2 Data analysis

The spectroscopy data was analyzed using IDL (Research Systems, Boulder, CO) and JMRUI 4.0 software (25). Acquired data was Hamming filtered in the spatial domain and zero-filled to 8192 data points in the time domain. The Hamming filtering resulted in voxels with an elliptical full-width half-max of 68x34x68 mm^3. One localized voxel from the MRSI examination containing glandular tissue, represented by high inorganic phosphate (Pi) and low phosphocreatine (PCr) signal, was chosen to use in the analyses. For each volunteer's examination the optimal voxel was chosen, which could be the same or a different voxel at each of the four time-points. All spectra, *i.e.* FIDs and echoes, were frequency aligned to Pi. Subsequent, all spectra were summed for the FID and each of the five echoes separately within JMRUI, weighted by the Pi signal for the FID. Metabolite quantification for PC, PE, GPE and GPC was done in JMRUI using the AMARES algorithm on the summed spectra (26). Prior to metabolite quantification, the average value of chemical shifts of all metabolites in each sum spectrum (1 sum total FID and 5 sum total

echo spectra) were determined. Furthermore, the sum spectra were apodized with 40 Hz, representing the smallest line width found. During quantification the line widths of PE, PC, GPE, GPC were set equal in each sum spectrum. The line widths determined for PMEs and PDEs of the different sum spectra ranged between 56 - 67 Hz, for Pi the linewidth ranged between 45 - 55 Hz for the different sum spectra. The difference in range corresponds to peak broadening for PME and PDE caused by ^{1}H-^{31}P J-coupling. The chemical shift values used in the quantification were constrained to the average chemical shift values (over the 4 cycle points) with a soft constraint of ± 0.05 ppm. Overall phases were fixed to zero in the quantification.

The peak integrals for PE, PC, GPE and GPC, obtained in the sum spectrum of all FIDs and in the sum spectrum of each echo, were used to calculate metabolite T_2 values. Standard deviations of the T_2 values were determined using Monte Carlo simulations, representing the uncertainty of the fittings. Metabolite signal ratios were determined based on the spectrum of the FID plus 5 echoes combined. The combining was performed accounting for the T_2 relaxations times of the metabolites, where the full echoes were weighted two times in comparison to the FID. This resulted in a sum spectrum per metabolite which was used for quantification. The metabolite quantification was done on group level and for each volunteer separately. Standard deviations of the metabolite ratios were determined using Monte Carlo simulations, representing the measurements uncertainty. All three metabolic ratios were tested for significant variation over the menstrual cycle on the individual data using Friedman's two-way ANOVA test.

4.3 Results

All 28 examinations were conducted successfully. In the analysis first a voxel containing glandular tissue was chosen for each measurement. One example is presented in Figure 4.1. A large proportion of the selected voxel in Figure 4.1 contains glandular tissue while chest wall muscle was excluded, resulting in a high Pi signal and relatively low PCr, as can be seen in the spectrum. Of all measurements one did not show sufficient signal from phosphorus resonances (SNR < 3), resulting in 27 exams to be included in the final analyses.

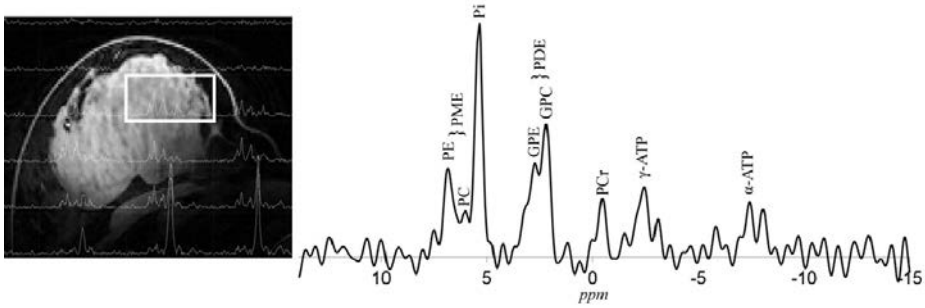

Figure 4.1. T_{1w} 3D FFE image (**a**) with a representation of the grid of voxels and their spectra. The voxel selected for the analysis is highlighted, of which the (**b**) ^{31}P FID spectrum is shown. Note the relatively high PME, Pi and PDE signals in contrast to the relatively low PCr signal.

Second, the T_2 relaxation times of the metabolites were calculated using the data of all volunteers combined for the FID and for each echo. These six pooled spectra (1 FID and 5 echoes) are shown in Figure 4.2.

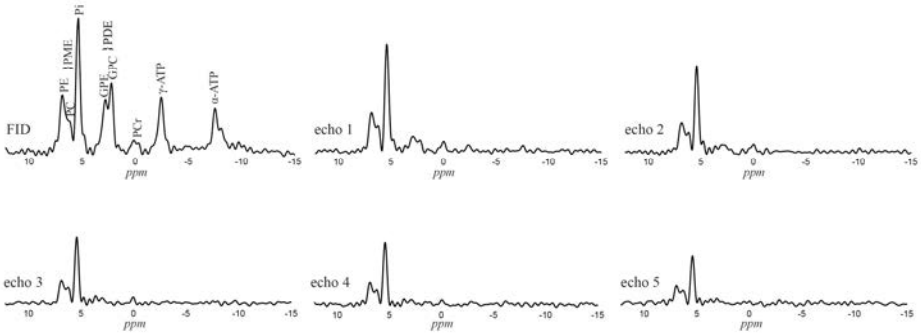

Figure 4.2. ^{31}P MR spectra of the FID and five echoes. From these spectra T_2 fits were made for PE, PC, GPE and GPC. Note the fast decay of PDEs, and slower decay of PMEs.

It can be observed that the PMEs decay much slower than the PDEs. T_2 decay plots were made for each of the metabolites, resulting in a T_2 relaxation time for PE of 154 ms (95% CI 144-164), for PC of 173 ms (95% CI 148-205), for Pi of 188 ms (95% CI 182-193), for GPE of 48 ms (95% CI 44-53), and for GPC of 23 ms (95% CI 21-26). Subsequent, the combined data of the FID and echoes were analyzed, on group basis and on individual basis, accounting for the calculated T_2 relaxation times of the metabolites (*i.e.* the FID and echoes were T_2-weighted and summed on a group level and individually).

^{31}P MR spectra, analyzed on group level, in the four phases of the menstrual cycle are displayed in Figure 4.3. The phosphorus metabolite signal ratios of these spectra analyzed on group level are presented in Table 4.I and Figure 4.4. The results for the seven volunteers individually are also displayed in Figure 4.4. In the group analysis a negligible variation in metabolic signal ratios throughout the menstrual cycle is observed, which is similar to the inaccuracy (expressed as standard deviations) of the measurement. The individually analyzed data shows more variation between the volunteers as well as between phases in the menstrual cycle within the volunteers, however, the standard deviations are larger as well. No specific pattern of variation during the menstrual cycle is observed for any of the ratios, and magnitudes of the observed variations are in the order of the experimental uncertainties (p = 0.86, p = 0.90 and p = 0.75, for PME to PDE, PE to GPE and PC to GPC, respectively).

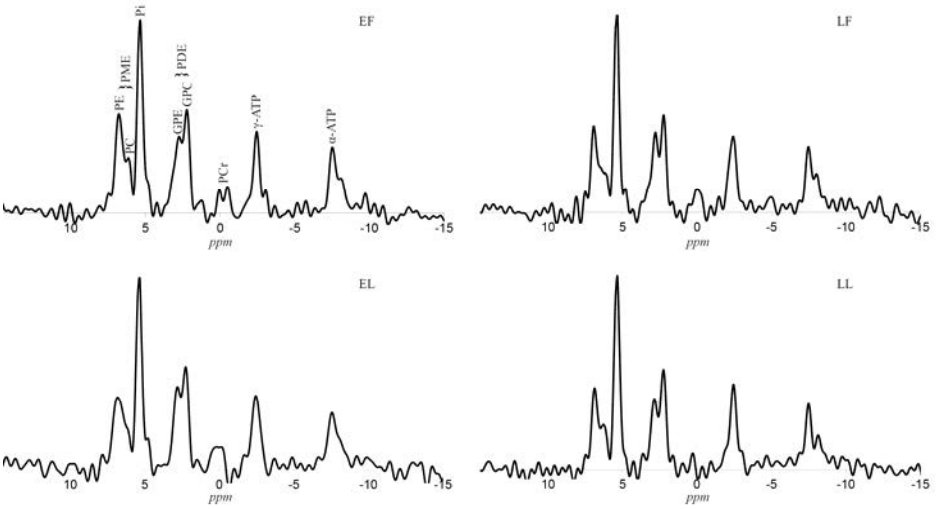

Figure 4.3. ^{31}P MR spectra analysed on group level, using the FID data, for each phase of the menstrual cycle; the early follicular phase (EF), late follicular phase (LF), early luteal phase (EL), and late luteal phase (LL).

Table 4.I. Metabolic signal ratios for the combined FID plus multi-echo data on group level, presented per phase of the menstrual cycle.

Metabolic signal ratios of FID plus multi-echo data ± SD				
	EF	LF	EL	LL
PME/PDE	0.75 ± 0.02	0.70 ± 0.02	0.69 ± 0.03	0.72 ± 0.02
PE/GPE	1.23 ± 0.08	1.13 ± 0.08	1.19 ± 0.10	1.24 ± 0.09
PC/GPC	0.40 ± 0.04	0.36 ± 0.03	0.33 ± 0.04	0.37 ± 0.03

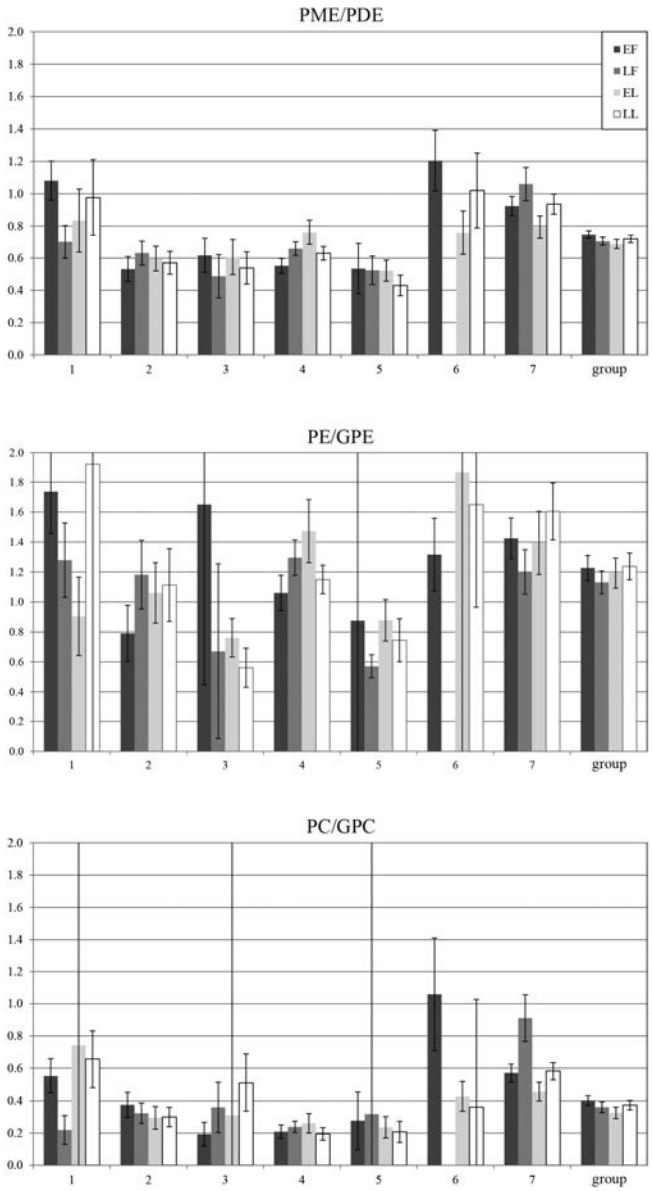

Figure 4.4. Phosphorus metabolic signal ratios for PME/PDE, PE/GPE and PC/GPC over the menstrual cycle with the standard deviation caused by system noise displayed with error bars. The ratios shown are the individual data (1 to 7) and the group data (group) obtained from the T_2-weighted analysis of the combined FID and multi-echo data. Note that the group results show little variation over the menstrual cycle for each ratio, which remain within standard deviations. On individual basis more variation is observed, however, without a specific pattern over the menstrual cycle.

4.4 Discussion

In this study no significant variations in phosphorus metabolite signal ratios over the menstrual cycle were measured on group level using ^{31}P MRS in the breast at 7 T. In the individual data analysis more variation was observed over the menstrual cycle intra-individually. However, the variation showed neither a specific pattern nor statistical significance since the measurements' uncertainty is greater than the observed variations.

In previous work, where ^{31}P MRS was similarly assessed in four premenopausal women, the summed data showed PME to PDE ratios of 1.06, 1.75, 0.48 and 0.78 for EF, LF, EL and LL, respectively (22). In our study, the summed data showed PME to PDE signal ratios of 0.75, 0.70, 0.69, and 0.72, indicating a more stable course throughout the menstrual cycle. Furthermore, the reported lower PME peak area in the late follicular phase, as measured in five women by Twelves *et al.* (23) was not reproduced, nor did we find significant lower levels of the individual monoesters PE and PC in any phase when assessing the metabolic signal ratios. In contrast to previous work, the SNR in our study was higher, which can be appreciated in the presented spectra. The higher SNR, and also higher spectral resolution provided by 7 T, allowed for assessment of the PE/GPE and PC/GPC ratio as well. Still, the measurements uncertainty, as can be observed by the standard deviations of the ratios, especially in the individual assessment, remains greater than the observed variation.

A relatively low PCr signal can be observed in the presented spectra. PCr has been reported to originate mainly from the chest wall in MRS breast spectra (15,23). When chest wall muscle is included a PCr signal a multitude greater than PME, Pi or PDE is to be expected (15). A relative low PCr signal is therefore considered a marker of good localization.

In all three metabolic ratios variations between the volunteers as well as between phases of the menstrual cycle were observed, however, also with larger standard deviations caused by relatively increased system noise when compared to the group analysis. Theoretically, an increase of PME/PDE ratio could be expected in the luteal phase. During the luteal phase progesterone levels are high, resulting in more proliferative activity, which is associated with a rise in PMEs (16,17,27). On the other hand, apoptotic figures are frequently seen during the luteal phase as well (16), possibly counteracting the effect of proliferation on the PME/PDE ratio, as cell breakdown is associated with an increase in PDEs (28).

However, the observed variation in the individual data did not show a specific pattern over the menstrual cycle.

Technical aspects may also have played a role in the inter-individual variation. For instance, differences in the distribution of glandular versus lipid tissue throughout the breast results in differences in magnetic field distortions. These lead to differences in spectral line widths, which cause a reduction in SNR and more overlap between resonances, and with that to more uncertainty in the results. Also, the reproducibility of the examinations might have played a role. There is only few data on the reproducibility of ^{31}P MRS(I) examinations in the breast. The data that is available suggests a 6% variation of total phosphate signal in patients that are examined on different days (11). The effects on metabolic ratios are not described in that work. It would be of great value to determine the reproducibility of ^{31}P MRS examinations, especially the precision. That way changes in ^{31}P MRS results obtained in longitudinal patient studies can be ascribed to either disease or therapy related changes, or to the measurements' variance.

Knowing that the menstrual cycle may influence the individuals' results in different phases of the menstrual cycle, the metabolic ratios may still be used as a follow-up marker in breast cancer patients to monitor treatment efficacy. Particularly, when using a bilateral set-up, the results of the contralateral breast may be used as an intra-individual reference measurement. In this study a unilateral breast coil was used. However, the first bilateral breast set-ups for 7 T have recently been presented (29,30), in which double-tuning could be incorporated.

Other MR spectroscopy methods that are of interest for their value in breast cancer diagnosis or monitoring have similarly evaluated the influence of the menstrual cycle on measurement results. For instance ^{1}H MRS has been used to measure the lipid composition and water-fat ratio at 1.5 and 4 T, respectively (31,32). Both showed to be significantly influenced by the menstrual cycle, implying that menstrual cycle status is important to take into account and correct for in a patient population when using these methods. In contrast, our current study shows that the used ^{31}P MRSI sequence can be applied independent of menstrual cycle status, which is favorable in a clinical setting.

T_2 relaxation times were calculated to account for when using the multi-echo data to maximize the SNR. To accurately determine the T_2 relaxation times all data were pooled over the volunteers and time points, assuming T_2 values do not changes over the menstrual cycle. In the calculations the PDEs showed to have a much shorter T_2 relaxation time than

the PMEs. That could possibly lead to misinterpretation of the multi-echo data when not compensating for this difference.

T_1 relaxation times were not accounted for in the analysis. This means the results are reproducible when using a T_R of 6 seconds, however, when using different repetition times a weighting factor has to be applied on the ratios.

For our study purpose a large voxel size was used, with a spatial resolution of 40x20x40 mm^3 (Figure 4.1), combined with Hamming filtering of the data in the spatial domain, which lead to sufficient signal in almost all cases to assess all metabolic ratios. In clinical practice however, a smaller voxel size will be mandatory and all the SNR available from a multi-echo sequence will be needed. Still, one of the volunteers' examinations did not show enough signal from the phosphorus resonances to be included in the analyses. If only a small amount of glandular tissue is present, or heterogeneously spread throughout the breast, the signals can possibly not exceed the noise level. In this one particular case, combined with a sub-optimal shim setting, it led to insufficient SNR to analyze the peak integrals. Research has shown that breast cancer has much higher PME signals than normal breast tissue, because of an increased phospholipid membrane anabolism (11). PMEs have been reported to be about three times as high in breast cancer compared to benign tumors (33,34). Therefore, in case of the presence of a malignancy it is expected that signals will sufficiently exceed noise level even if a smaller voxel size is used.

A limitation of our study is that the menstrual cycle status was assessed per questionnaire and no serum estrogen and progesterone levels were measured to verify the cycle phase. We did only include females with regular menstrual cycles to optimal determine the menstrual cycle phase without having to take a blood sample. However, this does mean that possible anovulatory cycles were not detected, which are reported to occur in up to 14% of healthy regular menstruating women (35).

Another limitation is that reported metabolite ratios are obtained in premenopausal women while the majority of breast cancer patients are postmenopausal. However, it has been shown that in the assessment of relative peak areas of PME, PDE and PCr there is only a significant difference in the PCr peak between pre-menopausal and post-menopausal women (23). This is probably due to breast size, because the observable PCr originated from the pectoral muscles (14). Those data therefore do imply that our obtained metabolic ratios apply in postmenopausal women as well.

In conclusion, phosphorus metabolic signal ratios assessed using multi-echo ^{31}P MRS examinations during the menstrual cycle do not show a variation on group level. On

individual basis more variation is observed, although without a specific pattern or statistical significance due to the uncertainty of the ^{31}P MRS measurements in individual subjects. Therefore, without significantly affecting the results of the phosphorus metabolic ratios, ^{31}P MRS examinations can be performed independent of menstrual cycle status.

References

1. Jemal A, Bray F, Center MM, Ferlay J, Ward E, Forman D. Global cancer statistics.CA Cancer J. Clin. 2011; 61: 69-90.
2. Mann RM, Kuhl CK, Kinkel K, Boetes C Breast MRI: guidelines from the European Society of Breast Imaging. Eur. Radiol. 2008; 18: 1307-1318.
3. Yeh ED. Breast magnetic resonance imaging: current clinical indications. Magn. Reson. Imag. Clin. N. Am. 2010; 18: 155–169.
4. Peters NHGM, Borel Rinkes IHM, Zuithoff NPA, Mali WPThM, Moons KGM, Peeters PHM. Meta-analysis of MR imaging in the diagnosis of breast lesions. Radiology 2008; 246: 116-124.
5. Loo CE, Straver ME, Rodenhuis S, Muller SH, Wesseling J, Vrancken Peeters MJTFD, Gilhuijs KGA. Magnetic resonance imaging response monitoring of breast cancer during neoadjuvant chemotherapy: relevance of breast cancer subtype. J. Clin. Oncol. 2011; 29: 660-666.
6. Begley JKP, Redpath TW, Bolan PJ, Gilbert FJ. *In vivo* proton magnetic resonance spectroscopy of breast cancer: a review of the literature. Breast Cancer Res. 2012; 14: 207.
7. Haddadin IS, McIntosh A, Meisamy S, Corum C, Styczynski Snyder AL, Powell NJ, Nelson MT, Yee D, Garwood M, Bolan PJ. Metabolite quantification and high field MRS in breast cancer. NMR Biomed. 2009; 22: 65-76.
8. Bolan PJ, Nelson MT, Yee D, Garwood M. Imaging in breast cancer: magnetic resonance spectroscopy. Breast Cancer Res. 2005; 7: 149-152.
9. Podo F. Tumour phospholipid metabolism. NMR Biomed. 1999; 12: 413-439.
10. Sijens PE, Wijrdeman HK, Moerland MA, Bakker CJ, Vermeulen JW, Luyten PR. Human breast cancer *in vivo*: ^{1}H and ^{31}P MR spectroscopy at 1.5 T. Radiology 1988; 169: 615-620.
11. Leach MO, Verrill M, Glaholm J, Smith TAD, Collins DJ, Payne GS, Sharp JC, Ronen SM, McCready VR, Powles TJ, Smith IE. Measurements of human breast cancer using magnetic resonance spectroscopy: a review of clinical measurements and a report of localized ^{31}P measurements of response to treatment. NMR Biomed. 1998; 11: 314-340.
12. Moestue SA, Giskeødegård GF, Cao MD, Bathen TF, Gribbestad IS. Glycerophosphocholine (GPC) is a poorly understood biomarker in breast cancer. Proc. Natl. Acad. Sci. U.S.A 2012; 109: E2506.

13. Klomp DWJ, Bank BL van de, Raaijmakers A, Korteweg MA, Possanzini C, Boer VO, Berg CA van de, Bosch MAAJ van den, Luijten PR. ^{31}P MRSI and ^{1}H MRS at 7 T: initial results in human breast cancer. NMR Biomed. 2011; 24: 1337-1342.

14. Wijnen JP, Kemp WJM van der, Luttje MP, Korteweg MA, Luijten PR, Klomp DWJ. Quantitative ^{31}P magnetic resonance spectroscopy of the human breast at 7 T. Magn. Reson. Med. 2012; 68: 339-348.

15. Kemp WJM van der, Boer VO, Luijten PR, Stehouwer BL, Veldhuis WB, Klomp DWJ. Adiabatic multi-echo ^{31}P spectroscopic imaging (AMESING) at 7 T for the measurement of transverse relaxation times and regaining of sensitivity in tissues with short T_2* values. NMR Biomed. 2013; 26: 1299-1307.

16. Ramakrishnan R, Khan SA, Badve S. Morphological changes in breast tissue with menstrual cycle. Mod. Pathol. 2002; 15: 1348-1356.

17. Vogel PM, Georgiade NG, Fetter BF, Vogel FS, McCarty KS Jr. The correlation of histologic changes in the human breast with the menstrual cycle. Am. J. Pathol. 1981; 104: 23-34.

18. Delille JP, Slanetz PJ, Yeh ED, Kopans DB, Garrido L. Physiologic changes in breast magnetic resonance imaging during the menstrual cycle: perfusion imaging, signal enhancement, and influence of the T_1 relaxation time of breast tissue. Breast J. 2005; 11: 236-241.

19. Müller-Schimpfle M, Ohmenhäuser K, Stoll P, Dietz K, Claussen CD. Menstrual cycle and age: influence on parenchymal contrast medium enhancement in MR imaging of the breast. Radiology 1997; 203: 145-149.

20. Kuhl CK, Bieling HB, Gieseke J, Kreft BP, Sommer T, Lutterbey G, Schild HH. Healthy premenopausal breast parenchyma in dynamic contrast-enhanced MR imaging of the breast: normal contrast medium enhancement and cyclical-phase dependency. Radiology 1997; 203: 137-144.

21. Rieber A, Nüssle K, Merkle E, Kreienberg R, Tomczak R, Brambs HJ. MR mammography: influence of menstrual cycle on the dynamic contrast enhancement of fibrocystic disease. Eur. Radiol. 1999; 9: 1107-1112.

22. Payne GS, Dowsett M., Leach MO. Hormone-dependent metabolic changes in the normal breast monitored non-invasively by ^{31}P magnetic resonance (MR) spectroscopy. The Breast 1994; 3: 20-23.

23. Twelves CJ, Lowry M, Porter DA, Dobbs NA, Graves PE, Smith MA, Richards MA. Phosphorus-31 metabolism of human breast - an *in vivo* magnetic resonance spectroscopic study at 1.5 Tesla. Br. J. Radiol. 1994; 67: 36-45.

24. Stehouwer BL, Klomp DWJ, Korteweg MA, Verkooijen HM, Luijten PR, Mali WPThM, Bosch MAAJ van den, Veldhuis WB. 7 T versus 3 T contrast-enhanced breast magnetic resonance imaging of invasive ductulolobular carcinoma: first clinical experience. Magn. Reson. Imaging 2013; 31: 613-617.

25. Naressi A, Couturier C, Devos JM, Janssen M, Mangeat C, Beer R de, Graveron-Demilly D. Java-based graphical user interface for the MRUI quantitation package. MAGMA 2001; 12: 141-152.

26. Vanhamme L, Boogaart A van den, Huffel S van. Improved method for accurate and efficient quantification of MRS data with use of prior knowledge. J. Magn. Reson. 1997; 129: 35-43.

27. Glaholm J, Leach MO, Collins DJ, Mansi J, Sharp JC, Madden A, Smith IE, McCready VR. *In vivo* ^{31}P magnetic resonance spectroscopy for monitoring treatment response in breast cancer. Lancet 1989; 333: 1326-1327.

28. Twelves CJ, Porter DA, Lowry M, Dobbs NA, Graves PE, Smith MA, Rubens RD, Richards MA. Phosphorus-31 metabolism of post-menopausal breast cancer studied *in vivo* by magnetic resonance spectroscopy. Br. J. Cancer 1994; 69: 1151-1156.

29. Brown R, Storey P, Geppert C, McGorty KA, Leite APK, Babb J, Sodickson DK, Wiggins GC, Moy L. Breast MRI at 7 tesla with a bilateral coil and T_1-weighted acquisition with robust fat suppression: image evaluation and comparison with 3 Tesla. Eur. Radiol. 2013; 23: 2969-2978.

30. Italiaander MGM, Nijholt PJ, Kraft O, Raaijmakers A, Stehouwer BL, Luijten PR, Klomp DWJ. High B_1 dutycycle in bilateral breast imaging at 7 T. Proc. ISMRM, Melbourne, Australia, 2012; 18: 1493.

31. Dzendrowskyj TE, Noyszewski EA, Beers J, Bolinger L. Lipid composition changes in normal breast throughout the menstrual cycle. MAGMA 1997; 5: 105-110.

32. Sharma U, Kumar M, Sah RG, Jagannathan NR. Study of normal breast tissue by *in vivo* volume localized proton MR spectroscopy: variation of water-fat ratio in relation to the heterogeneity of the breast and the menstrual cycle. Magn. Reson. Imaging 2009; 27: 785-791.

33. Degani H, Horowitz A, Itzchak Y. Breast tumors: evaluation with ^{31}P MR spectroscopy. Radiology 1986; 161: 53-55.

34. Ng TC, Grundfest S, Vijayakumar S, Baldwin NJ, Majors AW, Karalis I, Meaney TF, Shin KH, Thomas FJ, Tubbs R. Therapeutic response of breast carcinoma monitored by ^{31}P MRS *in situ*. Magn. Reson. Med. 1989;10: 125-134.

35. Filiberto AC, Mumford SL, Pollack AZ, Zhang C, Yeung EH, Schliep KC, Perkins NJ, Wactawski-Wende J, Schisterman EF. Usual dietary isoflavone intake and reproductive function across the menstrual cycle. Fertility and Sterility 2013; 100: 1727-1734.

CHAPTER 5

On the origin of the *in vivo* ^{31}P MRSI phosphodiester signals from the breast

WJM van der Kemp, BL Stehouwer, JH Runge, JP Wijnen, AJ Nederveen, PR Luijten, and DWJ Klomp.
(submitted)

5.1 Introduction

The phosphomonoesters (PMEs) phosphocholine (PC), phosphoethanolamine (PE) and the phosphodiesters (PDEs) glycerophosphocholine (GPC) and glycerophosphoethanolamine (GPE) are involved in cell membrane metabolism. The concentration ratio of these PMEs to PDEs was shown to be a marker in predicting cancer treatment response in *ex vivo* NMR studies (1,2). With ^{31}P MRS one can easily distinguish PC from GPC and PE from GPE, and these metabolites have been used as biomarkers in many *in vivo* studies, as reviewed by Glunde *et al.* (3). However, in contrast to some *ex vivo* methods, where extraction techniques are used to separate aqueous pools of metabolites from lipid pools, *in vivo* methods will also obtain signals from membrane phospholipids (MPL) (4,5). Moreover, as these MPL have chemical shifts similar to GPC — *e.g.* glycerophosphatidylethanolamine (GPtE) has almost identical chemical shift as GPC (6,7) (The molecular structures and chemical shifts are shown in Figure 5.1) — *in vivo* distinction of these compounds is hampered.

At lower field strength (< 2.5 T) *in vivo* ^{31}P spectra of various tissues, *e.g.* breast (8,9), brain (10-15), liver (16-19), and kidney (20,21) show a large signal in the PDE chemical shift range, with its top between 2-3 ppm referenced to phosphocreatine (PCr). The full width at half max of this signal is dependent upon the field strength, and the delay between excitation and acquisition, as for instance caused by phase encoding. It has been suggested (12,16) that this membrane peak disappears almost completely at high field strength, due to enhanced relaxation by chemical shift anisotropy, leaving only the signals of the aqueous soluble metabolites GPC and GPE. Nowadays, with high magnetic field human MRI, the origin of the PDE ^{31}P MRS signals — whether GPC and GPE, and/or GPtC and GPtE — is of renewed interest.

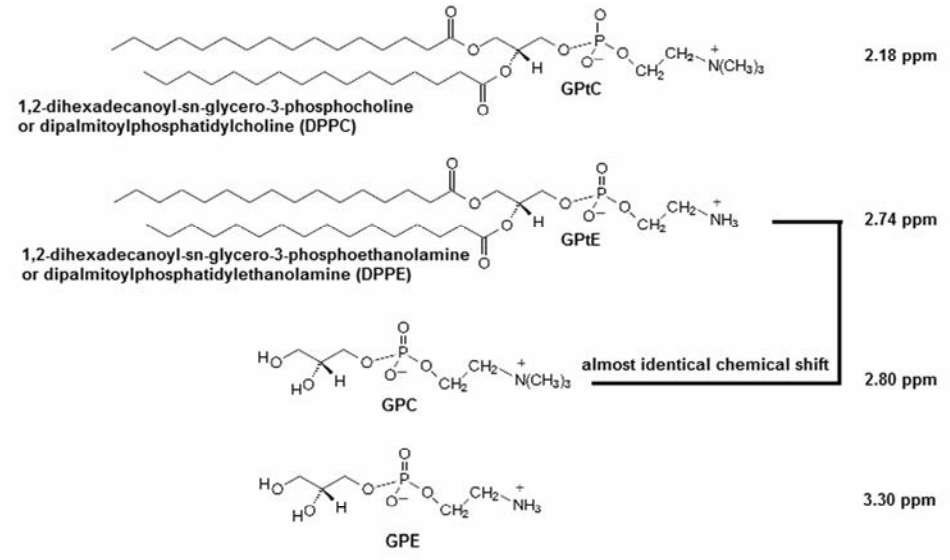

Figure 5.1. Molecular structures of GPC, GPE and their membrane phospholipids GPtC and GPtE. Chemical shift of GPC is taken as a reference at 2.80 ppm. Chemical shift differences $\Delta\delta$(GPtE-GPtC) = 0.56 ppm and (GPC-GPtC) = 0.62 ppm were calculated from high resolution spectra (spectral resolution < 0.02 ppm) by Schiller and Arnold (6), and $\Delta\delta$(GPE-GPC) = 0.50 ppm from Payne *et al.* (7).

Here we show that most of the PDE signals measured *in vivo* in the human breast at 7 T are most likely signals from MPL, although their line widths suggest aqueous small molecules such as GPC and GPE. Measurements are performed at 7 T to distinguish GPE from GPC and GPtE from GPtC. Adiabatic multi-echo spectroscopic imaging (AMESING) (22) and progressive saturation are used to identify the mobility of the molecules as reflected in the T_2 and T_1 values, respectively, to enable a distinction between the aqueous GPE and GPC from the more restricted MPL (GPtE and GPtC). Data are obtained in breast glandular tissue and compared to GPC and GPE metabolite signals as measured in liver tissue, all in healthy human volunteers *in vivo*.

5.2 Methods

^{31}P MRS measurements of glandular breast tissue and liver tissue were obtained from healthy volunteers using a dedicated breast coil (MR Coils BV, Drunen, the Netherlands), or half volume coil for the liver, interfaced to a 7 T MRI system (Philips, Cleveland, USA).

Pulse-acquire and multi-echo acquisitions (AMESING, (22)) were obtained with adiabatic RF pulses. Excitation was done with an adiabatic half passage (AHP) of 2 ms. For refocusing 4 ms B_1 insensitive rotation pulses (BIR-4 180°) were used. The AHP excitation pulse had a frequency sweep of 10.0 kHz and the BIR-4 refocusing pulses a frequency sweep of 20.0 kHz. Both pulses had tangent frequency modulation and hyperbolic tangent amplitude modulation as described in Garwood and Ke (23). Pulses were driven with γB_{1max} = 1700 Hz. Transmitter offset on the ^{31}P channel was set to 600 Hz with respect to the resonance of PCr. All chemical shifts reported here are referenced to PCr as standard at a chemical shift of 0.0 ppm, which is - 2.48 ppm compared to 85% phosphoric acid.

Measurements with the AMESING sequence were performed with a T_R of 6 s, 8x8x8 spherical acquired MRSI, 2x4x4 cm^3 voxel sizes for the breast on three volunteers and 32x10 2D MRSI (feet-head direction unlocalised) voxel sizes 1x1 cm^2 on one volunteer for the liver. Both FID and symmetric echoes were acquired with 256 data points, and the spectral bandwidth for the acquisition of the FID was 17.0 kHz and for the echoes 8.5 kHz (echo spacing 40.5 ms) to maintain equal acquisition durations for FID and each half echo. Acquired data was spatially Hamming filtered and zero filled in the time domain to 8192 data points. To obtain high-SNR spectra of the breast the datasets of three volunteers were pooled and PE-weighted based on the FID signal.

Phosphorus metabolite T_1 values in the breast were measured for the three volunteers by means of progressive saturation with an adiabatic AHP pulse acquire 1D MRSI sequence with T_R values in the range 0.5 to 8 s, where the scan time was kept identical for each T_R. The FID data were acquired with 512 datapoints and a spectral bandwidth of 8.2 kHz. A 1D MRSI encoded in the anterior-posterior direction was chosen to effectively suppress signals from the underlying pectoral muscles. Data was spatially Hamming filtered and subsequently zerofilled in the time domain to 8192 datapoints. To obtain high-SNR datasets for T_1 fitting, the volunteers were measured two or three times and the data per volunteer were averaged. Before averaging all spectra were aligned for Pi. Averaged spectra were spectrally fitted in JMRUI (24) using the AMARES algorithm (25), chemical shifts for the GPtE+GPC and GPtC resonances were fixed with a soft constraint to 2.77 ± 0.1 ppm and 2.18 ± 0.1 ppm and free but equal linewidth. The study was approved by the local medical ethics review board and written informed consent was obtained from all volunteers.

5.3 Results and Discussion

In Figure 5.2 the spectra of a voxel of the breast (average spectrum of three volunteers) and the liver (one volunteer) are shown. Due to limited bandwidth of the adiabatic pulses only the spectral range from +10 to -10 ppm is shown. The chemical shifts of the GPC and GPE signals in the liver (Figure 5.2c) do not correspond to the signals observed in the breast spectra (Figure 5.2a-b), that are usually labelled GPC and GPE, while the chemical shifts of the other metabolites (PE, PC, Pi, γ-ATP, α-ATP) in liver and breast do match. As the chemical shift of GPC and GPE are hardly pH sensitive, but Pi and to a lesser extent also PE, PC, and γ-ATP are (26), *p*H differences between liver and breast may influence chemical shift. If we would shift the breast spectrum by +0.5 ppm, to match the PDE signals between breast and liver, this would correspond to a shift in pH of +0.4 units based on Pi chemical shift. This pH difference is reasonably large, moreover expressing the change in chemical shift of +0.5 ppm for PE, PC and γ-ATP in pH units is either not possible, or goes beyond any physiologic condition. Therefore it seems likely that the metabolite signals in the breast that do not match those in the liver are (GPtE + GPC) and GPtC. Healthy liver is known to show high signals of GPC and GPE in ^{31}P MRS *in vivo* and also in *ex vivo* perchloric acid extracts (27,28). The peak labelled GPtC in the liver spectrum of Figure 5.2c is sometimes referenced to as (potentially) phosphoenolpyruvate (19,29). However, it does not show up in ^{31}P MRS perchloric acid liver extract studies (27,28), even though phosphoenolpyruvate is sufficiently soluble in an aqueous phase. Figure 5.2a,b show, for a voxel of breast glandular tissue, the average FID and the average T_2-weighted echo sum spectra using a fixed T_2 weighting of 154 ± 5 ms (30), scaled to the same noise. Note that the signal intensities of the peaks labelled PE, PC, Pi and (GPtE + GPC) increase, or at least do not decrease, in the echo sum spectrum as compared to the FID spectrum of the breast, while the signals of GPtC and ATP with known short T_2-values, do decrease in the echo-sum spectrum. Unlike ATP, the short apparent T_2 for GPtC (and GPtE) are not the result of homonuclear coupling. The most likely reason for the nearly constant (GPtE + GPC) signal over FID and echo sum is that aqueous GPC, with a relatively long T_2, increases in the echo sum, while GPtC, just like GPtE, decreases in intensity due to short T_2.

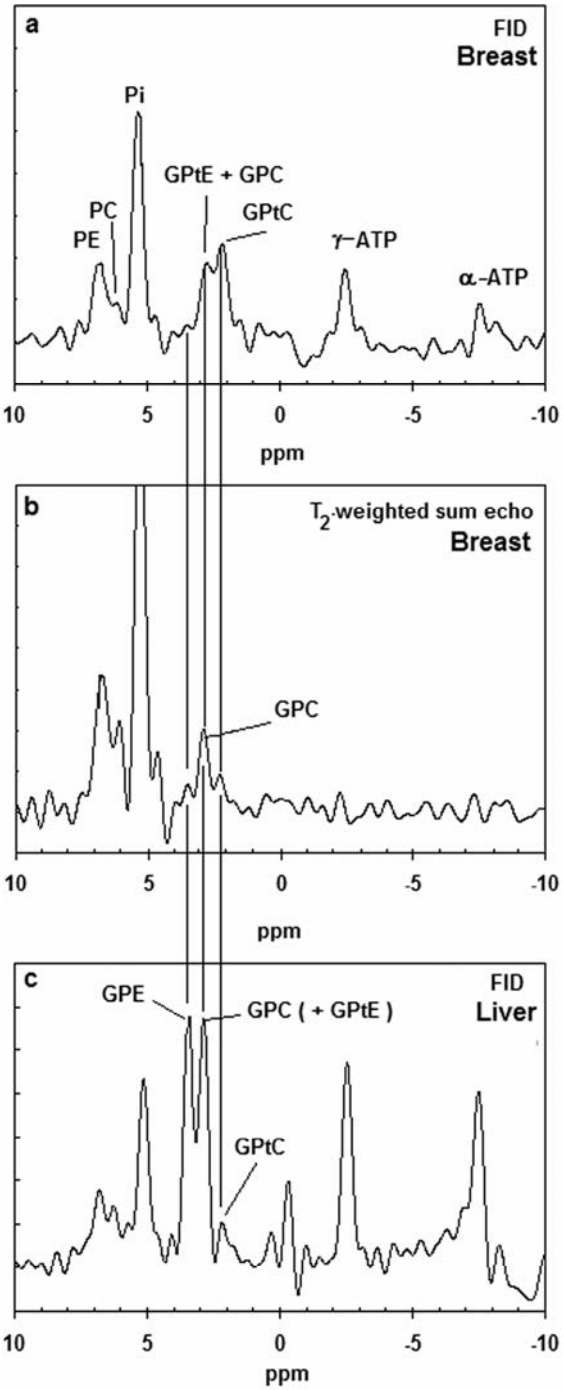

Figure 5.2. (a) Pulse acquire, **(b)** T_2-weighted echo sum (T_2 = 154 ms) ^{31}P MR spectra from a voxel of the breast (average of three volunteers) scaled to the same noise and **(c)** pulse acquire ^{31}P MR spectrum from the liver. Note that only the aqueous metabolites with long T_2 values such as PE, PC, Pi, and GPC get enhanced in the T_2-weighted echo sum and that the chemical shifts of liver GPE and GPC do not match the PDE signals from the breast, but are shifted + 0.5 ppm. The small peak to the right of Pi could potentially be the '2P'-peak from 2, 3-diphosphoglycerate, the '3P'-peak could be coinciding with the left side of Pi in the breast spectra, while it is visible as a small peak to the left of Pi in the liver spectrum.

A recent lipidomic profiling study on healthy mammary epithelial and breast cancer cells (31) has shown that in the membranes of healthy mammary epithelial cells the concentration of GPtC is approximately twice the concentration of GPtE. If we assume that the T_2-weighted echo sum signal at the chemical shift of GPtE+GPC in figure 5.2b is indeed all GPC and we assume a similar T_2 for GPC and PE and PC then we can calculate the GPtC to GPtE ratio by subtraction of the GPC contribution in Figure 5.2a. This leads to a GPtE to GPtC ratio of 2, in close agreement with the lipidomic profiling study. Minor contributions from sphingomyelin and glycerophosphatidylserines, seen in the lipidomic profiling study will probably add to the *in vivo* ^{31}P MR signal of GPtE and glycerophosphatidylinositol to the *in vivo* ^{31}P MR signal of GPtC, not altering the ratio substantially. Chemical shift differences for these different phospholipids are reported by Schiller and Arnold (6).

The ^{31}P T_2 values in liver can be low due to the presence of iron, for instance in the form of ferritin, which is known to increase the relaxivity of water (32). *In vivo* values for T_2 of ^{31}P metabolites (PE, PC, Pi, GPE, GPC) in the liver ranging between 37 ms and 71 ms have recently been measured at 7 T in our hospital in a group of seven healthy volunteers (33). For the breast, however, we measured that the T_2 of the ^{31}P spins at the chemical shift of GPtC (30) is even a factor 3 shorter than the T_2 of the ^{31}P spins of GPC in the liver (33), as shown in Figure 5.3. In fact, compared to the reported T_2 values — measured at 7 T — of PDEs in calf muscle (T_2 = 314 ms (34), 375 ms (22)) or of PC and PE in the breast, the T_2 value of GPtC we measured is almost an order of magnitude less. Spectral fitting of the FID spectrum of Figure 5.2a, simplified by equal linewidths for PE, PC, Pi and equal linewidths for the PDE signals shows an additional linewidth for the PDE signals of 9 Hz, which is close to the calculated value of 12 Hz when considering the measured T_2 of 23 ± 1 ms (30) and a T_2 for the PMEs and Pi of ~ 160 ms.

The low signals for GPE and GPC in the echo sum spectra of the breast are corroborated by an *in vitro* extract study on breast tumours by Smith *et al.* (5), where it was shown that GPE and GPC concentrations are low in non-necrotic breast tumours and that, at low field, PDE signals observed *in vivo* are mainly from phospholipids.

Note though that the signal intensities in the PDE chemical shift region of ^{31}P MR breast cancer spectra could be different from the corresponding signal intensities in healthy breast tissue.

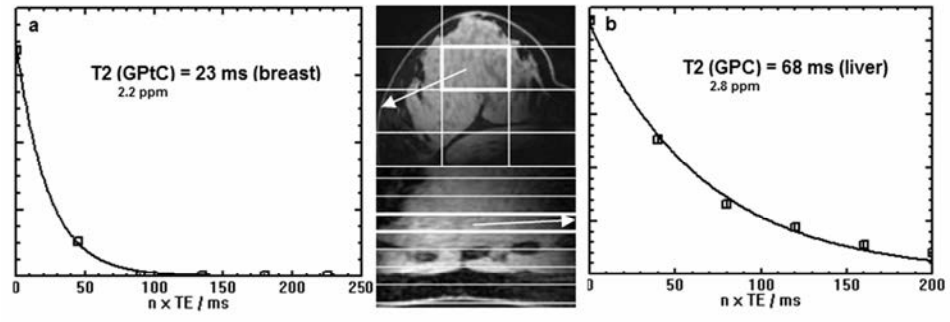

Figure 5.3. Signal decay over echo time of the GPtC peak at 2.2 ppm obtained from (**a**) the breast (30) and (**b**) the true GPC peak from the liver (33) at 2.8 ppm. Note the three-fold reduced T_2 of the ^{31}P spins of GPtC in the breast as compared to GPC in the liver.

Another reason to assume that the dominant phosphodiester signal we observe in the breast at 7 T is from mobile lipid structures is based upon the results of the T_1-measurements of the phosphodiester signal in the breast, as depicted in Figure 5.4.

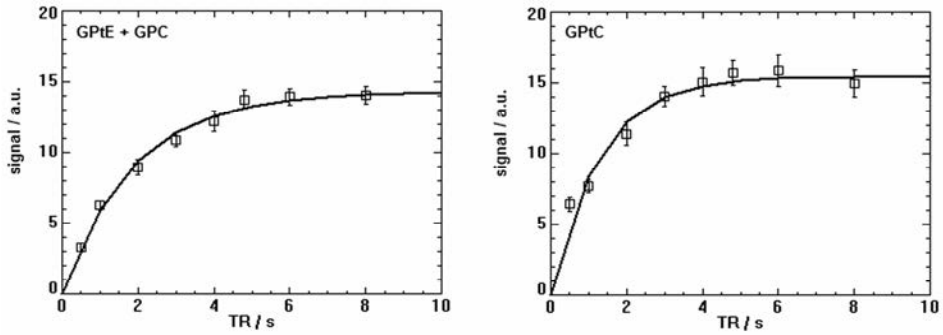

Figure 5.4. T_1-fits of the progressive saturation measurements for the PDE signals in the breast at 7 T. The plots shown are for the sum of three volunteers, but the T_1 values were calculated for the individual volunteers and the weighted average T_1 values (over the three volunteers) are 2.0 ± 0.4 s and 1.2 ± 0.3 s for the GPtE+GPC and GPtC signals respectively.

The T_1-values measured for the two phosphodiester signals are 2.0 ± 0.4 s and 1.2 ± 0.3 s for GPtE+GPC, and GPtC respectively, which is two to four fold less than reported for GPC and GPE in calf muscle and brain at 7 T and 3 T (34-36). Note that the T_1 value for the GPtE+GPC signal is larger than for GPtC, presumably due to the longer T_1 value for GPC, although not statistically significant. A value of 1.4 s for the T_1 of the ^{31}P MRS signal of dipalmitoylphosphatidylcholine (DPPC) vesicles with an average diameter of 100 nm has been measured by Klauda *et al.* (37) above the phase transition temperature. For

multi-lamellar dispersions of dimyristoylphosphatidylcholine (DMPC) a value around 1 s has been measured just above the phase transition temperature by Dufourc *et al.* (38).

The fitted linewidth of the two overlapping PDE signals of the breast spectrum depicted in Figure 5.2a is 58 Hz (i.e. 0.5 ppm). Bulk phospholipid bilayers show broad asymmetrical lineshapes (several tens of ppm) caused by large chemical shift anisotropy (39). Therefore, the very sharp resonances that we observe must be of highly mobile phospholipids, for which chemical shift anisotropy and dipolar couplings are sufficiently averaged out. Especially at ultra-high field, relaxation by chemical shift anisotropy that goes with the square of the field, causes additional line broadening as compared to spectra recorded at lower field strength. Highly mobile phospholipids can be found in small sized vesicles (<50 nm) (40), and in large arrays of: lipidic particles (41), inter-lamellar attachments (ILAs) (42), and inverted cubic structures (42-44) within the lipid bilayer.

The total concentrations of phospholipids in human tissues are in the range of 17 to 83 mmol/kg (45), while the total concentrations of the PMEs in breast glandular tissue are of the order of 2 mM (46). With a signal ratio of PDEs to PMEs in breast glandular tissue of 1.4 at T_R = 6 s (30) and a T_1 of PMEs of 5 s (46) and a T_1 of phospholipids of 1.2 s, the total concentration of *in vivo* visible mobile phospholipids in the human breast at 7 tesla is also of the order of 2 mM. This leads to a crude estimate of the visible mobile phospholipid fraction at 7 tesla of 2 to 12 %.

5.4 Conclusions

The PDE signals from the breast, as measured with MRSI techniques at 7 T *in vivo*, are likely to originate from mobile lipid structures such as small vesicles with diameters ≤ 50 nm, large arrays of lipidic particles or ILAs, or large domains of inverted cubic phases within the lipid bilayer. The T_1 and T_2 relaxation values for these PDE signals are too short to represent true aqueous GPC and GPE. In addition, the chemical shifts of these PDE signals do not correspond to GPE and GPC, but are shifted -0.5 ppm with regard to these, and correspond to chemical shift values of GPtE and GPtC. As the PC over GPC ratio is used as a biomarker in breast cancer research, the *in vivo* obtained value may be contaminated with signal from GPtE —having a similar chemical shift as GPC— or the GPtC peak may be erroneously assigned as GPC.

References

1. Negendank, W. G. Studies of human tumors by MRS: a review. NMR Biomed. 1992; 5: 303–324.
2. F. Podo. Tumour phospholipid metabolism. NMR Biomed. 1999; 12: 413-439.
3. Glunde K, Jiang L, Moestue SA, Gribbestad IS. MRS and MRSI guidance in molecular medicine: targeting and monitoring of choline and glucose metabolism in cancer. NMR Biomed. 2011; 24: 673-690.
4. Cerdan S, Subramanian VH, Hilberman M, Cone J, Egan J, Chance B, Williamson JR. ^{31}P NMR detection of mobile dog brain phospholipids. Magn. Reson. Med. 1986; 3: 432-439.
5. Smith TA, Glaholm J, Leach MO, Machin L, Collins DJ, Payne GS, McCready VR. A comparison of *in vivo* and *in vitro* ^{31}P NMR spectra from human breast tumors: Variations in phospholipid metabolism. Br. J. Cancer. 1991; 63: 514-516.
6. Schiller S, and Arnold K. Application of high resolution ^{31}P NMR spectroscopy to the characterization of the phospholipid composition of tissues and body fluids – a methodological review. Med. Sci. Monit. 2002; 8: 205-222.
7. Payne GS, Troy H, Vaidya SJ, Griffiths JR, Leach MO, Chung Y-L, Evaluation of ^{31}P high-resolution magic angle spinning of intact tissue samples, NMR Biomed. 2006; 19: 593–598.
8. Twelves CJ, Lowry M, Porter DA, Dobbs NA, Graves PE, Smith MA, Richards MA. Phosphorus-31 metabolism of human breast - an *in vivo* MRS study at 1.5 Tesla. Br. J. Radiol. 1993; 67, 36-45.
9. Payne GS, Dowsett M, Leach MO. Hormone-dependent metabolic changes in the normal breast monitored noninvasively by ^{31}P magnetic resonance (MR) spectroscopy. The Breast 1994; 3, 20-23.
10. Sauter A, and Rudin M. Effects of calcium antagonists on high-energy phosphates in ischemic rat brain measured by ^{31}P NMR spectroscopy. Magn. Reson. Med. 1987; 4: 1-8.
11. Kilby PM, Allis JL, Radda GK. Spin-spin relaxation of the phosphodiester resonance in the ^{31}P NMR spectrum of human brain. The determination of the concentrations of phosphodiester components. FEBS Lett. 1990; 272: 163-165.
12. Kilby PM, Bolas NM, Radda GK. ^{31}P-NMR study of brain phospholipid structures *in vivo*. Biochim. Biophys. Acta 1991; 1085: 257-264.
13. McNamara R, Arias-Mendoza F, Brown TR. Investigation of broad resonances in ^{31}P NMR spectra of the human brain *in vivo*. NMR Biomed. 1994; 7: 237–242.
14. Potwarka JJ, Drost DJ, Williamson PC. Quantifying ^{1}H decoupled *in vivo* ^{31}P brain spectra. NMR Biomed. 1999; 12: 8-14.
15. Jensen JE, Drost DJ, Menon RS, Williamson PC. *In vivo* brain ^{31}P-MRS: measuring the phospholipid resonances at 4 Tesla from small voxels. NMR Biomed. 2002; 15: 338-347.

16. Bates TE, Williams SR, Gadian DG. Phosphodiesters in the liver: the effect of field strength on the ^{31}P signal. Magn. Reson. Med. 1989; 12: 145-150.

17. Murphy EJ, Rajagopalan B, Brindle KM, Radda GK. Phospholipid bilayer contribution to ^{31}P NMR spectra *in vivo*. Magn. Reson. Med. 1989; 12: 282-289.

18. Murphy EJ, Bates TE, Williams SR, Watson T, Brindle KM, Rajagopalan B, Radda GK. Endoplasmic reticulum: the major contributor to the PDE peak in hepatic ^{31}P-NMR spectra at low magnetic field strengths. Biochim. Biophys. Acta. 1992; 1111: 51-58.

19. Wylezinska M, Cobbold JF, Fitzpatrick J, McPhail MJ, Crossey MM, Thomas HC, Hajnal JV, Vennart W, Cox IJ, Taylor-Robinson SD. A comparison of single-voxel clinical *in vivo* hepatic ^{31}P MR spectra acquired at 1.5 and 3.0 Tesla in health and diseased states. NMR Biomed. 2010; 24: 231-237.

20. Ratcliffe PJ, Moonen CT, Ledingham JG, Radda GK. Timing of the onset of changes in renal energetics in relation to blood pressure and glomerular filtration in haemorrhagic hypotension in the rat. Nephron. 1989; 51: 225-232.

21. Heindel W, Kugel H, Wenzel F, Stippel D, Schmidt R, Lackner K. Localized ^{31}P MR spectroscopy of the transplanted human kidney *in situ* shows altered metabolism in rejection and acute tubular necrosis. J. Magn. Reson. Imaging 1997; 7: 858-864.

22. Kemp WJM van der, Boer VO, Luijten PR, Stehouwer BL, Veldhuis WB, Klomp DWJ. Adiabatic multi-echo ^{31}P spectroscopic imaging (AMESING) at 7 tesla for measuring transverse relaxation times and regaining sensitivity in tissues with short T_2* values. NMR Biomed. 2013; 26: 1299-1307.

23. Garwood M, and Ke Y. Symmetric pulses to induce arbitrary flip angles with compensation for RF inhomogeneity and resonance offsets. J. Magn. Reson. 1991; 94: 511-525.

24. Naressi A, Couturier C, Devos JM, Janssen M, Mangeat C, Beer R de, Graveron-Demilly D. Java-based graphical user interface for the MRUI quantitation package, MAGMA, 2001; 12: 141–152.

25. Vanhamme L, Boogaart A van den, Huffel S van. Improved method for accurate and efficient quantification of MRS data with use of prior knowledge. J. Magn. Reson. 1997; 129: 35–43.

26. Robitaille P-ML, Robitaille PA, Brown GG Jr., Brown GG, An analysis of the pH-dependent chemical-shift behavior of phosphorus-containing metabolites, J. Magn. Reson. 1991; 92: 73-84.

27. Taylor-Robinson SD, Sargentoni J, Bell JD, Thomas EL, Marcus CD, Changani KK, Saeed N, Hodgson HJ, Davidson BR, Burroughs AK, Rolles K, Foster CS, Cox IJ. *In vivo* and *in vitro* hepatic phosphorus-31 magnetic resonance spectroscopy and electron microscopy in chronic ductopenic rejection of human liver allografts. Gut 1998; 42: 735-743.

28. Taylor-Robinson SD, Thomas EL, Sargentoni J, Marcus CD, Davidson BR, Bell JD. Cirrhosis of the human liver: an *in vitro* ^{31}P nuclear magnetic resonance study. Biochim. Biophys. Acta. 1995; 1272: 113-118.

29. Sevastianova K, Hakkarainen A, Kotronen A, Cornér A, Arkkila P, Arola J, Westerbacka J, Bergholm R, Lundbom J, Lundbom N, Yki-Järvinen H. Nonalcoholic fatty liver disease: detection of elevated nicotinamide adenine dinucleotide phosphate with *in vivo* 3.0-T ^{31}P MR spectroscopy with proton decoupling. Radiology. 2010; 256: 466-473.

30. Stehouwer BL, Kemp WJM van der, Luijten PR, Bosch MAAJ van den, Veldhuis WB, Wijnen JP, Klomp DWJ. ^{31}P magnetic resonance spectroscopy of the breast and the influence of the menstrual cycle. Breast Cancer Res. Treat. 2014; 144: 583-589.

31. Dória ML, Cotrim Z, Macedo B, Simões C, Domingues P, Helguero L, Domingues MR. Lipidomic approach to identify patterns in phospholipid profiles and define class differences in mammary epithelial and breast cancer cells. Breast Cancer Res. Treat. 2012; 133: 635-648.

32. Gossuin Y, Muller RN, Gillis P, Bartel L. Relaxivities of human liver and spleen ferritin. Magn. Reson. Imaging. 2005; 23: 1001-1004.

33. Runge JH, Kemp WJM van der, DWJ Klomp, Nederveen AJ, Stoker J. ^{31}P MRSI of the healthy liver at 3 T and 7 T with AMESING-boosted SNR. ISMRM Milan 2014 abstract number 2265.

34. Bogner W, Chmelik M, Schmid AI, Moser E, Trattnig S, Gruber S. Assessment of ^{31}P relaxation times in the human calf muscle: a comparison between 3 T and 7 T *in vivo*. Magn. Reson. Med. 2009; 62: 574-582.

35. Klomp DWJ, Wijnen JP, Scheenen TW, Heerschap A. Efficient ^{1}H to ^{31}P polarization transfer on a clinical 3 T MR system. Magn. Reson. Med. 2008; 60: 1298-1305.

36. Lei H, Zhu XH, Zhang XL, Ugurbil K, Chen W. *In vivo* ^{31}P magnetic resonance spectroscopy of human brain at 7 T: an initial experience. Magn. Reson. Med. 2003; 49: 199-205.

37. Klauda JB, Roberts MF, Redfield AG, Brooks BR, Pastor RW. Rotation of lipids in membranes: molecular dynamics simulation, ^{31}P spin-lattice relaxation, and rigid-body dynamics. Biophys. J. 2008; 94: 3074-3083.

38. Dufourc EJ, Mayer C, Stohrer J, Althoff G, Kothe G. Dynamics of phosphate head groups in biomembranes. Comprehensive analysis using phosphorus-31 nuclear magnetic resonance lineshape and relaxation time measurements. Biophys. J. 1992; 61: 42-57.

39. Seelig J. ^{31}P nuclear magnetic resonance and the head group structure of phospholipids in membranes. Biochim. Biophys. Acta 1978; 515: 105-140.

40. McLaughlin AC, Cullis PR, Berden JA, Richards R.E. ^{31}P NMR of phospholipid membranes: effects of chemical shift anisotropy at high magnetic field strengths. J. Mag. Reson. 1975; 20: 146-165.

41. Kruijff B de, Verkley AJ, Echteld CJ van, Gerritsen WJ, Mombers C, Noordam PC, Gier J de. The occurrence of lipidic particles in lipid bilayers as seen by ^{31}P NMR and freeze fracture electron-microscopy. Biochim. Biophys. Acta 1979; 555: 200-209.

42. Siegel DP. Inverted micellar intermediates and the transitions between lamellar, cubic, and inverted hexagonal amphiphile phases. III. Isotropic and inverted cubic state formation via

intermediates in transitions between L alpha and HII phases. Chem. Phys. Lipids 1986; 42: 279-301.

43. Jiménez-Monreal AM, Villalaín J, Aranda FJ, Gómez-Fernández JC. The phase behavior of aqueous dispersions of unsaturated mixtures of diacylglycerols and phospholipids. Biochim. Biophys. Acta 1998; 1373: 209-219.

44. Boni LT, Hui SW. Polymorphic phase behaviour of dilinoleoylphosphatidylethanolamine and palmitoyloleoylphosphatidylcholine mixtures. Structural changes between hexagonal, cubic and bilayer phases. Biochim. Biophys. Acta 1983; 731: 177-185.

45. Ansell GB, Spanner S. Phosphatidylserine, phosphatidylethanolamine, and phosphatidylcholine. *In***:** Phospholipids, New Comprehensive Biochemistry, Vol. 4. Hawthorne JN and Ansell CB, (eds). Elsevier Biomedical Press, Amsterdam, 1982, 1-41.

46. Wijnen JP, Kemp WJM van der, Luttje MP, Korteweg MA, Luijten PR, Klomp DWJ. Quantitative ^{31}P magnetic resonance spectroscopy of the human breast at 7 T. Magn. Reson. Med. 2012; 68: 339-48.

CHAPTER 6

Increased sensitivity of ^{31}P MRSI using Direct detection Integrated with Multi-Echo Polarization Transfer (DIMEPT)

WJM van der Kemp, VO Boer, PR Luijten, DWJ Klomp.

(a revised version of this chapter has been accepted for publication in NMR in Biomedicine)

6.1 Introduction

Phosphomonoesters (PME) and phosphodiesters (PDE) have shown clinical potential to be used as biomarkers in oncological and degenerative diseases (1-7). However, direct ^{31}P measurement of these metabolites *in vivo* is hampered by an intrinsic low sensitivity. SNR enhancement for PME and PDE can be obtained by proton decoupling, the Nuclear Overhauser Effect (NOE) or polarization-transfer techniques. *In vivo* proton decoupling is not very useful at high magnetic field because the linewidths are determined mostly by magnetic susceptibility effects and spectral resolution is usually sufficient to distinguish the individual PMEs and PDEs. Moreover, proton decoupling adds to RF power deposition that becomes more problematic at high magnetic field. For NOE, the enhancement for ^{31}P at 7 tesla, measured in the brain, is in the range of only 10 to 44 % (8). As NOE is governed by dipolar relaxation processes and at high-field relaxation by chemical shift anisotropy becomes increasingly important, enhancement by polarization transfer may be a more suitable method at higher field.

Sensitivity enhancement by polarization transfer can for instance be done with an adiabatic Refocused Insensitive Nuclei Enhanced Polarization Transfer RINEPT (9) *i.e.* a BINEPT (10,11) or by a sRINEPT *i.e.* a selectively refocused INEPT (12). In an earlier study we have shown that direct detection of ^{31}P can be combined with polarization transfer in the same scan time, without compromising the polarization transfer signal, since a different pool of spins is observed (13). However, the direct detection signal is hampered by the polarization-transfer sequence because it contains a refocusing pulse on the ^{31}P channel that inverts the z-magnetization of the ^{31}P spins, *i.e.* it transforms the direct

detection part into an inversion recovery sequence. Consequently, the inversion pulse will reduce the performance of the direct ^{31}P signal detection. This effect can be minimized, however, by applying an even number of refocusing pulses on the BINEPT ^{31}P channel: making it a BINEPT multi-echo, hence returning the ^{31}P spins close to equilibrium, as we will show here. Moreover, recently we demonstrated that in direct ^{31}P detection, the Adiabatic Multi-Echo Spectroscopic ImagING -AMESING- (15) sequence can boost SNR as well, particularly in tissues with short T_2* like in the breast. In this work we acquire the majority of all possible signals to enhance SNR per unit of time to the maximum. Coming from both ^{1}H and ^{31}P pools in the detection of phospholipid metabolites, we capture the signal of the BINEPT, as well as adding an even number of refocusing pulses to capture the echoes of spins with relatively long T_2s, with minimal distortion of the ^{31}P pool. In addition, within the same T_R we detect the direct ^{31}P pool including multiple echoes, all at the optimal T_R of 1.26 times the T_1 (14) of the ^{31}P spins. The combined sequence, DIMEPT (Direct detection Integrated with Multi-Echo Polarization Transfer), is depicted in Figure 6.1 and can be used for ^{31}P MRSI.

In the BINEPT multi-echo part of the sequence the ^{31}P spins that are not coupled to protons, *e.g.* Pi, PCr and ATPs, are relatively unaffected by the segmented BIR-4 0° and the BIR-4 180° pulses, and are only excited in the direct detection part of the sequence. The ^{31}P spins that are coupled to protons, *e.g.* PMEs and PDEs, experience a 90° pulse that only excites the polarization that has been transferred from the protons, due to the segmented BIR-4 0° and the 1/4J phase evolution of these coupled spins, provided that the timing τ_1 is correct. Multi-echo 3D MRSI with compensated phase encoding gradients is used in the sequence to enable localized T_2 measurement of ^{31}P metabolites and SNR enhancement by T_2-weighted averaging of all signals per voxel.

Using phantom measurements we demonstrate that multi-echo direct ^{31}P detection can be merged into a BINEPT multi-echo sequence with minimal disturbance of the SNR of polarization transfer or direct detection. In addition, we demonstrate the application of the DIMEPT sequence in the detection of very-low concentrations of PME in the healthy human breast.

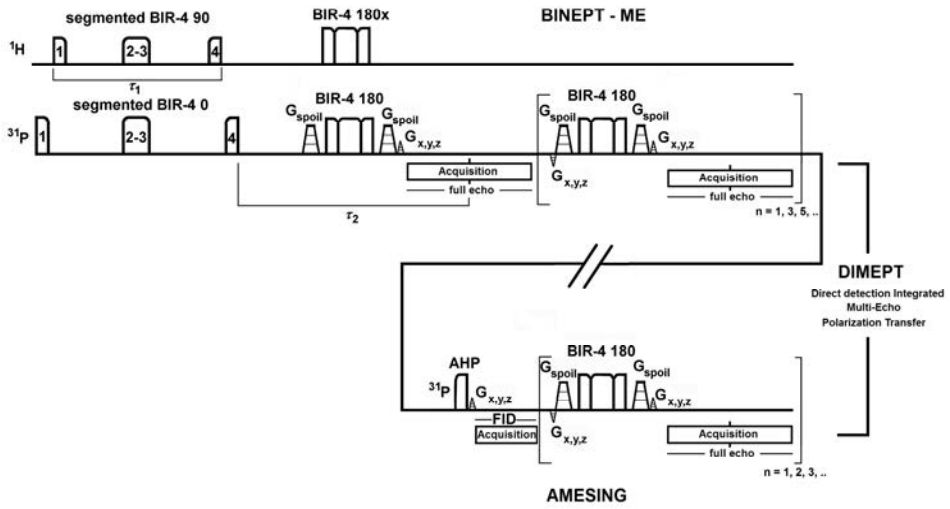

Figure 6.1. Direct detection Integrated with Multi-Echo Polarization Transfer (DIMEPT) for ^{31}P spectroscopic imaging. For the BINEPT multi-echo part the total number of BIR-4 180° pulses should be even, *i.e. n* should be odd.

6.2 Theory

With the DIMEPT sequence, the polarization transfer signal and multiple symmetric echoes of this signal can be acquired combined with a direct detection FID and multiple symmetric echoes in one T_R. All of these signals can be combined to maximize the SNR. A multi-echo approach leads to higher and optimal SNR if $T_2^* << T_2$ and $T_{acq} \geq 1.26T_2^*$, for a FID and $2.52T_2^*$ for a full echo (14). The full echoes contain $\sqrt{2}$ more SNR than half echoes and as maximizing SNR is a main objective, it is advantageous to sample the full echoes and apply T_2-weighted averaging of all the acquired metabolite signals.

The ^{31}P BINEPT signal of a heteronuclear J-coupled metabolite can be higher (here defined as a factor $1/b$) than the direct detection signals. This factor $1/b$ depends on the T_1 of the ^{1}H and ^{31}P spins of the metabolite and the polarization transfer enhancement E_{PT} of the coupled spins that undergo T_2 relaxation during the polarization transfer, which is contained in the factor E_{PT} and which is not given explicitly here.

$$\frac{1}{b} \propto E_{PT} \cdot \frac{1-e^{-T_R/T_1(^1\mathrm{H})}}{1-e^{-T_R/T_1(^{31}\mathrm{P})}} \cdot \frac{(1-\cos\alpha_{\mathrm{E},^{31}\mathrm{P}} e^{-T_R/T_1(^{31}\mathrm{P})})}{\sin\alpha_{\mathrm{E},^{31}\mathrm{P}}} \qquad [6.1]$$

In equation [6.1] the optimal case for $1/b$ is shown with Ernst angle excitation α_E for direct detection. The polarization transfer enhancement E_{PT} is defined as the ratio of the polarization transfer signal, to the pulse acquire FID signal, *i.e.* both with full longitudinal relaxation. The maximum enhancement by polarization transfer for a system with two coupled protons to phosphorus would be $\gamma^1H/\gamma^{31}P = 2.47$. However, as the protons in the phosphoesters show couplings with the protons on the adjacent carbon atom, the actual enhancement will be less. Even neglecting T_2 relaxation, the optimum enhancement E_{PT} (in case of 2 interfering coupled protons) is approximately $0.4\gamma^1H/\gamma^{31}P \approx 1$ (16) which is found for delays of $\tau_2 = 1/4J$ and $\tau_1 = \arctan(\sqrt{2}/2)/\pi J$.

The DIMEPT sequence can be implemented with an even number n of symmetric echoes of the BINEPT-ME part and, for convenience, with an equal number n of symmetric echoes of the AMESING part. These symmetric echoes can be considered equivalent to $2n$ half echoes (*i.e.* equivalent to $2n$ times the FID signal). The expected signal level of the symmetric echoes of AMESING and BINEPT-ME can be written as

$$S_{dd,i} = 2S_{dd,0} \cdot e^{-i\Delta TE/T_2}, \text{ and } S_{PT,i} = \frac{2}{b} S_{dd,0} \cdot e^{-i\Delta TE/T_2}, \qquad [6.2]$$

respectively, where the subscript dd stands for direct detection (AMESING) and PT for polarization transfer (BINEPT-ME), $S_{dd,0}$ is the direct detection FID signal. The subscript i is the echo number for direct detection as well as for polarization transfer. It can be shown (APPENDIX 6.A) that the SNR enhancement, obtained by T_2-weighted averaging of all signals from Eq. [6.2], of a metabolite is given by:

$$E_{wa} = \frac{SNR_{wa}}{SNR_{dd,0}} = \sqrt{1 + 2 \cdot \left(1 + \frac{1}{b^2}\right) \cdot \sum_{i=1}^{n} e^{-2i\Delta TE/T_2}}. \qquad [6.3]$$

Equation [6.3] gives the enhancement in SNR as compared to the FID of the sequence. For $T_R = 1.26T_1(^{31}P)$, the ratio of the signal of a pulse-acquire sequence with 90° pulses to Ernst-angle excitation is a factor 0.96. At $T_R = 1.26T_1(^1H)$, the optimal case for the polarization transfer, it is 0.62 (assuming $T_1(^{31}P) = 5T_1(^1H)$ (12)). The b-values calculated from Eq. [6.1] for the two cases (optimized for direct detection, optimized for polarization transfer) are $b = 0.75$ and $b = 0.49$ respectively.

Figure 6.2 shows a comparison between the SNR enhancement E_{wa} as obtained with equation [6.3], scaled to Ernst-angle excitation for ^{31}P, for the DIMEPT sequence and the AMESING sequence as a function of the $T_2/\Delta TE$ ratio for two optimal conditions; one at the T_R optimal for direct detection with 90 degree excitation (*i.e.* $b = 0.75$) and one with the

T_R optimal for PT, both compared to Ernst angle excitation for direct detection (*i.e.* b = 0.49), assuming $T_1(^{31}P) = 5T_1(^1H)$.

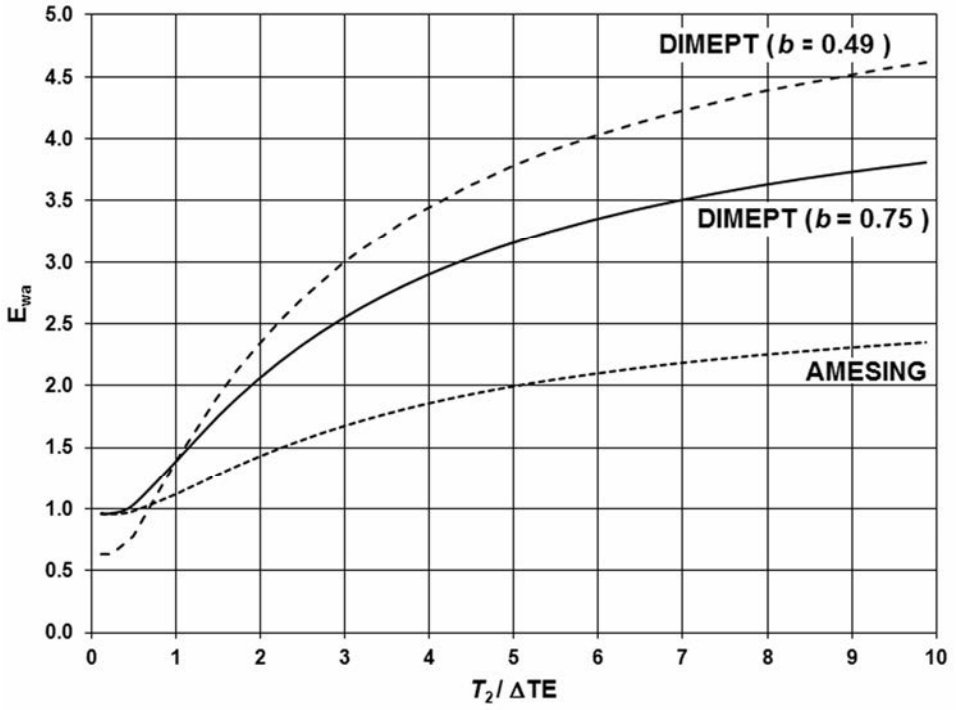

Figure 6.2. Comparison of the theoretical SNR enhancement for the DIMEPT sequence as calculated from equation [6.3], scaled to Ernst angle excitation with E_{wa} = 1, optimized for the direct detection part of the sequence at $T_R = 1.26T_1(^{31}P)$ (b = 0.75) and optimized for the BINEPT part of the sequence with $T_R = 1.26T_1(^1H)$ (b = 0.49), assuming a 5-fold difference in T_1 between ^{1}H and ^{31}P (12), equation [6.1], and the AMESING sequence, as a function of the ratio of the spin-spin relaxation time with the echo spacing $T_2/\Delta TE$. Number of full echoes in AMESING: n = 4; DIMEPT n = 8. With typical T_2 values at 7 T in the breast ranging from 20 to 200 ms (21) and echo spacings of 40 ms expected $T_2/\Delta TE$ values range from 0.5 to 5.

6.3 Experimental

6.3.1 Data acquisition

All measurements were performed with a whole body 7 Tesla MR system (Philips, Cleveland, USA) using a dual-tuned breast coil (MR Coils BV, Drunen, the Netherlands). Both AHP excitation and BIR-4 refocusing pulses were designed with a tangent frequency

modulation with a frequency sweep of 20.0 kHz and hyperbolic tangent amplitude modulation as described in Garwood and Ke (17). The AHP excitation pulse was driven with γB_{1max} = 1700 Hz power and had a duration of 1.0 ms. The BIR-4 180° pulses on the ^{31}P and ^{1}H channels were driven with a power of γB_{1max} = 1700 Hz and had a duration 4.0 ms. Spherical k-space sampling was used to speed up total scan time. Both FID and symmetric echoes were acquired with 256 data points, and the spectral bandwidth for the acquisition of the FID was 17.4 kHz and for the echoes 8.7 kHz to maintain equal acquisition durations for FID and each half echo. The acquisition duration for a FID was 14.7 ms, the first echo time was 38.5 ms and subsequent echo spacings were 40.5 ms. All scans were performed with a T_R = 6 s to remain within SAR limits, resulting in a total scan time of 25:39 minutes. In the BINEPT multi-echo part of the sequence four full echoes were acquired, in the direct detection part of the sequence one FID and four full echoes were acquired.

6.3.2 Data processing

Raw data of FID and echoes were processed using IDL software (Interactive Data Language, Research Systems, Boulder, CO, USA) and JMRUI (18). All data were spatially Hamming filtered and time domain data of FIDs were zero filled to 2048 and the full-echo data to 1024 data points, to account for different dwell times for half- and full-echo acquisition. The FID was first-order phase corrected for the acquisition delay. Time-domain data were Fourier transformed and all spectra, FID and echoes, were frequency aligned with respect to phosphoethanolamine (PE), to minimize the influence of B_0 variations. Zeroth-order phasing of the echo spectra was done by matching the maximum PE signal of the real spectrum to the absolute spectrum. For the FID the zeroth-order phase was set to the phase of the even echoes. The baseline of the FID was corrected by means of fitting a second-order spline

The DIMEPT sequence was tested on a spherical phantom of 10 cm diameter containing aqueous 9.8 mM PE, 8.0 mM phosphocholine (PC), 7.8 mM inorganic phosphate (Pi) and 7.3 mM glycerophosphocholine (GPC). Metabolite T_1 values in this phantom range from 6 to 9 s, while T_2 values are in the range of 400 to 500 ms. For comparison a fully T_1 relaxed ^{31}P MRS spectrum was measured and ^{31}P MR spectra using the AMESING sequence without the BINEPT-ME were acquired. The CSI grid for the phantom measurements was

8x8x8 with 20x20x20 mm^3 voxel sizes. The sequence was subsequently used for measuring ^{31}P MR spectra in the breast of five healthy female volunteers (age range 25 to 29 yr, average age 28 yr) with a CSI grid of 8x8x8 and 40x20x40 mm^3 voxel sizes.

6.3.3 Data analyses of volunteers

The data of all volunteers were pooled and weighted with the PE signal intensity to generate a data set of highest SNR for calculating *b*-values (equation [6.1]) and T_2. The echo weighting was done separately for the polarization-transferred signals and the direct detection signals. The polarization-transferred signals (BINEPT-ME) were multiplied by the PE signal of the first echo, *i.e.* the first refocused signal after polarization transfer, summed and divided by the sum of first echo PE-signal weights. The direct detection signals were multiplied by the FID-signal of PE, summed and divided by the sum of PE-FID weights. This procedure leads to PE-signal-weighted group spectra for the four BINEPT-ME symmetric echo signals and five (1 FID and 4 symmetric echoes) PE-signal weighted group spectra of the direct detection sequence. In this way physiological differences between volunteers are minimized and predominantly the signals with their system noise remain. The nine PE-signal-weighted group spectra were subsequently processed in JMRUI (18) for spectral fitting with AMARES (19) and metabolite T_2 values were fitted using the polarization transferred and direct detection signals, assuming mono-exponential decay of transverse relaxation, and taking into account the scaling factor *b*, equation [6.1], between the polarization-transferred signals and the direct detection signals. In the fitting procedure for a metabolite *m*, the T_2 as well as the *b* value were fitted to equation [6.2].

6.4 Results and Discussion

The measurements on a spherical phantom containing PE, PC, Pi, GPC are shown in Figure 6.3 for the DIMEPT and the AMESING sequences. The multi-echo spectra are, for brevity, not shown here, only the first BINEPT spectrum and the FIDs of the DIMEPT and AMESING sequences are shown. For comparison the FID spectrum in Figure 6.3a is with full longitudinal relaxation.

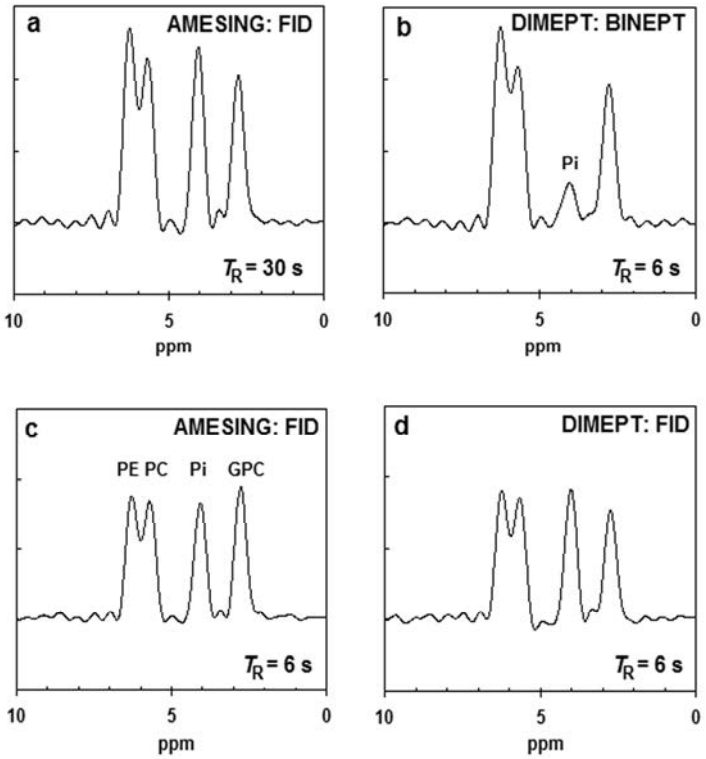

Figure 6.3. ^{31}P Spectra obtained in a 20x20x20 mm^3 voxel of a spherical phantom containing PE, PC, Pi and GPC with the proposed DIMEPT sequence and for comparison with the AMESING sequence. (**a**) FID of the AMESING sequence with full longitudinal relaxation, T_R = 30 s. (**b**) First BINEPT signal of the DIMEPT sequence with T_R = 6 s; (**c**) FID of the AMESING sequence with T_R = 6 s; (**d**) FID of the DIMEPT sequence with T_R = 6 s. Acquired data were apodized with 90 Hz Gaussian line broadening to reduce the truncation artifact for this well shimmed spherical phantom. *In vivo* SNR is much lower and T_2* values for ^{31}P metabolites in the breast are < 10 ms, so these truncation artifacts are expected to remain below noise level.

As the spectra in Figure 6.3 were measured on a well shimmed spherical phantom, the data were apodized with 90 Hz Gaussian line broadening to reduce the truncation artefact. Especially with the high signals of the FID with T_R = 30 s and the polarization transfer signal the truncation artefact is still visible. However, *in vivo* T_2*-values in the breast are short, in the order of 10 ms or less, hence give rise to a small truncation artefact as the duration of the acquisition is 14.7 ms for a FID and 29.4 ms for a full echo, which remains below the noise level.

Note that the BINEPT spectrum of the J-coupled metabolites (Figure 6.3b) corresponds well to the fully T_1-relaxed direct detection spectrum (Figure 6.3a). The small Pi peak is because of T_2 loss during the segmented BIR-4 0° pulse on the ^{31}P channel and excluding phase cycling during all measurements. The FID obtained sequentially after the BINEPT-ME (Figure 6.3d), within the same T_R of 6s, has comparable SNR as the FID obtained exclusively with the AMESING acquisition (Figure 6.3c, *i.e.* without polarization transfer). The polarization transfer efficiency E_{PT} measured for PE, PC, GPC in the phantom were 0.99, 0.88, and 0.87, respectively.

Figure 6.4 shows a comparison of the ^{31}P spectra acquired in summed voxels of fibro-glandular tissue of five healthy female volunteers with the DIMEPT sequence and the AMESING sequence. The spectra shown in Figure 6.4 are the average over five volunteers. Note that the FID spectra of DIMEPT and AMESING are of similar signal intensity. The T_2 and 1/b-weighted spectra reveal the increase in SNR that is obtained when a weighted average of FID and all echoes are taken. As the T_2 and b values are metabolite- and thus chemical shift dependent, the weights were determined as a cubic spline function over the spectral range. The spectra shown in Figure 6.4 are all scaled to the same noise level.

Note the substantial increase in SNR for the PMEs in the DIMEPT T_2,1/b spline-weighted spectrum as compared to the FID of the sequence. When comparing the SNR of the PMEs obtained with the DIMEPT versus the FID of the direct detection, more than 3.5-fold gain is observed. From the weighted spectra of AMESING and DIMEPT it becomes clear that the PDE signals (2.0 to 3.3 ppm) are dominated by metabolites with short T_2 values, presumably from (mobile) phospholipids, *e.g.* glycerophosphatidylcholine and –ethanolamine (20), as their weighted average signal intensity is not enhanced by multi-echo nor polarization transfer. The T_2 and 1/b weighting can be taken into account during quantification of the resonances as can be observed in the DIMEPT weighted average spectrum scaled to the same intensity scale as the FID, (*i.e.* with variable noise through the spectrum) as shown in Figure 6.5.

Figure 6.6 shows a comparison of a quantification with the AMARES algorithm in JMRUI for the FIDs from the AMESING and the DIMEPT sequences. On average the quantified intensities from the FID signals of the DIMEPT sequence, excluding the ATP signals, are 4 % lower than those of the AMESING sequence. The small decrease in the direct detection metabolite signals is most likely caused by the T_2 relaxation during the segmented BIR-4 0° pulse, which is further discussed in Appendix 6.B.

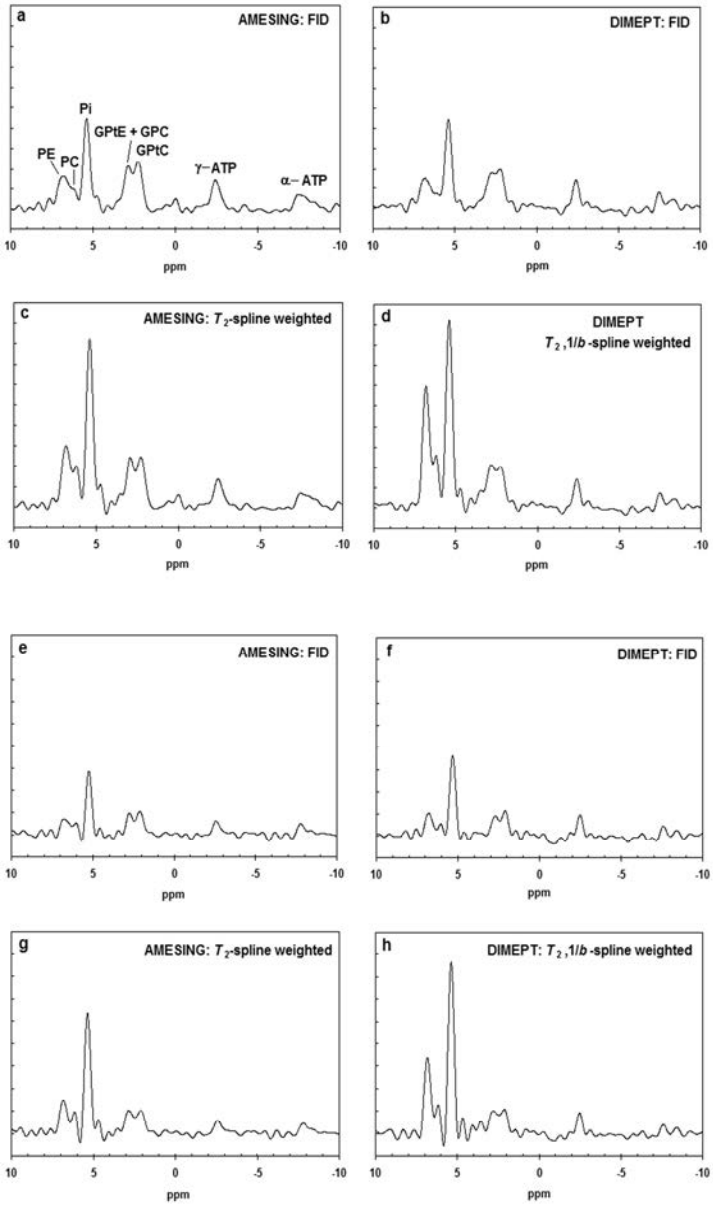

Figure 6.4. *In vivo* ^{31}P MR spectra in a voxel of 40x20x40 mm^3 of the breast, T_R = 6 s. (**a**) – (**d**) Average spectra of five healthy volunteers; (**e**) – (**f**) Spectra of one volunteer. (**a, e**) FID spectrum measured with AMESING (*i.e.* without polarisation transfer); (**b, f**) FID spectrum measured with DIMEPT. (**c, g**) T_2-weighted (using a cubic spline function) AMESING spectrum; (**d, h**) T_2 and 1/b-weighted (using a cubic spline function) DIMEPT spectrum. All spectra are scaled to the same noise level. Note that the cubic spline data need to be used to correct the fitted metabolite levels, which are affected by their individual T_2 and 1/b values.

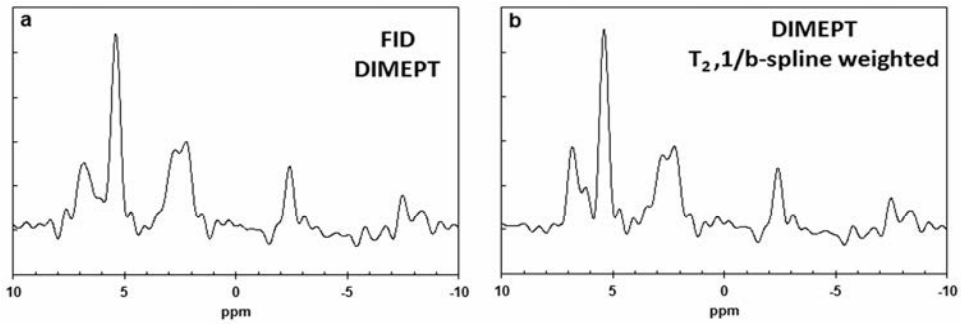

Figure 6.5. FID and weighted average DIMEPT spectrum with T_2 and (1/b) weighting applied throughout the spectrum using a spline function. This way values are scaled at the same intensity as the FID albeit with variable noise throughout the spectrum.

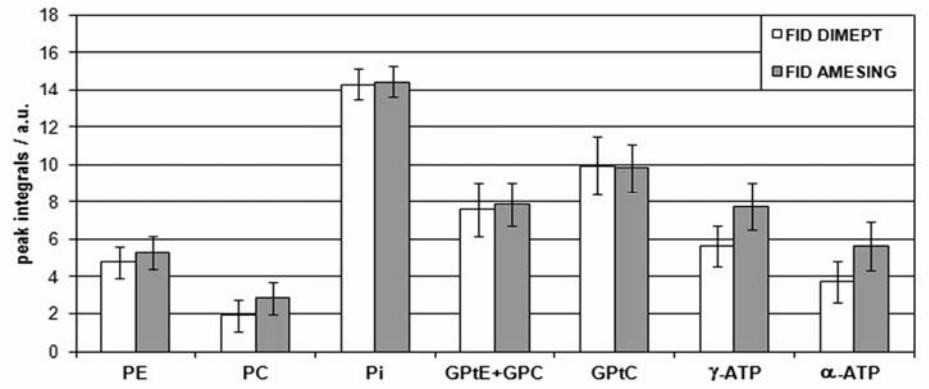

Figure 6.6. Comparison of metabolite quantification of the FIDs of the DIMEPT and the AMESING sequences of the in vivo data shown in Figure 6.4a,b, using the AMARES algorithm within JMRUI.

The SNR enhancements for the phosphomonoesters (PE and PC) based on the weighted average DIMEPT spectrum as compared to the FID of the DIMEPT sequence is more than 3.5. Based on Eq. [6.3], (PE: T_2 = 162 ms, 1/b = 1.67) the SNR enhancement is 3.25. The small discrepancy can be due to limits in SNR, or to incorrect assumptions on T_1. Underestimating metabolite T_1 values leads to overestimation of the SNR enhancement, because the SNR of the FID spectrum depends more on the accurate assumption of T_1 than the BINEPT part of the sequence.

Our present implementation of the DIMEPT sequence contains 11 adiabatic (segmented) BIR-4 pulses of 4 ms and 1 single AHP of 1 ms within a T_R of 6 s driven with a surface RF transmit coil. A shorter T_R or more pulses within the T_R is currently restricted due to SAR limits. If the DIMEPT sequence would be employed using RF coils with

homogeneous B_1 field, then the high SAR demanding adiabatic refocusing pulses may be replaced by short duration block pulses. In that case one could increase SNR per unit of time even further by setting the optimal T_R for the polarization transfer (PT) part of the sequence to a $T_R = 1.26T_1(^1H)$. Or since the T_1 values of the ^{31}P spins of the phosphoesters are a factor of 4 to 5 longer than the T_1 values of the coupled ^1H spins, four PT parts can be interleaved with one direct detection part to maximize SNR for both ^1H as well as the ^{31}P pools. Note however, that the DIMEPT sequence relies on the segmented BIR-4 pulses for obtaining both polarization transfer as well as a 0° pulse to keep the ^{31}P pool unaffected. A hybrid sequence with SAR demanding segmented BIR-4 pulses for polarization transfer and low SAR demanding 180° pulses for refocusing may then be the most optimal solution.

In conclusion, we have shown that the SNR per time unit of the signals of heteronuclear J-coupled ^{31}P metabolites can be increased by using an adiabatic multi-echo polarization transfer technique with an even number of 180° refocusing pulses on the ^{31}P channel combined with an adiabatic multi-echo direct detection sequence in one T_R, while minimally affecting the polarization transfer or the direct detection signal. The *in vivo* increase in SNR for PMEs as compared to an optimal 90° pulse acquire acquisition is more than three fold, or 270% when compared to Ernst-angle excitation pulse acquire. The PDE signals in the breast, presumably mainly mobile phospholipids, have too short T_2 to be enhanced by a multi-echo or polarization-transfer method.

References

1. Negendank W. Studies of human tumors by MRS: a review. NMR Biomed. 1992; 5: 303–324.
2. Podo F. Tumour phospholipid metabolism. NMR Biomed. 1999; 12: 413–439.
3. Glunde K, Bhujwalla ZM, Ronen SM. Choline metabolism in malignant transformation. Nat. Rev. Cancer 2011; 11: 835–848.
4. Harper DG, Jensen JE, Ravichandran C, Sivrioglu Y, Silveri M, Iosifescu DV, Renshaw PF, Forester BP. Tissue-specific differences in brain phosphodiesters in late-life major depression. Am. J. Geriatr. Psychiatry 2014; 22: 499-509.
5. Weber-Fahr W, Englisch S, Esser A, Tunc-Skarka N, Meyer-Lindenberg A, Ende G, Zink M. Altered phospholipid metabolism in schizophrenia: A phosphorus-31 nuclear magnetic resonance spectroscopy study. Psychiatry Res. 2013; 214: 365-73.

6. Valenzuela MJ, Sachdev P. Magnetic resonance spectroscopy in Alzheimer disease. Neurology 2001; 56: 592–598.

7. Yildiz A, Sachs GS, Dorer DJ, Renshaw PF. ^{31}P Nuclear magnetic resonance spectroscopy findings in bipolar illness: a meta-analysis. Psychiatry Res. 2001; 106: 181–191.

8. Lei H, Zhu XH, Zhang XL, Ugurbil K, Chen W. *In vivo* ^{31}P magnetic resonance spectroscopy of human brain at 7 T: an initial experience. Magn. Reson. Med. 2003; 49: 199-205.

9. Burum DP, Ernst RR. Net polarization transfer via a J-ordered state for signal enhancement of low-sensitivity nuclei. J. Magn. Reson. 1980; 39: 163–168.

10. Merkle H, Wei H, Garwood M, Ugŭrbil K. B_1-insensitive heteronuclear adiabatic polarization transfer for signal enhancement. J. Magn. Reson. 1992; 99: 480–494.

11. Payne GS and Leach MO. Surface-coil polarization transfer for monitoring tissue metabolism *in vivo*. Magn. Reson. Med. 2000; 43: 510–516.

12. Klomp DWJ, Wijnen JP, Scheenen TWJ, Heerschap A. Efficient ^{1}H to ^{31}P polarization transfer on a clinical 3 T MR system. Magn. Reson. Med. 2008; 60: 1298–1305.

13. Kemp WJM van der, Boer VO, Luijten PR, Wijnen JP, Klomp DWJ. Increase in SNR for ^{31}P MR spectroscopy by combining polarization transfer with a direct detection sequence. Magn. Reson. Med. 2012; 68: 353–357.

14. Pohmann R, Kienlin M von, Haase A. Theoretical evaluation and comparison of fast chemical shift imaging methods, J. Magn. Reson. 1997; 129: 145–160.

15. Kemp WJM van der, Boer VO, Luijten PR, Stehouwer BL, Veldhuis WB, Klomp DWJ. Adiabatic multi-echo ^{31}P spectroscopic imaging (AMESING) at 7 tesla for measuring transverse relaxation times and regaining sensitivity in tissues with short T_2* values. NMR Biomed. 2013; 26: 1299-1307.

16. Mohebbi A and Goonen O. Recovery of heteronuclear coherence-transfer efficiency losses due to ^{1}H–^{1}H J-coupling in proton to phosphorus RINEPT. J. Magn. Reson. Series A 1996; 123: 237–241.

17. Garwood M and Ke Y. Symmetric pulses to induce arbitrary flip angles with compensation for RF inhomogeneity and resonance offsets. J. Magn. Reson. 1991; 94: 511–525.

18. Naressi A, Couturier C, Devos JM, Janssen M, Mangeat C, Beer R de, Graveron-Demilly D. Java-based graphical user interface for the MRUI quantitation package, MAGMA, 2001; 12: 141–152.

19. Vanhamme L, Boogaart A van den, Huffel S van. Improved method for accurate and efficient quantification of MRS data with use of prior knowledge. J. Magn. Reson. 1997; 129: 35–43.

20. Kemp WJM van der, Stehouwer BL, Runge JH, Wijnen JP, Nederveen AJ, Luijten PR, Klomp DWJ. AMESING and BINEPT ^{31}P MRS at 7 T distinguishes glycerophosphatidylcholine from glycerophosphocholine. Proceedings ISMRM Milan, 2014, 4073.

21. Stehouwer BL, Kemp WJM van der, Luijten PR, Bosch MAAJ van den, Veldhuis WB, Wijnen JP, Klomp DWJ. ^{31}P magnetic resonance spectroscopy of the breast and the influence of the menstrual cycle. Breast Cancer Res. Treat. 2014; 144: 583-589.

APPENDIX 6.A

SNR enhancement of T_2-weighted signal averaging

For a maximum SNR, all signals can be averaged using sensitivity weighting; *i.e.* making use of the 1/*b*-scaling factor between polarization transfer and direct detection signals, and T_2 weighting of all echoes and FID of a metabolite:

$$S_{\mathrm{wa}} = \frac{S_{\mathrm{dd},0} w_{\mathrm{dd},0} + 2\sum_{i=1}^{n}\left(w_{\mathrm{dd},i} \cdot S_{\mathrm{dd},i}\right) + \frac{2}{b}\sum_{i=1}^{n}\left(w_{\mathrm{PT},i} \cdot S_{\mathrm{dd},i}\right)}{w_{\mathrm{dd},0} + 2\sum_{i=1}^{n} w_{\mathrm{dd},i} + 2\sum_{i=1}^{n} w_{\mathrm{PT},i}}. \qquad [6.A1]$$

The weighted average noise can be written

$$\sigma_{\mathrm{wa}}^2 = \sigma_{\mathrm{dd},0}^2 \cdot \frac{w_{\mathrm{dd},0}^2 + 2\sum_{i=1}^{n} w_{\mathrm{dd},i}^2 + 2\sum_{i=1}^{n} w_{\mathrm{PT},i}^2}{\left[w_{\mathrm{dd},0} + 2\sum_{i=1}^{n} w_{\mathrm{dd},i} + 2\sum_{i=1}^{n} w_{\mathrm{PT},i}\right]^2}, \qquad [6.A2]$$

where $\sigma_{\mathrm{dd},0}^2$ is the noise of the FID (or half echo) acquisition.

The T_2-weighting factors for direct detection and polarization transfer echoes are given by

$$w_{\mathrm{dd},i} = e^{-i\Delta TE / T_2}, \text{ and } \; w_{\mathrm{PT},i} = \frac{e^{-i\Delta TE / T_2}}{b}, \qquad [6.A3]$$

respectively. On substitution of equation [6.2] and [6.A3] in equation [6.A1] and $w_{\mathrm{dd},0} = 1$, the T_2-weighted average signal S_{wa} of a metabolite becomes

$$S_{\mathrm{wa}} = S_{\mathrm{dd},0} \frac{1 + 2 \cdot \left(1 + \frac{1}{b^2}\right) \cdot \sum_{i=1}^{n} e^{-2i\Delta TE / T_2}}{1 + 2 \cdot \left(1 + \frac{1}{b}\right) \cdot \sum_{i=1}^{n} e^{-i\Delta TE / T_2}}, \qquad [6.A4]$$

and the weighted average noise can be written

$$\sigma_{wa}^2 = \sigma_{dd,0}^2 \cdot \frac{1+2\cdot\left(1+\frac{1}{b^2}\right)\cdot\sum_{i=1}^{n} e^{-2i\Delta TE/T_2}}{\left[1+2\cdot\left(1+\frac{1}{b}\right)\cdot\sum_{i=1}^{n} e^{-i\Delta TE/T_2}\right]^2}. \qquad [6.A5]$$

Dividing equation [6.A4] by the square root of equation [6.A5] leads to the SNR enhancement E_{wa} of the weighted average signal as given by equation [6.3].

APPENDIX 6.B

Modelling the effect of T_2 loss during the polarization transfer

Neglecting T_2 loss during the RF periods of the pulse itself, due to spin-lock, the effect of the T_2 loss on this segmented pulse can be expressed as a pulse imperfection α. The T_2 loss over a period of 36 ms with a T_2 of 162 ms is 20 %, which can be expressed as an apparent pulse imperfection of the BIR-4 0° of α = 25°. This implies that part of the pool of ^{31}P spins, only have $0.5T_R$ for longitudinal relaxation, before the excitation of the direct detection part of the sequence begins. It can be shown that the influence of this apparent pulse imperfection α on the steady-state longitudinal magnetization available just prior to the 90° pulse for the direct detection FID of the DIMEPT sequence is

$$M_z = M_0\left(\cos(\alpha)\cdot(e^{-T_R/2T_1} - e^{-T_R/T_1}) + 1 - e^{-T_R/2T_1}\right). \qquad [6.B1]$$

In Figure 6.B1, the deviation in the signal intensity of the FID from the DIMEPT is shown as a function of the apparent pulse imperfection angle α. Note that up till pulse imperfections of 30° the decrease of the FID signal intensity does not exceed 5%.

As the timing of the BIR-4 180° pulses is such that $TE << T_R$ and there are an even number of them, the influence of the BIR-4 180° pulses from the BINEPT-ME part of the sequence on the available longitudinal magnetization for the direct detection FID of the DIMEPT is > -1.4 %, for metabolite T_1 values in the range of 1 to 7 s.

To account for the empirical difference in FID signal between the FID of the AMESING sequence and the FID of the DIMEPT sequence of -4 % we assume that -1% is caused by the extra BIR-4 180° pulses of the BINEPT-ME part of the sequence and -3% by the apparent pulse imperfection of the segmented BIR-4 0° in the BINEPT part of the DIMEPT which leads to α = 25° (see Figure 6.B1).

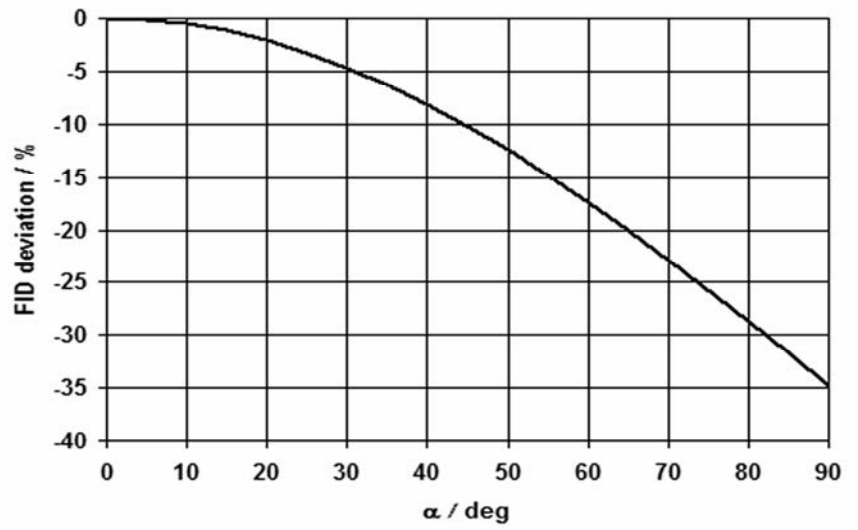

Figure 6.B1. Deviation of the FID signal of the direct detection part of the DIMEPT sequence as a function of the apparent pulse imperfection α (T_2 loss) of the segmented BIR-4 0° pulse of the BINEPT part of the sequence. The figure is shown for the optimal direct detection acquisition of $T_R = 1.26T_1$.

Figure 6.B2 shows for an imperfection angle of 25° the deviation of the FID signal (dashed line) from a 90° pulse acquire signal with T_R = 6 s as a function of metabolite T_1.

Another independent estimate of the apparent pulse imperfection α can be made by comparison of the Pi signal of the first BINEPT echo and the first echo of the AMESING part of the DIMEPT sequence, and extrapolating this to *TE* = 0 ms, by means of the T_2 of Pi, for which we take 188 ms (21). The ratio of the Pi signal, at *TE* = 0, in the BINEPT and the direct detection sequence is 0.29. On neglecting the multi-echoes, the steady-state transverse magnetisation after the BIR-4 0° pulse with apparent imperfection α can be written as

$$M_{xy}(\alpha) = M_0 \cdot (1 - e^{-T_R / 2T_1}) \cdot \sin(\alpha) \qquad [6.B2]$$

The steady-state M_{xy} signal after the 90° pulse in the direct detection part of the DIMEPT equals the steady-state longitudinal magnetisation just before this 90° pulse *i.e.* equal to Eq. [6.B1]. Taking the ratio of Eq. [6.B2] and [6.B1] equal to 0.29 and substituting with T_R = 6 s and T_R/T_1 = 1.26 and solving for α also leads to α = 25°.

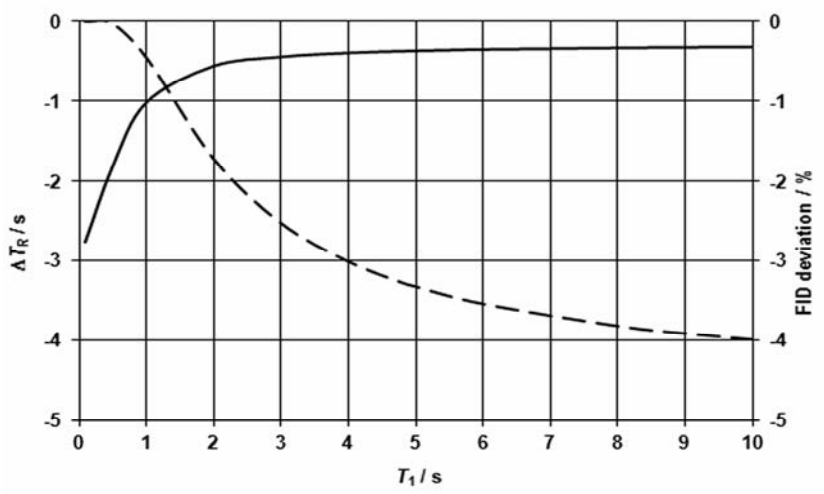

Figure 6.B2. Deviation of the FID signal from the DIMEPT (dashed line) at an apparent pulse imperfection (caused by T_2 loss) of $\alpha = 25°$ of the segmented BIR-4 0°, compared to a conventional 90° pulse acquire FID (both at $T_R = 6$ s), and corresponding deviation in T_R (solid line) as a function of metabolite T_1.

CHAPTER 7

Monitoring of membrane metabolism during neoadjuvant chemotherapy in patients with breast cancer using phosphorus MR spectroscopy at 7 tesla

WJM van der Kemp, BL Stehouwer, PR Luijten, MAAJ van den Bosch, and DWJ. Klomp.

(in preparation)

7.1 Introduction

Breast cancer is by far the most prevalent type of cancer in women worldwide (1). Surgical breast cancer treatment is sometimes preceded by a neoadjuvant therapy such as chemotherapy, endocrine therapy, and/or targeted therapy. Neoadjuvant therapy is applied in patients with inoperable inflammatory or locally advanced breast cancer and nowadays also in patients with operable breast cancer, to reduce tumor volume to enable breast conserving surgery (2). Although reduction of the tumor volume is achieved in the majority of patients, a pathologic complete response is only seen in less than 20% of patients according to a recent meta-analyses which included almost 3800 breast cancer patients receiving neoadjuvant therapy (3). Because of this low pathologic complete response that is often used to predict survival rate, there is a need for early assessment of neoadjuvant chemotherapy efficacy, which would enable switching to a possibly more successful agent early in therapy. In contrast to imaging, that monitors the tumor's morphology alterations during neoadjuvant therapy, the monitoring of tumor metabolism may offer a faster and better window to assess therapy efficacy. Phosphorus magnetic resonance spectroscopy (^{31}P MRS) is probably the most suitable tool to achieve this, because the metabolites of interest are phosphorus compounds such as the phosphomonoesters (PME) phosphocholine (PC) and phosphoethanolamine (PE) and the phosphodiesters (PDE) glycerophosphocholine (GPC) and glycerophosphoethanolamine (GPE) that

are involved in cell membrane anabolism and catabolism respectively (4,5). In addition to these metabolites, signals of mobile phospholipids glycerophosphatidylcholine (GPtC) and glycerophosphatidylethanolamine (GPtE), but also metabolites involved in energy metabolism such as inorganic phosphate (Pi) and adenosinetriphosphate (ATP) can be measured with ^{31}P MRS.

Although hampered by a relatively low intrinsic sensitivity, ^{31}P MRS offers substantial benefits above proton (^{1}H) MRS in monitoring tumor metabolism. *In vivo* measurement of these individual ^{31}P metabolites is feasible with ^{31}P MRS, while *in vivo* proton MRS can only assess a 'total-choline' signal that comprises the sum of PMEs and PDEs. In contrast to ^{1}H MRS, that necessitates water suppression that may bias the total choline signal, phosphorus MRS doesn't require water suppression. Moreover the chemical shift of Pi, as measured in ^{31}P MRS may serve as a proxy for intracellular *p*H and tumor hypoxia.

The first clinical application of ^{31}P MRS in monitoring neoadjuvant chemotherapy in breast cancer patients was reported in 1989 by Ng *et al.* (6), after which a number of reports followed (7-10). All of these studies were performed at low magnetic field, having insufficient spectral resolution to resolve the individual PME (PE, PC) signals or individual PDE (GPE, GPC and mobile GPtE and GPtC) signals. Moreover, the sensitivity at these lower field strengths could only detect MR spectra from very large tumors, often involving almost the entire breast. Nonetheless, these previous studies report increased PME signal prior to therapy and decreasing PME during therapy for responders and partial responders. After the publication of Leach *et al.* in 1998 (10), it took 13 years to improve ^{31}P MRS in breast cancer to facilitate clinical studies in more relevant tumor sizes. First of all, the field strength was increased from 1.5 T to 7 T, and efficient quadrature RF coils were designed dedicated to the human breast (11). All together this improved sensitivity by an order of magnitude; a factor of 2 from 1.5 T to 3 T and more than a factor of 5 from 3 T to 7 T using the dedicated breast coil (12). Moreover, MRS sequences were improved that include spatial localization techniques and means to maximize sensitivity even further by using adiabatic multi-echo spectroscopic imaging (AMESING) (13).

In this work we investigate whether state of the art ^{31}P MRSI is sufficiently sensitive to pick up PME alterations in the primary tumor in patients with breast cancer during the course of neoadjuvant chemotherapy.

7.2 Methods

7.2.1 Patients

From the period February 2012 to August 2013, six patients diagnosed with breast cancer (one T1c, four T2 and one T3 stage cancers) who were scheduled for neoadjuvant chemotherapy, at our institute, were asked to participate in this study. The study protocol was approved by the local medical ethics committee and all patients gave written informed consent. All patients received 6 doses of chemotherapy; either 6x FEC (fluorouracil + epirubicine + cyclophosphamide) or 3x FEC followed by 3x docetaxel. Patients underwent a ^{31}P MRSI scan prior to-, half way- and after chemotherapy. Patients underwent surgery within a week after the last scan and chemotherapy efficacy was assessed by histo-pathology.

7.2.2 MRI and MRSI

Patients were scanned in prone position on a 7 tesla MR scanner (Philips Healthcare, Cleveland, USA) using a unilateral two channel double tuned RF breast coil (MR Coils BV, Drunen, The Netherlands). The scan session contained a fat-suppressed T_1-weighted 3D MRI (TE = 2 ms, T_R = 4 ms, binominal 10 degree flip angle, FOV, resolution 1 mm^3). B_0-shimming over the breast was obtained using the standard Philips pencil beam shimming (14). ^{31}P MRSI was obtained using the AMESING sequence (Figure 7.1), in which 1 FID and 5 full echoes were acquired with ΔTE = 45 ms; T_R = 6 s; FOV 160x160x 160 mm^3; 8x8x8 voxels; (2 cm)^3 nominal resolution; BW = 8200 Hz; sampling matrix size = 256; total scan time 25:36 min.

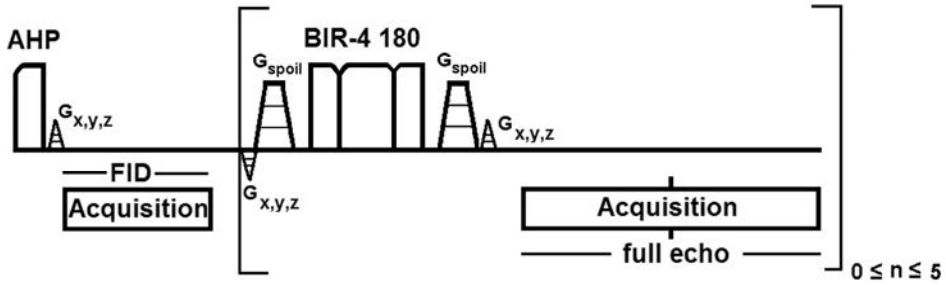

Figure 7.1. Adiabatic multi-echo spectroscopic imaging (AMESING) sequence (13).

7.2.3 Data analysis

Acquired data were zerofilled in the time domain and spatially Hamming filtered. The voxel containing the breast tumor was selected using 3DiCSI (15) for visualisation. Spectra (1 FID and 5 full echoes) from tumor voxels of the patients, prior (P), halfway (HW), and after (A) neoadjuvant chemotherapy were frequency aligned for PE and weighted for the PE intensity of the FID to maximise SNR of the patient group spectra. The weighted sum FID spectra and the five weighted sum spectra of the full echoes at the three points in time were spectrally fitted in JMRUI (16) using the AMARES (17) algorithm. Average chemical shifts of the metabolites were calculated prior to-, halfway-, and after neoadjuvant chemotherapy from FID and echo spectra. Prior to quantification the spectra were apodized with 40 Hz. During spectral fitting overall phases were fixed to zero, the linewidths of PE, PC and Pi were fixed to 55 Hz and the linewidth of GPtE+GPC in the FID was fixed to 65 Hz and in the echoes to 55 Hz (where predominantly GPC is left), the linewidth of GPtC was fixed to 65 Hz. The chemical shift of PE was kept in the range of 6.7 to 6.9 ppm, of GPtE+GPC in the range 2.7 to 2.9 ppm. Frequency differences between PE and PC, GPtE+GPC and GPtC, GPE and GPC were kept at 68 Hz. Metabolic signal ratios for PE/(GPtE+GPC), PC/GPtC and PME/PDE, and PME/Pi were calculated from spectral fitting. Weighted sum spectra of the patient group for the 5 full echoes were spectrally fitted as well and both FID and echo data were used to calculate metabolite T_2 values. 95% Confidence intervals for the metabolite T_2 values were calculated by means of Monte Carlo simulations.

Metabolic signal ratios for the individual patients during the course of neoadjuvant chemotherapy were calculated based on T_2 weighting of the FID and the five symmetric echoes that were acquired for the tumor voxels. Metabolic T_2 weighting was based on an assumed proportionality between accurately known average T_2 values of ^{31}P metabolites in healthy glandular tissue (18) and those values in tumor tissue. To this end the ^{31}P spectrum of a voxel containing the tumor was SNR optimized for all signals by fitting the same proportionality constant for all metabolites while applying the T_2 weighting.

7.3 Results and Discussion

Within a time frame of 17 months, six patients participated in this study. One patient dropped out after the first scan session due to claustrophobia. Cancer type and receptor

status of the breast cancers were assessed from core needle biopsies. Two patients of the group who successfully concluded this study were diagnosed with invasive ductolobular carcinoma, two with invasive ductal carcinoma, and one with medullary carcinoma. Three patients had receptor status ER +, PR +, Her2neu – and two were triple negative. Histopathologic assessment showed that the patient group that concluded the study (n = 5) consisted of one full responder and four partial responders. After chemotherapy the full responder still had a fibroadenoma surrounding the tumor location.

The FID spectra during neoadjuvant chemotherapy for the patient group are shown in Figure 7.2. For comparison, a FID spectrum of a healthy volunteer group consisting of seven healthy volunteers measured four times and with a four times larger nominal voxel size is shown as well (18). There are a number of distinct features that distinguish the presented breast cancer spectra from the healthy volunteer group spectrum.

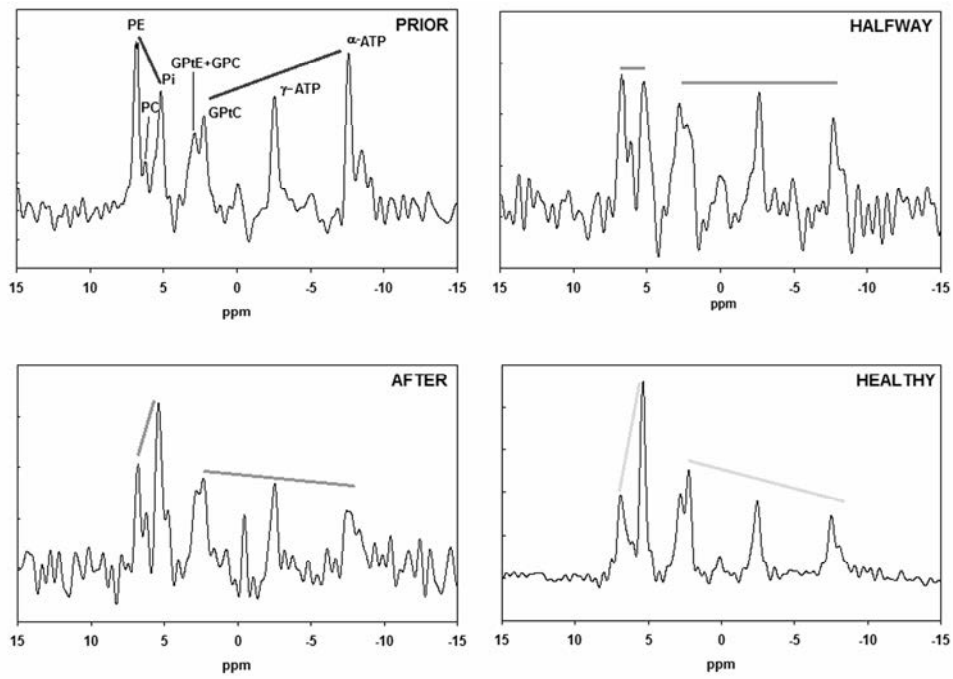

Figure 7.2. Patient group FID spectra during neoadjuvant chemotherapy as compared to a FID spectrum of a group of healthy volunteers. Data from healthy volunteers were obtained recently in our group by Stehouwer *et al.* (18) and are based on 7 volunteers measured four times with four times larger voxel sizes leading to a high-SNR group spectrum.

These distinct features are most prominent when comparing the patient spectrum acquired prior to chemotherapy with the healthy volunteer group spectrum. Prior to chemotherapy the patient group spectrum shows higher: PE than Pi, PE than GPtE+GPC, and PE than GPtC. The signals of γ-ATP and α-ATP are higher than the PDE signals. In the healthy volunteer group spectrum these patterns are reversed. During chemotherapy (half way and after chemotherapy) the patient group spectra are showing more resemblance to the healthy volunteer group spectrum.

In Figure 7.3 the PME to PDE signal ratios (PME/PDE, PE/(GPtE+GPC), PC/GPtC) and the PME to Pi metabolic signal ratios, as obtained from spectral fitting the FID group spectra, are shown during the course of chemotherapy, also in comparison to the healthy volunteer data by Stehouwer *et al.* (18). Except for PC/GPtC, with the largest error bars, all metabolite signal ratios of the patient group PE/(GPtE+GPC), PME/PDE and PME/Pi show the same decreasing pattern during the course of chemotherapy and all normalize to values observed in healthy volunteers. The metabolic signal ratios of the averaged group

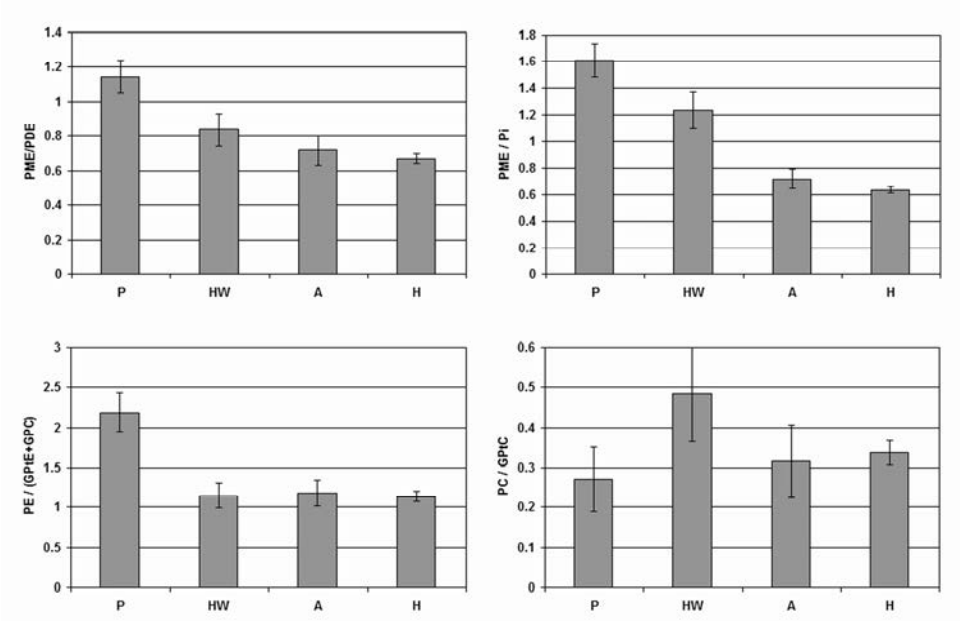

Figure 7.3. PME and PDE metabolic signal ratios obtained by spectral fitting of FID group spectra of patients during neoadjuvant chemotherapy as compared to a group spectrum of 7 healthy volunteers. P: Prior-; HW: Halfway-; A: After neoadjuvant chemotherapy; H: healthy.

spectra shown in Figure 7.3 are based on average group signals (no physiological variability) and system noise (*i.e.* Cramer Rao lower bounds (19)) is represented by the error bars. In Figure 7.4 the PME over PDE ratios are shown as an average based on the individual patient data –including physiological variation as an error bar– and averaged group data with system noise as an error bar. The largest physiological variation between patients is seen in the PME over PDE ratios prior to chemotherapy.

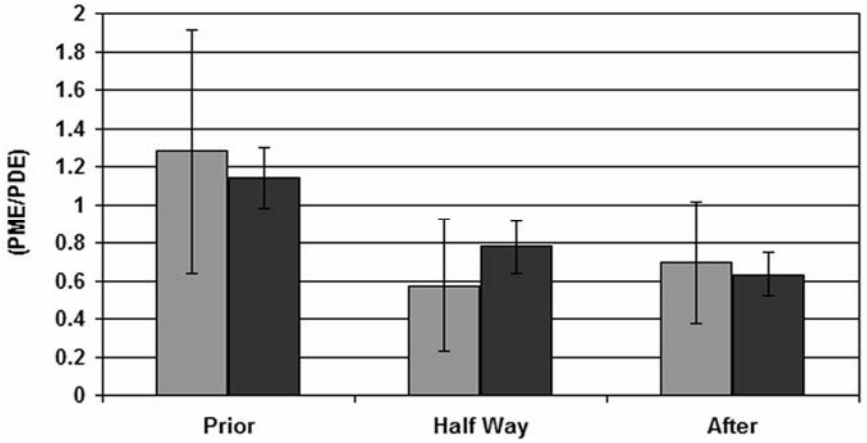

Figure 7.4. Average PME over PDE signal ratios, during the course of neoadjuvant chemotherapy, calculated for individual patients (light grey, with physiological variation) and calculated from averaged patient group spectra (dark grey, without physiological variation).

Patient signal ratios of PME over Pi relative to healthy glandular tissue are shown during the course of chemotherapy, in Figure 7.5. Here, a ratio of 1.0 implies that patients PME over Pi signal ratio equals that of healthy glandular tissue. Prior to neoadjuvant chemotherapy, four out of five patients show significantly higher PME over Pi signal ratios than encountered in healthy glandular tissue. After chemotherapy, one out of five patients shows a significantly lower PME over Pi signal ratio than encountered in healthy glandular tissue, while the other four patients have PME over Pi signal ratios similar to those in healthy glandular tissue. The PME over Pi ratio is a tissue viability marker that can be used in for instance assessing kidney quality for transplantation (20), where a high ratio designates viable tissue. In radiation therapy a decrease of this ratio is an early marker for tumor cell apoptosis (21). However, pre-thermoradiotherapy PME to Pi ratios in sarcomas inversely correlate to pathologic complete response (22).

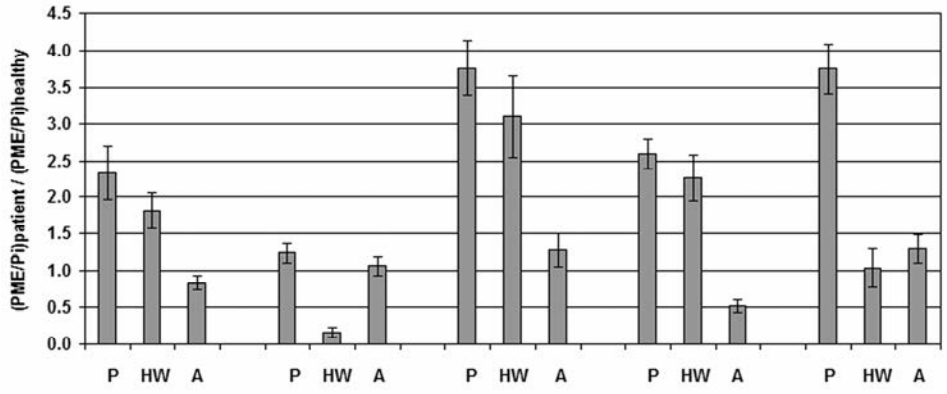

Figure 7.5. Individual patient metabolic signal ratios of PME over Pi, during the course of chemotherapy, relative to healthy glandular tissue. P: Prior-; HW: Half Way-; A: After neoadjuvant chemotherapy. For a value of 1.0 the PME over Pi signal ratio of patient equals that ratio in healthy glandular tissue. Note that all patients showed a higher PME over Pi ratio than 1.0 prior to therapy.

Calculated metabolite T_2 values with 95 % confidence intervals are shown in Figure 7.6 during chemotherapy and for healthy volunteers. Metabolite T_2 values fitted from low-SNR

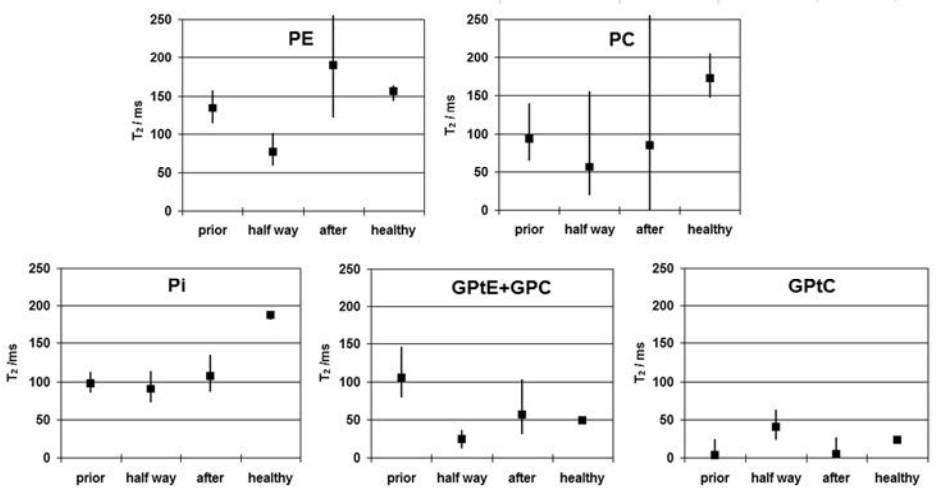

Figure 7.6. Calculated metabolite T_2 values and 95 % confidence intervals for several phosphorus containing metabolites in a breast cancer patient group during neoadjuvant chemotherapy.

data are prone to be overestimated, as is evident from the asymmetric confidence intervals in Figure 7.6. Significantly lower T_2 values are seen for PE(HW), PC(P), Pi(P, HW, A) and GPtE+GPC(HW). Overall there is a trend for lower ^{31}P metabolite T_2 values in these breast

cancer patients, as compared to the metabolite T_2 values in healthy fibroglandular tissue. This matches the lower T_2 values of water in prostate tumors as reported by Roebuck *et al.* (23). The significant higher T_2 for the (GPtE+GPC) signal prior to chemotherapy is possibly caused by increased GPC prior to chemotherapy in this patient group, that includes two triple negative breast cancer patient cases. It is likely that GPtE has a T_2-value similar to GPtC, *i.e.* in the order of 20 ms, while GPC is likely to have a T_2 value that is in the range of the PMEs or even higher. In calf muscle for instance it exceeds 300 ms at 7 T (24). This implies that on average the GPC signal (and concentration) is higher prior to chemotherapy and decreases during therapy in this patient group, which is contrary to the general, probably too simplistic, paradigm of increasing GPC and GPE during successful chemotherapy. This is corroborated by a report on the difference in choline metabolic profile of basal like and luminal like breast cancer xenografts by Moestue *et al.* (25), where it was found that triple negative/basal like breast carcinomas had high GPC/PC ratios.

For the patient group as a whole the average chemical shift of Pi shows an increase of $+0.14 \pm 0.05$ ppm over the course of the chemotherapy, which corresponds to a shift in *p*H of 0.19 units, implying a more acidic environment before the start of the chemotherapy, possibly indicative of tumor hypoxia or lactate formation.

In conclusion, using state of the art ^{31}P MRSI provides sufficient sensitivity to detect statistically significant phospholipid alterations in primary breast tumors during neoadjuvant chemotherapy, despite the limited and heterogeneous sample size. Moreover, the ^{31}P spectrum of the patient group obtained prior to treatment is distinctly different from the ^{31}P spectrum of glandular tissue in the healthy volunteer group and transforms its shape during the course of the chemotherapy towards the shape of the spectrum of the healthy volunteer group. In line with our prospective hypothesis, the elevated PMEs in breast tumors decrease during the course of the chemotherapy. In addition, due to the high spectral resolution at 7 T, a subtle tumor *p*H reduction of 0.19 units is observed during the treatment, possibly indicating tumor hypoxia or lactate formation.

References

1. Jemal A, Bray F, Center MM, Ferlay J, Ward E, Forman D. Global cancer statistics. CA Cancer J. Clin. 2011; 61: 69-90.

2. Liu, S. V., Melstrom, L., Yao, K., Russell, C. A. and Sener, S. F. Neoadjuvant therapy for breast cancer. J. Surg. Oncol. 2010; 101: 283–291.

3. Kong X, Moran MS, Zhang N, Haffty B, Yang Q. Meta-analysis confirms achieving pathological complete response after neoadjuvant chemotherapy predicts favourable prognosis for breast cancer patients. Eur. J. Cancer 2011; 47: 2084-2090.

4. Podo F, Tumor phospholipid metabolism. NMR Biomed. 1999; 12: 413-439.

5. Glunde K, Jie C, Bhujwalla ZM. Molecular causes of the aberrant choline phospholipid metabolism in breast cancer. Cancer Res. 2004; 64: 4270-4276.

6. Ng TC, Grundfest S, Vijayakumar S, Baldwin NJ, Majors AW, Karalis I, Meaney TF, Shin KH, Thomas FJ, Tubbs R. Therapeutic response of breast carcinoma monitored by ^{31}P MRS *in situ*. Magn. Reson. Med. 1989; 10: 125-34.

7. Glaholm J, Leach MO, Collins DJ, Mansi J, Sharp IC, Madden A, Smith IE, McCready VR, *In vivo* ^{31}P magnetic resonance spectroscopy for monitoring treatment response in breast cancer. Lancet 1989; 333: 1326-1327.

8. Redmond OM, Stack JP, O'Connor NG, Carney DN, Dervan PA, Hurson BJ, Ennis JT. ^{31}P MRS as an early prognostic indicator of patient response to chemotherapy. Magn. Reson. Med. 1992; 25: 30-44.

9. Twelves CJ, Porter DA, Lowry M, Dobbs NA, Graves PE, Smith MA, Rubens RD, and Richards MA, Phosphorus-31 metabolism of post-menopausal breast cancer studied *in vivo* by magnetic resonance spectroscopy Br. J. Cancer 1994; 69: 1151-1156.

10. Leach MO, Verrill M, Glaholm J, Smith TA, Collins DJ, Payne GS, Sharp JC, Ronen SM, McCready VR, Powles TJ, Smith IE. Measurements of human breast cancer using magnetic resonance spectroscopy: a review of clinical measurements and a report of localized ^{31}P measurements of response to treatment. NMR Biomed. 1998; 11: 314-340.

11. Klomp DWJ, Bank BL van de, Raaijmakers A, Korteweg MA, Possanzini C, Boer VO, van de Berg CAT, Bosch MAAJ van de, Luijten PR. ^{31}P MRSI and ^{1}H MRS at 7 T: initial results in human breast cancer. NMR Biomed. 2011; 24: 1337–1342.

12. Korteweg MA, Veldhuis WB, Visser F, Luijten PR, Mali WP, Diest PJ van, Bosch MA van den, Klomp DJ. Feasibility of 7 Tesla breast magnetic resonance imaging determination of intrinsic sensitivity and high-resolution magnetic resonance imaging, diffusion-weighted imaging, and ^{1}H-magnetic resonance spectroscopy of breast cancer patients receiving neoadjuvant therapy. Invest. Radiol. 2011; 46: 370-376.

13. Kemp WJM van der, Boer VO, Luijten PR, Stehouwer BL, Veldhuis WB, Klomp DWJ. Adiabatic multi-echo ^{31}P spectroscopic imaging (AMESING) at 7 tesla for measuring transverse relaxation times and regaining sensitivity in tissues with short T_2* values. NMR Biomed. 2013; 26: 1299-1307.

14. Gruetter R. Automatic, localized *in vivo* adjustment of all first- and second-order shim coils. Magn. Reson. Med. 1993; 29: 804-811.

15. Zhao Q, Patriotis P, Arias-Mendoza F, Stoyanova R, Brown TR: 3D Interactive chemical shift imaging: a comprehensive software program for data analysis and quantification. 48th ENC Experimental Nuclear Magnetic Resonance Conference: 2007.

16. Naressi A, Couturier C, Devos JM, Janssen M, Mangeat C, Beer R de, Graveron-Demilly D. Java-based graphical user interface for the MRUI quantitation package, MAGMA, 2001; 12: 141–152.

17. Vanhamme L, Boogaart A van den, Huffel S van. Improved method for accurate and efficient quantification of MRS data with use of prior knowledge. J. Magn. Reson. 1997; 129: 35–43.

18. Stehouwer BL, Kemp WJM van der, Luijten PR, Bosch MAAJ van den, Veldhuis WB, Wijnen JP, Klomp DWJ. ^{31}P Magnetic Resonance Spectroscopy of the breast and the influence of the menstrual cycle. Breast Cancer Res. Treat. 2014; 144: 583-589.

19. Graaf RA de. *In vivo* NMR, Principals and Techniques. Wiley: Chichester; 2007.

20. Bretan PN Jr, Baldwin N, Novick AC, Majors A, Easley K, Ng T, Stowe N, Rehm P, Streem SB, Steinmuller DR. Pretransplant assessment of renal viability by ^{31}P magnetic resonance spectroscopy. Clinical experience in 40 recipient patients. Transplantation. 1989; 48: 48-53.

21. Sakurai H, Mitsuhashi N, Murata O, Kitamoto Y, Saito Y, Hasegawa M, Akimoto T, Takahashi T, Nasu S, Niibe H. Early radiation effects in highly apoptotic murine lymphoma xenografts monitored by ^{31}P magnetic resonance spectroscopy. Int. J. Radiat. Oncol. Biol. Phys. 1998; 41: 1157-1162.

22. Dewhirst MW, Poulson JM, Yu D, Sanders L, Lora-Michiels M, Vujaskovic Z, Jones EL, Samulski TV, Powers BE, Brizel DM, Prosnitz LR, Charles HC. Relation between pO_2, ^{31}P magnetic resonance spectroscopy parameters and treatment outcome in patients with high-grade soft tissue sarcomas treated with thermoradiotherapy. Int. J. Radiat. Oncol. Biol. Phys. 2005; 61: 480-491.

23. Roebuck JR, Haker SJ, Mitsouras D, Rybicki FJ, Tempany CM, Mulkern RV. Carr-Purcell-Meiboom-Gill imaging of prostate cancer: quantitative T_2 values for cancer discrimination. Magn. Reson. Imaging 2009; 27:497-502.

24. Bogner W, Chmelik M, Schmid AI, Moser E, Trattnig S, Gruber S. Assessment of ^{31}P relaxation times in the human calf muscle: a comparison between 3 T and 7 T in vivo. Magn. Reson. Med. 2009; 62: 574-82.

25. Moestue SA, Borgan E, Huuse EM, Lindholm EM, Sitter B, Børresen-Dale AL, Engebraaten O, Maelandsmo GM, Gribbestad IS. Distinct choline metabolic profiles are associated with differences in gene expression for basal-like and luminal-like breast cancer xenograft models. BMC Cancer 2010; 10: 433.

Summary

Chapter 1: Introduction.

At present, the risk of a woman developing invasive breast cancer during her life is about 1 in 8. This makes breast cancer the most prevalent type of cancer in women worldwide. As the risk of dying from breast cancer for a woman is about 1 in 36, early breast cancer detection and effective treatment are paramount in decreasing this risk.

From preclinical studies and clinical studies in large tumors it is known that phospholipid- and energy metabolism are altered in cancer as compared to healthy fibro-glandular tissue. Phosphorus magnetic resonance spectroscopy (^{31}P MRS) offers the possibility to measure a number of key metabolites involved in these processes *in vivo*. Unfortunately, the ^{31}P MRS method is not very sensitive and requires that the magnetic field strength, the coil efficiency, the B_1 field, and the pulse sequences used, are pushed to the limit, all to maximize the signal to noise ratio. The main theme of this thesis is pushing pulse sequences to the limit, to obtain the best signal to noise ratio possible in detecting phosphorus metabolites.

The work described in this thesis can therefore possibly contribute to increasing the specificity of breast cancer detection and monitoring the efficacy of neoadjuvant therapy.

Chapter 2: Increase in SNR for ^{31}P MR spectroscopy by combining polarization transfer with a direct detection sequence.

The sensitivity of ^{31}P MRS can be increased using higher magnetic fields, but in addition also by using ^{1}H to ^{31}P polarization transfer techniques. Consequently, the sensitivity is determined by the polarization of the proton spins and thus the SNR per unit time is unaffected by the slow T_1 relaxation properties of the ^{31}P spins. This implies that ^{31}P spins can be manipulated during the T_1 relaxation of the ^{1}H spins, without affecting the SNR of the ^{1}H to ^{31}P polarization transferred spins. It is shown here that by combining ^{1}H to ^{31}P polarization transfer with a direct ^{31}P detection sequence in one T_R, one can gain more SNR per unit of time as compared to a polarization-transfer sequence alone. Proof of principle is demonstrated by phantom measurements and additionally the method was applied to the human calf muscle and to the human breast *in vivo* at 7 T.

Chapter 3: Adiabatic Multi-Echo ^{31}P Spectroscopic ImagiNG (AMESING) at 7 tesla for measuring transverse relaxation times and regaining sensitivity in tissues with short T_2* values.

An Adiabatic Multi-Echo Spectroscopic ImagING (AMESING) sequence, used for ^{31}P MRSI, with spherical k-space sampling and compensated phase encoding gradients, was implemented on a whole body 7 tesla MR system. One free induction decay (FID) and up to five symmetric echoes can be acquired with this sequence. In tissues with short T_2* and long T_2 this can theoretically lead to a potential maximum SNR increase of almost a factor 3, compared to a conventional FID acquisition with Ernst-angle excitation. However, with T_2 values being in practice $\leq$ 400 ms a maximum enhancement of approximately 2 compared to low flip Ernst-angle excitation should be feasible. The multi-echo sequence also enables the determination of localized T_2-values. The sequence is validated with ^{31}P 3D MRSI on the calf muscle and on the breast of a healthy volunteer, and subsequently applied in a breast cancer patient. The T_2-values of phosphocreatine (PCr), phosphodiesters (PDE) and inorganic phosphate (Pi) in calf muscle were 193 ± 5 ms, 375 ± 44 ms, 96 ± 10 ms, respectively and the apparent T_2 of γ-ATP of 25 ± 6 ms. A T_2 of 136 ± 15 ms for Pi was measured in glandular breast tissue of a healthy volunteer. The T_2-values of phospho-monoesters (PME) and PDE in breast cancer tissue (ductulolobular carcinoma) ranged between 170 and 210 ms and PME to PDE signal ratios were calculated to be for: phospho-ethanolamine (PE) to glycerophosphoethanolamine (GPE) 2.7, phosphocholine (PC) to glycerophosphocholine (GPC) 1.8 and PME/PDE = 2.3. Considering the relatively short T_2* values of the metabolites in breast tissue at 7 T, the echo spacing can be short without compromising spectral resolution, while maximizing sensitivity.

Chapter 4: ^{31}P Magnetic resonance spectroscopy of the breast and the influence of the menstrual cycle.

Phosphorus metabolite ratios are potential biomarkers in breast cancer diagnosis and treatment monitoring. To investigate the metabolite ratios PME to PDE, PE to GPE, and PC to GPC in healthy glandular breast tissue, and the potential effect of the menstrual cycle, we performed ^{31}P MRS at 7 T. Seven women with regular menstrual cycles each underwent four MRS examinations (n = 28 examinations in total) using 3D ^{31}P AMESING. Peak integrals were assessed of spectra from glandular tissue using IDL and JMRUI software. First, T_2 relaxation times were calculated using multi-echo data pooled across

subjects and time points. Subsequent, metabolite ratios were calculated for each phase of the menstrual cycle using the calculated T_2 values to account for when combining the FID and all five echoes. The metabolite ratios were calculated both on group level and individually. T_2 decay fits resulted in a T_2 relaxation time for PE of 154 ms (95% CI 144-164), for PC of 173 ms (95% CI 148-205), for Pi of 188 ms (95% CI 182-193), for GPE of 48 ms (95% CI 44-53), and for GPC of 23 ms (95% CI 21-26). The metabolite ratios analysed on group level showed negligible variation throughout the menstrual cycle. Individual results did show an apparent intra-individual variation, however, non-significant due to the measurements' uncertainty. Based on these findings we conclude that the phospholipid metabolites in glandular breast tissue as measured with ^{31}P MRS at 7 T are not significantly affected by the menstrual cycle.

Chapter 5: On the origin of the *in vivo* ^{31}P MRSI phosphodiester signal of the healthy human breast at 7 tesla.

A large part of the *in vivo* PDE signals from the breast, as measured with ^{31}P MRSI techniques at 7 T, are likely to originate from mobile lipid structures. Examples of these mobile lipid structures are small vesicles with diameters $\leq$ 50 nm, large arrays of inter-lamellar attachments, or large domains of inverted cubic phases within the lipid bilayer. The T_1 and T_2 relaxation times for these PDE signals are too short to represent true aqueous GPC and GPE. In addition, the chemical shifts of these PDE signals do not correspond to GPE and GPC, but are shifted -0.5 ppm with regard to these, and correspond to chemical shift values of glycerophosphatidylethanolamine (GPtE) and glycerophosphatidylcholine (GPtC). As the PC over GPC ratio is proposed as a biomarker in breast cancer research, the *in vivo* obtained value may be contaminated with signal from mobile GPtE, or the GPtC peak may be erroneously assigned as GPC.

Chapter 6: Increased sensitivity of ^{31}P MRSI using Direct detection Integrated with Multi-Echo Polarization Transfer (DIMEPT).

It is shown here that the sensitivity of ^{31}P MRSI of ^{31}P spins J-coupled to protons can be increased by almost a factor 3, as compared to an optimal direct detection FID. By direct detection integrated with multi-echo polarization transfer (DIMEPT), multiple signals from polarization transfer and direct detection can be acquired in one repetition time, with minimal mutual interference, provided that the number of refocusing pulses in the multi-

echo polarization transfer part is even. The DIMEPT sequence is implemented on a 7 tesla body scanner and tested on a phantom and on the breast of five healthy volunteers. The *in vivo* SNR enhancement for the J-coupled PME is 270% as compared to Ernst-angle pulse acquire. However, the PDE signals presumably mainly mobile phospholipids, have too short T_2 values to be enhanced. Uncoupled ^{31}P spins, with sufficiently long T_2 values, such as inorganic phosphate are SNR enhanced by a factor 1.9 as compared to Ernst-angle excitation pulse acquire, due to multi-echo direct detection.

Chapter 7: Non-invasive detection of alterations in membrane metabolism during neoadjuvant chemotherapy in patients with breast cancer using phosphorus MR spectroscopy at 7 tesla.

Here we investigate the feasibility of tumor metabolism monitoring in T1c to T3 breast cancer during neoadjuvant chemotherapy by means of ^{31}P MRSI at 7 T. Five breast cancer patients were examined using a ^{31}P MRSI sequence, prior to-, halfway-, and after neoadjuvant chemotherapy. Histopathologic assessment showed four partial responders and one complete responder to chemotherapy. The ^{31}P MRSI data were analyzed on group level and compared to a spectrum of a group of healthy volunteers. The ^{31}P spectrum of the patient group was distinctly different from the ^{31}P spectrum of healthy volunteers and transformed its shape during the course of chemotherapy towards the shape of the spectrum of the healthy volunteers. Prior to chemotherapy the PME to PDE signal ratio and the PME to Pi signal ratio were high, and during the course of the chemotherapy these ratios normalized to the value of the healthy volunteers. Metabolite T_2 values in tumor tissue tended to be lower than those for healthy glandular tissue. Assessment of individual patients showed that four out of five had a significant drop of the PME to Pi ratio by a factor of 2 or more. On average, the *p*H of the tumor, calculated from chemical shift variation of Pi, was 0.19 units lower before chemotherapy. In conclusion, we have demonstrated that the sensitivity of ^{31}P MRSI in breast cancer at 7 T is sufficient to detect alterations in membrane metabolism during neoadjuvant chemotherapy in T1c to T3 breast cancer, which may be used for early assessment of treatment efficacy.

Samenvatting

Hoofdstuk 1: Inleiding

Momenteel is het risico dat een vrouw borstkanker ontwikkelt gedurende haar leven 1 op 8. Dit maakt borstkanker wereldwijd de meest voorkomende soort van kanker bij vrouwen. Aangezien het risico om te overlijden aan borstkanker voor een vrouw ongeveer 1 op 36 bedraagt, zijn het vroegtijdig detecteren en het effectief behandelen van borstkanker van het grootste belang om dit risico te verlagen.

Uit preklinische studies en klinische studies in grote tumoren is bekend dat het fosfolipide- en energie metabolisme veranderd zijn in kanker ten opzichte van gezond borstklierweefsel. Fosfor magnetische resonantie spectroscopie (^{31}PMRS) biedt de mogelijkheid om een aantal van de sleutelmetabolieten die bij deze processen betrokken zijn *in vivo* te meten. Helaas is de ^{31}P MRS methode niet erg gevoelig en dat maakt dat het magneetveld, de spoel efficiëntie, het B_1-veld en de gebruikte pulssequenties tot de uiterste grens gedreven moeten worden om de best haalbare signaal ruis verhouding te bewerkstelligen voor het detecteren van deze fosformetabolieten.

Het hoofdthema van dit proefschrift is om de grens op te zoeken van wat mogelijk is met pulssequenties, om zo de best haalbare signaal ruis verhouding voor de detectie van fosformetabolieten te verkrijgen.

Het in dit proefschrift beschreven werk kan mogelijk bijdragen tot een verhoging van de specificiteit van borstkanker detectie en het bewaken van de effectiviteit van neo-adjuvante therapie.

Hoofdstuk 2: Verhoging van de SNR in ^{31}P MR spectroscopie door het combineren van polarisatieoverdracht met een directe detectie sequentie.

De gevoeligheid van ^{31}P MRS kan worden verhoogd door toepassing van hogere magneetveldsterktes maar daarbovenop ook door het toepassen van ^{1}H naar ^{31}P polarisatieoverdracht. Hierdoor wordt de gevoeligheid bepaald door de polarisatie van de proton spins en de SNR per tijdseenheid wordt niet beïnvloed door de trage T_1 relaxatie-eigenschappen van de ^{31}P spins. Dit betekent dat de ^{31}P spins gemanipuleerd kunnen worden gedurende de T_1 relaxatie van de ^{1}H spins zonder daarbij de SNR te beïnvloeden

van de ^{31}P spins verkregen via ^{1}H naar ^{31}P polarisatieoverdracht. Hier wordt aangetoond dat door het combineren van ^{1}H naar ^{31}P polarisatieoverdracht met een directe detectie ^{31}P sequentie in een T_R men een hogere SNR kan behalen dan met polarisatieoverdracht alleen. De principiële bruikbaarheid is aangetoond in fantoommetingen, de menselijke kuitspier en de borst op 7 T.

Hoofdstuk 3: Adiabatische multi-echo ^{31}P spectroscopische beeldvorming (AMESING) bij 7 tesla voor het meten van transversale relaxatietijden en het herwinnen van gevoeligheid in weefsels met korte T_2* waarden.

Een adiabatische multi-echo spectroscopische beeldvormings-sequentie (AMESING), gebruikt voor MRSI, met bolvormige k-ruimte bemonstering en gecompenseerde fase-coderingsgradiënten werd geïmplementeerd op een 7 tesla magnetische resonantie systeem geschikt voor het hele lichaam. Eén vrij inductie verval (FID) en tot vijf symmetrische echo's kunnen worden opgenomen met deze sequentie. In weefsels met korte T_2* en lange T_2 kan dit theoretisch leiden tot een potentieel maximale SNR toename van bijna een factor 3, in vergelijk met een conventionele FID opname met Ernst-hoek excitatie. Echter, met T_2 waarden die in de praktijk korter dan 400 ms zijn, zou de maximaal behaalbare toename ongeveer een factor 2 kunnen zijn in vergelijk met lage Ernst-hoek excitatie. Met de multi-echosequentie kunnen bovendien lokaal T_2 waarden bepaald worden. De sequentie is getest met ^{31}P 3D MRSI op de kuitspier en de borst van een gezonde proefpersoon en vervolgens in een patiënte met borstkanker. De T_2-waarden van fosfocreatine (PCr), fosfodiesters (PDE) en anorganisch fosfaat (Pi) in de kuitspier waren respectievelijk 193 ± 5 ms, 375 ± 44 ms, 96 ± 10 ms, en de ogenschijnlijke T_2 van γ-ATP was 25 ± 6 ms. Een waarde van 136 ± 15 ms voor Pi werd gemeten voor de T_2 in het borstklierweefsel van een gezonde proefpersoon. De T_2- waarden voor fosfomonoesters (PME) en PDE in borstkankerweefsel (ductaal lobulair carcinoom) varieerde tussen 170 en 210 ms en de signaalverhoudingen tussen PME en PDE werden bepaald voor: fosfoethanolamine (PE) en glycerofosfoethanolamine (GPE) 2.7, fosfocholine (PC) en glycerofosfocholine (GPC) 1.8 en PME en PDE 2.3. Gezien de relatief korte T_2* tijden van de metabolieten in borstklierweefsel bij 7 T, kan de tijd tussen de echo's kort zijn zonder afbreuk te doen aan de spectrale resolutie terwijl de gevoeligheid gemaximaliseerd wordt.

Hoofdstuk 4: ^{31}P magnetische resonantiespectroscopie van de borst en de invloed van de menstruele cyclus.

Fosformetabolietverhoudingen zijn potentiële biomarkers in de diagnose van borstkanker en de bewaking van de behandeling hiervan. De verhoudingen van PME en PDE, PE GPE, en PC en GPC in gezond borstklierweefsel en de potentiële invloed van de menstruele cyclus hierop, werden onderzocht met ^{31}P MRS bij 7 T. Zeven vrouwen, met een regelmatige menstruele cyclus, werden onderzocht met een 3D ^{31}P MRSI-sequentie en ondergingen elk vier MRS onderzoeken (n = 28 onderzoeken in totaal). Piekintegralen van spectra van borstklierweefsel werden berekend met behulp van IDL en JMRUI software. Eerst werden T_2 relaxatietijden berekend uit samengevoegde multi-echo data over subjecten en tijdspunten. Vervolgens werden de metabolietverhoudingen voor iedere fase van de menstruele cyclus berekend met gebruikmaking van de berekende T_2 waarden voor de weging van FID en alle vijf de echo's. De metabolietverhoudingen werden zowel op groepsniveau als op individueel niveau berekend. Fits van het T_2 verval resulteerden in T_2 relaxatie tijden voor PE van 154 ms (95% betrouwbaarheidsinterval (CI) 144-164), voor PC van 173 ms (95% CI 148-205), voor Pi van 188 ms (95% CI 182-193), voor GPE van 48 ms (95% CI 44-53), en voor GPC van 23 ms (95% CI 21-26). Op groepsniveau vertoonden de metabolietverhoudingen verwaarloosbare variatie over de menstruele cyclus. Individuele resultaten laten een ogenschijnlijke intra-individuele variatie zien die, vanwege de meetonnauwkeurigheid, niet significant is. Gebaseerd op deze bevindingen is de conclusie dat de metabolietverhoudingen van metabolieten betrokken bij het fosfolipidenmetabolisme niet significant beïnvloed worden door de menstruele cyclus.

Hoofdstuk 5: Over de oorspong van het in vivo ^{31}P MRSI fosfodiester signaal in de gezonde menselijke borst bij 7 tesla.

Een groot gedeelte van de PDE signalen uit de borst, zoals gemeten met ^{31}P MRSI technieken bij 7 T, is waarschijnlijk afkomstig van structuren met mobiele fosfolipiden. Voorbeelden van deze structuren met mobiele fosfolipiden zijn kleine dubbellaags blaasjes met diameters $\leq$ 50 nm, lange rijen van inter-lamelaire aanhechtingen, of grote gebieden van geïnverteerde kubische fasen binnen de lipidedubbellaag. De T_1 en T_2 relaxatietijden van deze PDE signalen zijn te kort om afkomstig te zijn van werkelijk waterig opgeloste GPC en GPE. Daar komt bij dat de chemische verschuiving van deze PDE signalen niet overeenkomen met GPE en GPC maar -0.5 ppm verschoven zijn ten opzichte van deze en

corresponderen met de chemische verschuiving van glycerofosfatidylethanolamine (GPtE) en glycerophosphatidylcholine (GPtC). Omdat de verhouding van PC met GPC mogelijk gebruikt wordt als biomarker in borstkanker onderzoek, kan de *in vivo* verkregen waarde beïnvloed zijn door signaal van mobiel GPtE, of de piek van GPtC kan abusievelijk worden aangemerkt als GPC.

Hoofdstuk 6: Verhoogde gevoeligheid voor ^{31}P MRSI door gebruikmaking van directe detectie geïntegreerd met multi-echo polarisatieoverdracht (DIMEPT).

Hier wordt aangetoond dat de gevoeligheid van ^{31}P MRSI van ^{31}P spins die een J-koppeling hebben met protonen, kunnen worden verhoogd met bijna een factor 3 ten opzichte van een optimale directe detectie FID. Door directe detectie geïntegreerd met multi-echo polarisatieoverdracht, kunnen meerdere signalen van polarisatieoverdracht en directe detectie worden opgenomen binnen één repetitietijd, met minimale onderlinge interferentie, vooropgesteld dat er een even aantal refocuseringspulsen bij de multi-echo polarisatieoverdracht wordt gebruikt. De DIMEPT sequentie is geïmplementeerd op een 7 tesla MR systeem voor het hele lichaam en getest in een fantoom en op de borst van 5 gezonde proefpersonen. De *in vivo* SNR versterking voor de J-gekoppelde PME was 270% in vergelijking tot een Ernst-hoek excitatiepuls-opname. Echter, de PDE signalen, vermoedelijk hoofdzakelijk afkomstig van mobiele fosfolipiden, hadden te korte T_2 tijden om versterkt te worden. Ongekoppelde ^{31}P spins met voldoende lange T_2 tijden, zoals Pi kregen een versterking tot een factor 1.9 in vergelijking tot een Ernst-hoek excitatiepuls-opname, ten gevolge van de multi-echo directe detectie.

Hoofdstuk 7: Non-invasieve detectie van veranderingen in membraan metabolisme gedurende neo-adjuvante chemotherapie bij patiënten met borstkanker door gebruikmaking van fosfor MR spectroscopie bij 7 tesla.

Hier wordt de mogelijkheid onderzocht van het bewaken van het tumor metabolisme gedurende neo-adjuvante chemotherapie bij T1c tot T3 borstkanker met behulp van fosfor magnetische resonantie spectroscopie bij 7 T. Vijf borstkankerpatienten zijn onderzocht met behulp van een ^{31}P MRSI sequentie voorafgaand-, halverwege- en na neo-adjuvante chemotherapie. Histopathologische beoordeling toonde aan dat er vier partiële respondenten en één volledige respondent op de chemotherapie was. De ^{31}P data werden geanalyseerd op groepsniveau en vergeleken met een spectrum van een groep gezonde

proefpersonen. Het ^{31}P spectrum van de patiëntgroep is duidelijk onderscheidbaar anders dan dat van de gezonde proefpersonen en het veranderde gedurende de chemotherapie van vorm steeds meer gelijkend op het spectrum van de gezonde proefpersonen. Voorafgaand aan de chemotherapie waren de signaalverhoudingen van PME met PDE en Pi hoog, en gedurende het verloop van de chemotherapie normaliseerde deze verhoudingen tot die van de gezonde proefpersonen. Metaboliet T_2 tijden in tumor weefsel vertoonden een trend naar lagere waarden dan die in gezond borstklierweefsel. Beoordeling van de individuele patiënten liet zien dat vier van de vijf patiënten een significante daling hadden van de PME/Pi verhouding van een factor 2 of meer. Gemiddeld genomen was de *p*H van de tumor, berekend uit de verandering van de chemische verschuiving van Pi, 0.19 eenheden lager voor de chemotherapie. Concluderend: er is aangetoond dat de gevoeligheid van ^{31}P MRSI in borstkanker bij 7 T voldoende is om veranderingen in membraanmetabolisme waar te nemen gedurende neo-adjuvante chemotherapie van T1c tot T3 borstkanker, en dat de techniek mogelijk gebruikt kan worden bij de beoordeling van de effectiviteit van de therapie.

Dankwoord

Bij het tot stand komen van dit proefschrift wil ik graag een aantal mensen bedanken die aan het werk hebben bijgedragen of anderszins een belangrijke bijdrage hebben geleverd.

Beste Peter, jouw 7 Tesla Groep haalt de hoogste score voor medewerkerstevredenheid binnen het UMC Utrecht. Naast je vakinhoudelijke kennis van MRI, MRS, en medische beeldvorming, versta je de kunst van het faciliteren, motiveren en ook het vrijlaten van mensen om het beste uit zichzelf en anderen te halen. Dankjewel voor het scheppen van de ideale omstandigheden voor het doen van onderzoek en je hulp bij het beschrijven ervan.

Beste Dennis, jouw enthousiasme, optimisme en vindingrijkheid zijn van cruciaal belang geweest bij het in dit proefschrift beschreven onderzoek. Waar ik menigmaal problemen of zelfs onmogelijkheden zag, waren die vaak na een mailtje, een korte ‘pep-talk’, of nieuwe vondst van je zo weer opgelost. Dankjewel voor al je hulp, je snelle correctiewerk en het in mij gestelde vertrouwen!

Beste Vincent, iedere afdeling heeft iemand nodig zoals jij. Briljant, bescheiden en hulpvaardig. Dankjewel voor je hulp bij het puls-programmeren, het debuggen van mijn patches, het wegwijs maken op de scanner en je correctiewerk.

Beste Bertine, zonder jouw hulp bij het includeren van patiënten was de patiëntenstudie nooit van de grond gekomen. Verder hebben we samen de ‘MRSycle’-studie gedaan en denk ik met veel plezier terug aan onze gezamenlijke scan sessies met vrijwilligers en patiënten. Laten we kijken of we de ‘Repro’-studie ook nog kunnen afronden.

Beste Jannie, dankjewel voor je hulp bij het ^{31}P MRS werk en het corrigeren van een aantal papers. Leuk dat ik als postdoc op jouw project nog een aantal jaar verder kan met de toepassing van ^{31}P MRS bij borstkanker.

Beste Sylvia, dankjewel voor het organiseren van vrijwilligers en het bewaken van de tijdslijnen en administratie. Goed dat je zo af en toe orde op zaken stelt.

Beste Bart, Ingmar, Mark en Michel, (oud)-collega's van het 'MR Coils' lab, hartelijk dank voor jullie technische ondersteuning.

Beste collega's en studenten van de 7 T, jullie gezelschap maakt het werken in het UMC zo plezierig.

De beoordelingscommissie bestaande uit de professoren Van den Bosch, Heerschap, Lagendijk (voorzitter), Moonen, en Nicolay wil ik graag bedanken voor het beoordelen en goedkeuren van dit proefschrift.

Mijn dank gaat ook uit naar alle patiënten en vrijwilligers die aan het onderzoek hebben meegewerkt.

Beste Matthias, lieve zoon, we hebben de afgelopen jaren in de weekends heel wat uren samen in de controlekamer van de 7 T MR scanner doorgebracht. Jij achter een computer met de nieuwste internetspelletjes en ik achter een werkstation gekoppeld aan heel kostbaar magnetisch 'speelgoed'. Samen frietjes eten tijdens de lunch maakte het feest altijd weer compleet.

Lieve Marjo, mede dankzij jou ben ik aan dit avontuur van een nieuwe studie en een tweede promotieonderzoek begonnen. Je uitspraak: "Volgens mij ben je niet burn-out maar bore-out" en je aanmoediging om daar iets aan te gaan doen, hebben het in gang gezet. Dankjewel voor je steun en het creëren van een fijne thuisbasis.

Curriculum Vitae

Wybe van der Kemp werd geboren op 28 november 1964 te Ede. Na het behalen van het MAVO, HAVO en VWO examen in respectievelijk 1981, 1983, en 1984 begon hij aan de studie scheikunde aan de Universiteit Utrecht, die werd afgerond op 28 november 1988. In 1989 startte hij met een promotieonderzoek betreffende de thermodynamica van binaire mengkristallen bij de Faculteit Scheikunde van de Universiteit Utrecht. Dit onderzoek werd afgerond met een academische promotie op 12 september 1994. Vervolgens deed hij een jaar onderzoek op het gebied van de fysische chemie van lipiden aan de Faculteit Scheikunde van de Universiteit Utrecht. Daarop volgden drie jaar (1996-1999) onderzoek naar grondwater hydrogeologie en hydrochemie van de Ledo-Paneseliaan aquifer in Vlaanderen, uitgevoerd aan de Vrije Universiteit van Amsterdam en de Rijksuniversiteit Gent. Vervolgens was hij in de periode 1999-2001 werkzaam als onderzoeker op het gebied van ^{14}C datering van Antarctische ijskernen aan de Faculteit Natuurkunde van de Universiteit Utrecht. Van 2001 tot 2010 was hij werkzaam in de informatie en communicatietechnologie bij ABN-AMRO, de laatste vijf jaar in dienst van IBM. In 2006 begon hij in deeltijd de studie Biomedical Image Sciences (BIS) aan de Universiteit Utrecht die in 2011 werd afgerond. In 2010, tijdens de BIS opleiding trad hij in dienst van het UMC Utrecht en was werkzaam bij de 7 Tesla Groep waar het huidige promotieonderzoek werd uitgevoerd.